

Many-Body Effects in Novel Nanostructures : Optical and Transport Properties

Mousa Bahrami

A Thesis
In
The Department of
Physics

Presented in Partial Fulfillment of the Requirements
For the Degree of
Doctor of Philosophy (Physics) at
Concordia University
Montréal, Québec, Canada

May 2018

©Mousa Bahrami, 2018

CONCORDIA UNIVERSITY
SCHOOL OF GRADUATE STUDIES

This is to certify that the thesis prepared

By: Mousa Bahrami

Entitled: Many-Body Effects in Novel Nanostructures : Optical
and Transport Properties

and submitted in partial fulfillment of the requirements for the degree of

DOCTOR OF PHILOSOPHY (Physics)

complies with the regulations of this University and meets the accepted standards
with respect to originality and quality.

Signed by the final examining committee:

_____ Chair

Dr. Galia Dafni

_____ External Examiner

Dr. Xue-Feng Wang

_____ External to Program

Dr. Dmitry Korotkin

_____ Examiner

Dr. Mariana Frank

_____ Examiner

Dr. Pablo Bianucci

_____ Supervisor

Dr. Panagiotis Vasilopoulos

Approved _____

Dr. Pablo Bianucci, Graduate Program Director

June 21, 2018 _____

Dr. Andre Roy, Dean, Faculty of Arts and Science

ABSTRACT

Many-Body Effects in Novel Nanostructures : Optical and Transport Properties

Mousa Bahrami, Ph.D.

Concordia University, 2018

This work explores many-body effects in novel nanostructures specifically on transport and optical properties. As an introduction, we investigate these properties by employing the Drude model in the classical regime. In quantum regime, these properties are related to the density-density response function known as polarization function. To evaluate the polarization function of a system, we employ Linear Response Theory in the absence of many-body effects. Two such effects are the Coulomb potential and local field factor; we present the random-phase and Hubbard approximations considering the former and latter respectively. Impurity effects have profound influence on a system properties. We develop the Linear Response Theory in the Van Hove limit to consider the impurity effects. As examples of quantum wells and wires, we treat graphene and armchair graphene nanoribbons (AGNRs). The single-body wave function of a system is required to evaluate its polarization function. We introduce the tight-binding approach to evaluate the eigenvalues and eigenfunctions analytically. Within the $k \cdot p$ method we obtain the energy spectrum and eigenvalues of those systems at Dirac points in the low energy limit. We present the dynamical conductivity of AGNRs by considering many-body effects. In addition, we show reflection and transmission coefficients in the absence and presence of electron-electron interaction and scattering for AGNRs. As an example of collective coherent phenomena, we obtain surface plasmons in AGNRs. To investigate the impurity effects on collective coherent phenomena, we evaluate plasmons and surface plasmons in graphene and two-dimensional free electron gas. We show how impurity modifies the dispersion domain of these coherent phenomena. We have also show that there is a critical value for the impurity strength below which there are no collective coherent phenomena. In addition, we obtain an analytic expression for quality factor of surface plasmons for intra-level and inter-level. Finally, we show the effects of two-body collisions on dc transport in a homogeneous system by employing a quantum Boltzmann equation (QBE). As an application of the QBE, we study the effect of screening, temperature, and electron density on the dc conductivity of graphene.

Dedicated to my grandfather, Hossein, for his unwavering support and unique-of-its-kind encouragement from the very first day of school. Looking down from heaven, I'm blissful your dream finally came true upon earning this PhD degree in Physics.

Contents

| | |
|---|------------|
| List of Figures | vii |
| List of Tables | x |
| 1 Introduction | 1 |
| 2 Transport and optical properties of metallic materials | 5 |
| 2.1 Introduction | 5 |
| 2.2 Drude model | 8 |
| 2.3 Plasmons | 11 |
| 2.4 Surface Plasmons | 12 |
| 2.5 Classical TM surface plasmons within Drude model | 15 |
| 3 Quantum Linear Response Theory | 17 |
| 3.1 Introduction | 17 |
| 3.2 Density-density response function | 19 |
| 3.3 Quantum wells, wires, and dots | 21 |
| 3.4 Many-body effects | 22 |
| 3.5 The random-phase approximation | 23 |
| 3.6 Exchange and correlation effects | 26 |
| 3.7 The Lindhard polarization function of a free electron gas | 27 |
| 3.8 Static screening | 29 |
| 4 Carbon allotropes | 30 |
| 4.1 Introduction | 30 |
| 4.2 Graphene | 31 |
| 4.3 The tight-binding model | 32 |
| 4.4 Density of States | 39 |
| 4.5 Lindhard polarization function of graphene | 40 |
| 5 Armchair Graphene Nanoribbons | 42 |
| 5.1 Tight-binding model for AGNRs | 42 |
| 5.2 DOS of AGNRs | 47 |
| 5.3 The k-p method for AGNRs | 49 |
| 5.4 Lindhard polarization function of AGNR | 52 |
| 6 Transport and optical properties of AGNRs | 56 |
| 6.1 Introduction | 56 |
| 6.2 Scattering effect on the polarization function | 61 |

| | | |
|----------|--|------------|
| 6.3 | Reflection amplitude | 62 |
| 6.4 | AGNR surface plasmons | 64 |
| 6.5 | TE transmission and reflection coefficients | 66 |
| 7 | Scattering effects on linear response theory | 67 |
| 7.1 | Introduction | 67 |
| 7.2 | A challenge for quantum linear response theory | 69 |
| 7.3 | Linear response theory in the presence of impurities | 70 |
| 7.4 | Current-current density response | 72 |
| 7.5 | Plasmons in graphene in the presence of impurities | 73 |
| 7.6 | Plasmons in a two-dimensional electron gas | 81 |
| 7.7 | Single- and two-band TM SP | 83 |
| 7.8 | Quality factor | 86 |
| 7.9 | Single- and two-band TE SP | 87 |
| 8 | Quantum Boltzmann equation | 89 |
| 8.1 | Introduction | 89 |
| 8.2 | dc conductivity of graphene in presence of electron-electron interaction | 90 |
| 9 | Conclusions and outlook | 96 |
| | Bibliography | 98 |
| | Appendix A Time ordering operator | 105 |
| | Appendix B Matrix elements of the Coulomb potential of AGNRs | 107 |

List of Figures

| | | |
|-----|--|----|
| 2.1 | The geometry of incident, reflected, and transmitted (a) TM and (b) TE electromagnetic fields in two media with permittivity ϵ_1 and ϵ_2 | 7 |
| 2.2 | Plasmon wave in a metallic system. | 11 |
| 2.3 | TM surface plasmon profile propagating at the interface of two media with permittivities ϵ_1 and ϵ_2 | 13 |
| 2.4 | TM surface plasmon dispersion for a joint dielectric-metallic medium. | 16 |
| 2.5 | (a) Phase matching condition for TM surface plasmon of a joint dielectric-metallic medium. (b) Kretschmann technique geometry. | 16 |
| 3.1 | A schematic of linear response theory for a system which is at equilibrium before the interaction with external perturbation. | 17 |
| 3.2 | Bulk, Quantum well, wire and dot systems. | 22 |
| 3.3 | Sketch of the mean field idea. The real physical system where the interaction gives rise to correlation between the particle motions is shown in left box. The interactions felt by the red particle is replaced by an average interaction due to the average density of the blue particles. | 26 |
| 4.1 | Carbon allotropes. | 31 |
| 4.2 | sp^2 configuration in graphene. | 32 |
| 4.3 | The crystal of arm-chair and zigzag graphene nanoribbons. | 32 |
| 4.4 | Graphene unit cell and its two primitive vectors a_1 and a_2 | 34 |
| 4.5 | The First Brillouin zone of graphene lattice. | 34 |
| 4.6 | The energy spectrum of graphene. | 38 |
| 4.7 | (a) Contour plot of energy spectrum in the Brillouin zone. (b) Graphene spectrum at one of the corner of Brillouin zone which is like a cone. | 39 |
| 4.8 | DOS of graphene (a) and (b) contour plot of its energy spectrum. | 41 |
| 4.9 | Intra- and inter-transitions in the energy spectrum of graphene. | 41 |
| 5.1 | The unit cell and primitive vector of an AGNR. | 42 |
| 5.2 | Energy spectrum of AGNR for (a) $dm = 4$ (b) $dm = 5$ and their DOS. | 47 |
| 5.3 | DOS spectrum for (a) $dm = 4$, (b) $dm = 5$, (c) $dm = 7$, (d) $dm = 10$, (e) $dm = 20$, and (f) $dm = 100$ | 48 |
| 5.4 | (a) Energy spectrum of AGNR for dimmer number $dm = 101$ (b) graphene energy spectrum. | 49 |
| 5.5 | Intra- and inter-transitions in the energy spectrum of AGNR. | 52 |
| 6.1 | An AGNR on a substrate. | 56 |
| 6.2 | An AGNR at the interface of two media with permittivities ϵ_1 and ϵ_2 | 57 |

| | | |
|------|--|----|
| 6.3 | Matrix element of the screened potential vs q/k_F in (a) an AGNR for $dm = 14$, $E_F = 0.1$ eV, and 2D graphene in (b) the RPA and (c) Thomas-Fermi approaches. | 59 |
| 6.4 | 3D surfaces and (ω, q) contour plots of the RPA, Hubbard, and Lindhard conductivities of a metallic AGNR for $dm = 14$ and $E_F = 0.1$ eV. | 60 |
| 6.5 | Cross sections of Fig. 6.4 for (a) $q/k_F = 0.18$ and (b) $\hbar\omega/E_F = 0.48$ | 60 |
| 6.6 | Hubbard conductivity for $dm = 8, 14, 20$ and $E_F = 0.1$ eV. Panel (a) is for fixed $\hbar\omega/E_F = 0.48$ and panel (b) for fixed $q/k_F = 0.18$ | 61 |
| 6.7 | (ω, q) amplitude contour plot of the RPA, Hubbard, and Lindhard conductivities of a metallic AGNR, in the long-wavelength limit, for $dm = 14$ and $E_F = 0.1$ eV. The top panels are for $\gamma' = 0$, the middle ones for $\gamma' = 0.001$, and the bottom panels for $\gamma' = 0.03$ | 62 |
| 6.8 | (ω, q) contour plot of $-\pi\hbar v_F \text{Im} \chi^{RPA}$ for a metallic AGNR with $dm = 14$ and $E_F = 0.1$ eV. The first row of panels is for an <i>unscreened</i> potential with $\gamma' = 0.001, 0.005$, and 0.009 ., the second row for a <i>screened</i> one with $\gamma' = 0.001$ and $k'_s = 0.001, 0.01, 0.1$ | 63 |
| 6.9 | (a) RPA Reflection coefficient for $dm = 14$, $E_F = 0.1$ eV, $n_1 = 2$ and $n_2 = 1$ in the absence of screening and scattering. (b) contour of (a). (c) The solid red curve is a cross section of (a) for $\hbar\omega/E_F = 0.5$ and the dot-dashed blue one the result for a 2D substrate. | 63 |
| 6.10 | (a) TM Lindhard and (b) Hubbard surface plasmon dispersions in a metallic AGNR with $n_1 = 2, n_2 = 1$, and $E_F = 0.1$ eV. From top to bottom the AGNR width is $dm = 5, 8, 20$ | 65 |
| 6.11 | TM Lindhard, RPA, and Hubbard surface plasmon dispersions in a AGNR for $E_F = 0.1$ eV and width $dm = 8$ for (a) $q/k_F \leq 1$ and (b) long wavelength limit, $q/k_F \rightarrow 0$ | 65 |
| 7.1 | Real and imaginary parts of the polarization function $\chi_{non}^{'0,TB}$ in the absence of impurities. | 75 |
| 7.2 | Real parts of χ_{non}^0 and χ_{im}^0 versus ω' where χ_{im}^0 is displayed for several γ' | 75 |
| 7.3 | (a) Real part of the TB DDRF ($\Re\epsilon\chi$) for several values of γ' . (b) A part of (a) for $\omega' \leq 0.4$ | 76 |
| 7.4 | (a) Imaginary part of the TB DDRF, $\Im\mathfrak{m}\chi$, for $q' = 0.01$ and several γ' . (b) A segment of $\Im\mathfrak{m}\chi$ for three γ' | 76 |
| 7.5 | (a) Real and (b) imaginary parts of the TB DDRF versus q' at $\omega' = 0.001$ for several different values of γ' | 77 |
| 7.6 | Real and imaginary parts of the polarization function $\chi_{imp}^{'0,TB}$ in the presence of impurities. | 77 |
| 7.7 | Real and imaginary parts of χ for $\gamma' = 5$ | 78 |
| 7.8 | (a) Real and (b) imaginary parts of the TB DDRF for $\gamma' = 0$ versus ω' . (c)- (d): as in (a) and (b) for $\gamma' = 10$ | 78 |
| 7.9 | (a) SB dispersion relation for several values of γ' . (b) The portion of (a) for $0.03 \leq q' \leq 0.05$ | 80 |
| 7.10 | (a) TB dispersion relation for several values of γ' . (b) The portion of (a) for $0.028 \leq q' \leq 0.05$ | 80 |
| 7.12 | SB and TB plasmon spectra for γ' continuous. | 81 |
| 7.11 | SB and TB critical values γ'_c versus ω' | 81 |

| | | |
|------|---|-----|
| 7.13 | 2DEG plasmon dispersion (a) in the absence and (b) presence of impurity scattering. In (b) $\gamma' = 25$ is used. | 82 |
| 7.14 | γ_c^{2DEG} versus ω' for several values of β' | 83 |
| 7.15 | (a) SB TM SP for different values of γ' . (b) The segment of (a) for $q' \leq 0.006$ | 84 |
| 7.16 | (a) TB TM SP for different values of γ' . (b) The segment of (a) for $q' \leq 0.015$ | 85 |
| 7.17 | 3D bar and (γ', ω') contour plot of TM SB SPs. | 85 |
| 7.18 | 3D bar and (γ', ω') contour plot of TM TB SPs. | 86 |
| 7.19 | Critical impurity strength versus SP frequency. | 86 |
| 7.20 | (a) SB and (b) TB TM SPs QF versus SP frequency for several values of γ' | 87 |
| 8.1 | (a) σ'_{xx} versus temperature for several values of $l_\tau k_F$ for $k_s/k_F = 0.001$ and $E_F = 0.01$ eV. (b) σ'_{xx} versus temperature for several values of k_s/k_F for $l_\tau k_F = 10$ and $E_F = 0.01$ eV | 93 |
| 8.2 | (a) σ'_{xx} versus Fermi energy for several values of $l_\tau k_F$ for $k_s/k_F = 0.001$ and $T = 300$. (b) a segment of (a) in the range of $0.04 \leq E_F \leq 0.06$ eV. | 94 |
| 8.3 | 3D bar of σ'_{xx} (a) versus Fermi energy and temperature for $k_s/k_F = 0.001$ and $l_\tau k_F = 10$. (b) versus Fermi energy and $l_\tau k_F$ for $T = 300$ and $k_s/k_F = 0.001$ | 94 |
| B.1 | Several values of the Fourier components of the Coulomb potential with $dm = 23$ | 109 |
| B.2 | Fourier components of the Coulomb potential, $V_{0,0}(q)$, for several values of dm | 109 |

List of Tables

| | | |
|-----|--|----|
| 3.1 | External perturbation Examples. | 18 |
| 4.1 | Properties of carbon allotropes. | 30 |

1 Introduction

Nowadays, in less than seconds, the most recent news is displayed on our smart phones, laptops, tablettes just a few clicks away. Thousands of books and documents are stored on these devices. We send and receive emails easily, talk to anyone on the other side of the world. Finding any location and the best route has been facilitated by the geographical position system known as GPS. We check the weather forecast whenever we want. Indeed, processing and transferring information is the core of many of our daily activities. So how have we arrived at these technologies and where are we heading from here? To understand, let's review some parts of the history.

Automatic Sequence Controlled Calculator (ASCC) constructed by Howard Aiken at Harvard University in 1944 was the first large-scale digital computer which used electromagnetic relays for storing and processing numbers. However, some problems were associated with these relays; they needed very powerful power pulses to switch them; they would occupy a very large space; and flipping from "off" to "on" would take time. Colossus, a computer invented by a team of English mathematicians, instead of relays used vacuum tubes to switch. In 1946, John Mauchly and J. Presper Eckert from the University of Pennsylvania invented the first fully electronic, general-purpose, digital computer called ENIAC. It weighed almost 30 tons, was around 24 meters long, and contained 18000 vacuum tubes. Its operations time was 5000 cycles per second. The amount of power ENIAC consumed was around 2000 times as much as a laptop. A computer with an order of magnitude faster than ENIAC would had needed approximately millions of vacuum tubes. In 1974, John Bardeen, William Shockley and Walter Brattain were trying to develop a new technology for telephone for amplifying the electrical signals. They used semiconductors to create an amplifier known as point-contact transistor. Transistors have some advantages compared to vacuum tubes. Their size was typically about as big as a bean. In addition, the power consumption of transistors were very low since they used no power when not in operation. However, one major problem remained. All those transistors had to be connected together by wires. Finally, Jack Kilby and Robert Noyce invented integrated circuit (IC) that contained an array of transistors [1, 2, 3, 4].

The building blocks of all contemporary digital electronic device, communications, and circuits which are employed to process, transport, and storage information are formed of metal-oxide-semiconductor field effect transistors (MOSFETs) [5, 6, 7]. Since nowadays many issues in the vast majority of science fields and economy rely on transistors with high clock speed, demand for low cost and high speed MOSFETs with lower power consumption is very strong. The clock speed of information process in transistors directly pertains to the size, miniaturization, and density of comprised elements in it [8]. On the contrary, smaller transistors with high and condensed density of interconnects have high speeds but there is a paramount

challenge related to the interconnect number. By reducing the size of interconnects the delay-time increases and imposes critical limitations to the clock speed frequencies [7]. Reducing the size of semiconductor devices, circuits, and components exerts an influence on their performance and speeds up information processes [8, 9]. Furthermore, size reduction poses major problems such as short-channel effects, gate leakage, and drastically increasing power density [10].

One successful effective solution is to supersede electromagnetic waves as information carriers [8]. Due to their extremely high bandwidth, fibre-optics communication devices can carry information by three orders of magnitude faster than electronic circuits [6]. In addition, in fibre optics light packets carry information they can travel over long distances [7]. These features of fibre optics suggest a synergy between these two technologies [11]. However, because the strength of light-matter interaction in these dielectric materials is not sufficient to exhibit nonlinear behavior, they require high power density and volume which result in limitations on the integration with electronic circuits [12]. The major obstacle is a consequence of the diffraction limit which does not allow to squeeze light in a region smaller than its wavelength [6, 7, 13].

One of the promising solutions is plasmonics waves (PWs) whose wavelength is smaller than that of a free electromagnetic wave. This PW feature plays a pivotal role in many applications, such as integrated photonic systems, biosensing, photovoltaic devices, single-photon transistors for quantum computing, optical modulators, photonic memory devices, surface enhanced Raman spectroscopy [14, 15, 16, 17], and boosting nonlinear optical effects [18]. PWs allow to manipulate and route light on the nanoscale [19, 20, 21, 11, 7]. PWs provide extremely fast processing, in the order of a few femtoseconds [18]. Gold and silver as noble metals are predominant materials for plasmonics. However, they suffer from disadvantages such as high ohmic losses and non-tunability [22]. Size reduction of plasmonic materials give rises to PWs with smaller wavelength. In addition to gold and silver, two-dimensional (2D) plasmonic materials, such as a 2D electron gas (2DEG), polar interfaces of oxides, and oxide nanosheets have more merits than bulk 3D materials. Because of high losses, PWs in 2D materials can be observed just at low temperatures. These PWs lie in the mid-infrared (MIR) wavelength range [10]. Another 2D plasmonic material is graphene that has several advantages, such as high confinement, chemical doping or electrical gating tunability, low losses [22], and terahertz-to-MIR PWs [14, 23] at room temperatures. PWs in graphene can be controlled by doping or electrical gating. The PW dispersion in graphene nanoribbons can be modified by varying their width [24, 25, 26, 27, 28]. The width of the nanoribbons and the type and quality of their edges determine whether they are metallic or semiconducting. The aforementioned studies [24, 25, 26, 27, 28, 29] and many others consider metallic nanoribbons but their existence has been seriously questioned by first-principle and tight-binding band-structure calculations [30] which find that they are semiconducting. Of course such a behaviour is found in nanoribbons created from graphene on a hBN substrate [31]. However, recent experimental studies reported both, (zero gap) metallic and (finite gap) semiconducting nanoribbons for widths as small as 4.5 nm [32]. PW losses in graphene are lower compared with those in noble metals. Scattering, e.g., by impurities, can profoundly affect PWs in it. In literature those effects has been regarded phenomenologically by heuristically introducing a Drude-form conductivity in the long wavelength limit

[33].

The thesis is organized as follows:

In **Chapter 2** we investigate transport and optical properties of metallic materials within Drude model. Then we introduce the concept of plasmons and surface plasmons in classical regime. We present the concept of phase-matching by Kretschmann technique to launch surface plasmons.

Chapter 3 presents the general formalism of the Linear Response Theory. In addition, the concept of quantum wells, wires, and dots will be discussed. Many-body effects within the random-phase and Hubbard approximations will be addressed as well. Finally, in this chapter we present the Lindhard polarization function of an electron gas and static screening within random-phase approximation.

In **Chapter 4** we discuss carbon allotropes. In particular, we talk about striking features of graphene. We show the general application of tight-binding model applied to graphene. By linearizing the energy spectrum of graphene, we obtain the massless Dirac equation. Then, we investigate the density of states in the low energy limit. Finally, we present the polarization function.

In **Chapter 5**, in order to obtain optical properties of AGNRs, through tight-binding model, we evaluate the energy spectrum of AGNRs. Using DOS for several width values, we obtain a general expression to determine whether AGNRs are metals or semiconductors. Then, in the low energy limit, within the $k \cdot p$ method, we evaluate the wave functions and eigenvalues of a metallic AGNR. Finally, we present detailed calculations of the polarization function of an AGNR in the low energy limit.

In **Chapter 6**, using Maxwell's equations for the incoming and outgoing electromagnetic fields, in interaction with a metallic AGNR, and the relationship between the density-density response function and the conductivity, we study surface plasmons in an AGNR within Lindhard, random-phase, and Hubbard approximations. For transverse magnetic modes, we obtain analytical dispersion relations valid for $q \leq k_F$ and assess their width dependence. In all approximations, we include screening. In the long wavelength limit, $q \rightarrow 0$, there is a small but noticeable difference between dispersion relations of the three approximations. In this limit, the respective scattering-free conductivities differ drastically from those obtained in the presence of impurities. The reflection amplitude shows that metallic AGNRs do not support Brewster angles. In addition, AGNRs do not support transverse electric surface plasmons.

In **Chapter 7**, within the linear-response theory, we derive a response function which thoroughly takes into account the influence of elastic scattering that is also valid beyond the long-wavelength limit. We apply the theory to plasmons and surface plasmons in graphene and in the two-dimensional electron gas. The scattering-modified dispersion relation shows that below a critical scattering strength γ_c which is simply related to the plasmon frequency ω , no plasmons are allowed. The critical strength, γ_c , and the allowed (ω, q) plasmon spectra of intra-band and inter-band transitions in graphene are different. In both graphene and the 2DEG, γ_c falls rapidly for small ω 's but much more slowly for large ω 's. We investigate transverse magnetic and transverse electric surface plasmons in graphene at the presence of impurity scattering in the Lindhard approximation. We show how the behaviour and domains of transverse magnetic surface plasmons are altered by the impurity

strength γ and determine the critical value of γ below which no surface plasmons exist. The quality factor of transverse magnetic surface plasmons for single- and two-band cases is shown to be proportional to the square of $\alpha\lambda_{SP}/\gamma$, where α is the fine-structure constant and λ_{SP} the surface plasmon wavelength. Further, we show that impurity scattering suppresses transverse electric surface plasmons.

In **Chapter 8**, we study the homogeneous DC conductivity of graphene using quantum Boltzmann equation via two-body collisions. We investigate the temperature, mean free-path, and screening effect on graphene's DC transport.

Finally, we conclude with highlighting the remarkable results of the thesis in chapter **Chapter 9**.

2 Transport and optical properties of metallic materials

2.1 Introduction

The study and treatment of transport and optical properties of material can be classified in three different approaches. It is worth pointing out that these properties are material response to a stimulus. Indeed, they remain dormant until an external perturbation is exerted on them, which can be dynamic or static. To illustrate a typical static stimulus, a simple wire has no current until an external voltage be applied to it. In addition, if the external voltage varies with time and resulting in alternative current, it will generate an electromagnetic field like what occurs in the radio devices. As a matter of fact, thermodynamically, these properties do not exist in the equilibrium condition. These stimuli and materials can be regarded classically or quantum mechanically. Therefore, the treatment can be totally classical, semi-classical, semi-quantum mechanic, or fully quantum mechanical. If both the external perturbation and material are considered classically we call it the classical regime. In contrast, if both are regarded quantum mechanically it is called the quantum regime. There is a better justification and perspective of the essential physics of what is happening when we first treat the former and latter with the Jaynes-Cummings model but this is beyond the scope of this writing [34, 35].

Transport and optical properties of a material are characterized by two quantities, permittivity and conductivity, respectively [36]. However, in the static regime there is no connection between them whereas in the dynamic regime, these quantities are closely intertwined. We first treat optical properties of a material via employing Maxwell's equations and then we find its relation with the dynamical transport. In particular, these properties are observed in both the classical and quantum mechanical regimes. However, the generated electromagnetic field will be treated classically. Although the following treatments and calculations are valid for magnetic and non-magnetic materials, we limit ourself to the latter case. Maxwell's equations [37] are

$$\vec{\nabla} \cdot \vec{D} = \rho_{ext}, \quad (2.1)$$

$$\vec{\nabla} \cdot \vec{B} = 0, \quad (2.2)$$

$$\vec{\nabla} \times \vec{E} = -\frac{\partial \vec{B}}{\partial t}, \quad (2.3)$$

$$\vec{\nabla} \times \vec{H} = \vec{J}_{ext} + \frac{\partial \vec{D}}{\partial t}, \quad (2.4)$$

where D and B are the electric and magnetic fields within the material, respectively. These quantities pertain to the external electric and magnetic fields through the constructive relations

$$\vec{D} = \epsilon_0 \vec{E} + \vec{P} = \epsilon \epsilon_0 \vec{E}, \quad (2.5)$$

$$\vec{B} = \epsilon_0 \vec{H} + \vec{M} = \mu \mu_0 \vec{H}, \quad (2.6)$$

where P refers to the medium polarization induced by the stimulus and M is the medium magnetization in the absence of an external magnetic field. In addition, ρ_{ext} and J_{ext} in Eqs. (2.1) and (2.4) indicate the external charge and current in the medium where current and electric field are related by

$$\vec{J} = \sigma \vec{E}. \quad (2.7)$$

If we apply the curl operator to both sides of Eq. (2.3)

$$\vec{\nabla} \times (\vec{\nabla} \times \vec{E} = -\frac{\partial \vec{B}}{\partial t}), \quad (2.8)$$

and substitute \vec{B} with Eq. (2.4) on the right hand side, we find

$$\vec{\nabla} \times \vec{\nabla} \times \vec{E} = -\mu \frac{\partial}{\partial t} (\vec{J}_{ext} + \frac{\partial \vec{D}}{\partial t}). \quad (2.9)$$

In the absence of an external charge implying no external current, $J_{ext} = 0$. By employing Eqs. (2.5) and (2.6) the Eq. (2.9) becomes

$$\vec{\nabla}(\vec{\nabla} \cdot \vec{E}) - \vec{\nabla}^2 \vec{E} = -\mu \epsilon \epsilon_0 \frac{\partial^2 \vec{E}}{\partial t^2}. \quad (2.10)$$

One of the possible solutions that satisfies the Eq. (2.10) is given by

$$\vec{E}(\vec{r}, t) = \vec{E}_I e^{i\vec{k} \cdot \vec{r} - i\omega t}, \quad (2.11)$$

where E_I is the amplitude of electromagnetic field. From Eqs. (2.10) and (2.11) we obtain

$$i\vec{k}(i\vec{k} \cdot \vec{E}_I) + k^2 \vec{E}_I = \omega^2 \mu \epsilon \epsilon_0 \vec{E}_I. \quad (2.12)$$

For the transverse electromagnetic (TEM) field, whith the direction of wave propagation, known as the wave-vector \vec{k} , perpendicular to that of the electric and magnetic fields, the first term of Eq. (2.12) is zero. Therefore, the constitutive relation between the wave-vector, permeability, and permittivity for the TEM field is

$$k^2 = \omega^2 \mu \epsilon_0 \epsilon(\vec{k}, \omega), \quad (2.13)$$

where k is the magnitude of the wave-vector. In general, k is a complex quantity

$$k = k_r + ik_i. \quad (2.14)$$

As a matter of fact, Eq. (2.13) indicates that the medium permittivity and permeability are complex quantities

$$\epsilon = \epsilon_r + i\epsilon_i, \quad (2.15)$$

$$\mu = \mu_r + i\mu_i. \quad (2.16)$$

For a non-magnetic medium where $\mu = \mu_0$, from Eqs. (2.13), (2.14), and (2.15) we obtain the following relations

$$k_r = \frac{1}{\sqrt{2}} \frac{\omega}{c} \left[\epsilon_r + \sqrt{\epsilon_r^2 + \epsilon_i^2} \right]^{1/2}, \quad (2.17)$$

$$k_i = \frac{1}{\sqrt{2}} \frac{\omega}{c} \epsilon_i \left[\epsilon_r + \sqrt{\epsilon_r^2 + \epsilon_i^2} \right]^{-1/2}, \quad (2.18)$$

where c is the light speed in vacuum with $c^2 = 1/\epsilon_0\mu_0$. It is worth pointing out that the real and imaginary parts of the wave-vector imply propagation and dissipation of energy in the medium, respectively[38]. Note that, the energy dissipation is connected to the imaginary part of the medium permittivity. The medium refractive index is defined as

$$n = \frac{k}{k_0}, \quad (2.19)$$

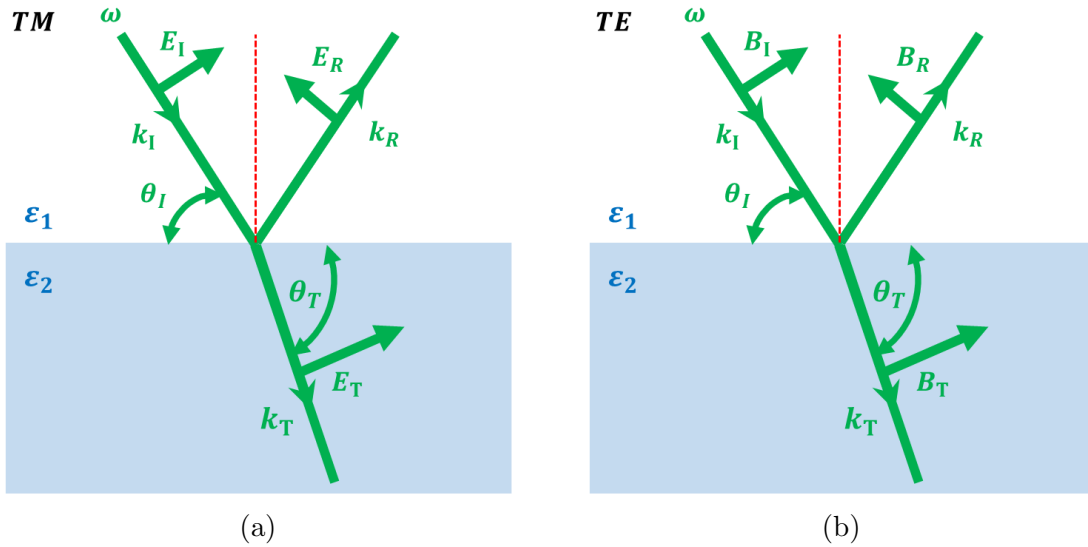


Figure 2.1: The geometry of incident, reflected, and transmitted (a) TM and (b) TE electromagnetic fields in two media with permittivity ϵ_1 and ϵ_2 .

where k_0 is the wave-vector in vacuum. There are two types of TEM electromagnetic fields, TM and TE, that are depicted in Fig. 2.1[39]. In the former the wave-vector and electric field are in the same plane with the magnetic field perpendicular to them. In contrast, in the TE case the magnetic field and wave-vector lie in the same plane with the electric field normal to plane of incident. In some contexts, these TM and TE correspond to the p-polarization and s-polarization respectively.

In addition to TEM electromagnetic fields there is another type for which the wave-vector and electric field are along the same direction. In other words, it is a longitudinal electromagnetic field. The existence of this kind of electromagnetic field can be derived from Eq. (2.1) as

$$i\vec{k} \cdot \epsilon \vec{E} = 0, \quad (2.20)$$

this condition can be satisfied only when ϵ is equal to zero. As we mentioned, there is a close connection between the medium permittivity and conductivity. The bound charges in a medium are related to the polarization by

$$\vec{\nabla} \cdot \vec{P} = -\rho_{bound}. \quad (2.21)$$

Using continuity equation for the current density of bound charges,

$$\vec{\nabla} \cdot \vec{J} = -\frac{\partial \rho_{bound}}{\partial t}, \quad (2.22)$$

we obtain the relation between the current density and the medium polarization

$$\vec{J} = \frac{\partial \vec{P}}{\partial t}. \quad (2.23)$$

From Eqs. (2.5), (2.7) and (2.23) after some simple algebra we obtain

$$\frac{\epsilon(\vec{k}, \omega)}{\epsilon_0} = 1 + \frac{i\sigma(\vec{k}, \omega)}{\epsilon_0 \omega}. \quad (2.24)$$

In the classical regime to obtain the static conductivity it suffices to set the frequency equal to zero, $\omega = 0$. The static conductivity characterizes the inertia of the charge movement in the medium due to the externally applied electric field. Moreover, the static permittivity in both the classical and quantum regimes characterizes the screening of the Coulomb potential [40]. In the classical regime it is constant and equals to ϵ_0 which is independent of the wave-vector. However, it depends on the wave-vector in the quantum regime and can be evaluated either with the random-phase or Hubbard approximations [41].

2.2 Drude model

At the turn of twentieth century Paul Karl Ludwig Drude developed a theory to justify the empirical law of Wiedermann-Franz which states that the ratio of the electrical conductivity to the thermal conductivity at a given temperature is constant for all metals [42]. Ohm's law, Joule heating of metals, equipartition theorem, and the discovery of electron by J.J. Thomson were available at that moment. Although at normal temperature and pressure the electron density in a metals is three order of magnitude larger than in a gas. Drude courageously treated conduction electrons in metals as a gas of negatively charged particles traversing in a medium of uniformly distributed positive ions. He assumed that these positive ions which are required

for charge neutrality are heavier particles, which are immobile and are at rest and do not contribute to the conduction. It should be pointed out that Drude presented his model in 1897, a few years before the plum pudding model by J.J. Thomson and Rutherford model. The former proposed in 1904 and the later in 1909. He constructed his model by applying classical mechanics and the kinetic theory of gas to the electron sea. In the following we review the essential assumptions that he used to picture his model [42, 43, 44].

1. Some fraction of electrons are free. They are not bound to any nuclear sites and they move in a homogeneous potential.
2. For a given electron, its interaction with other electrons and ions between collisions is neglected. The former known as independent electron approximation implying that there is no correlation between the electron momentum before and after the collision. In other words, electron has no “memory”. The latter is known as free electron approximation.
3. Collisions are treated as instantaneous and elastic. It is assumed that after undergoing a collision, an electron instantaneously attains thermal equilibrium with the surrounding. This reflects that after a collision, the electrons have the same temperature as the local environment of the lattice. Furthermore, electrons have a randomly directed velocity, with a kinetic energy given by the appropriate thermodynamic distribution function after collision.
4. Electrons are assumed to experience collisions. The collisions are essential due to increasing kinetic energy as a function of time which imply the energy diverges and this is unphysical. The probability of an electron collision in a time interval dt is dt/τ where τ is known as the mean free time, relaxation time, or collision time. It is assumed that the relaxation time is independent of the electron position and has no dependence on time.

Permittivity and conductivity of a medium in the classical regime can be evaluated within the Drude model. From Newton’s second law of motion, given by

$$m\ddot{\vec{x}} = \vec{F}, \quad (2.25)$$

where F is the total internal and external forces acting on an electron. In general these forces have time and space dependencies. Here we assume that the internal force, which is caused by friction, to be constant and proportional to the electron velocity. For the external force, we suppose that the medium is interacting with an electromagnetic field. Therefore, the electron equation of motion is

$$m\ddot{x} = -m\gamma\dot{x} + qE(x, t), \quad (2.26)$$

where $\gamma\tau = 1$ and $q = -e$, is the electron charge. For simplicity we consider the one-dimensional case which can be easily extended to the three-dimension. In general, the external electromagnetic field can be regarded as a electromagnetic wave packet. Therefore, it is given by

$$E(x, t) = \sum_q \int d\omega E(q, \omega) e^{i(qx - \omega t)}, \quad (2.27)$$

where $E(q, \omega)$ is the Fourier component of the electromagnetic field. Note that, any other external field that acts on an electron can be treated the same way. Here, for simplicity, we limit our calculation to the long wavelength limit. In this limit, the wave-vector of the external field goes to zero, as $q \rightarrow 0$. This means the wavelength of the external field is larger than any system characteristic length such as the unit cell. It is worth remarking that the width of external field that perturbs the system is assumed to be larger than the size of the sample. In other words, all parts of the system is covered by the external field. In this case Eq.(2.27) becomes

$$E(t) = \int d\omega E(\omega)e^{-i\omega t}. \quad (2.28)$$

Since in Eq. (2.25) we expressed the external force in terms of Eq. (2.28), the electron position can be regarded the same way. Therefore, it is given by

$$x(t) = \int d\omega_1 x(\omega_1)e^{-i\omega_1 t}, \quad (2.29)$$

From Eqs.(2.26), (2.28), and (2.29) we arrive at

$$\int d\omega_1 m [-\omega_1^2 - i\gamma\omega_1] x(\omega_1)e^{-i\omega_1 t} = q \int d\omega E(\omega)e^{-i\omega t}. \quad (2.30)$$

If we multiply both sides by $e^{i\omega'' t}$ and integrating over t we obtain

$$\int d\omega_1 m [\omega_1^2 + i\gamma\omega_1] x(\omega_1)\delta(\omega_1 - \omega'') = -q \int d\omega E(\omega)\delta(\omega - \omega''). \quad (2.31)$$

Integration over ω_1 and ω_0 yields

$$x(\omega) = -\frac{q}{m} \frac{E(\omega)}{\omega^2 + i\gamma\omega}. \quad (2.32)$$

We can obtain the medium permittivity, from Eq. (2.5) by first evaluating its polarization, which in the time Fourier space is defined as

$$P(\omega) = qnx(\omega), \quad (2.33)$$

where n is the electron density. Combining Eqs. (2.5), (2.32), and (2.33) leads to

$$\epsilon(\omega)E(\omega) = \epsilon_0 E(\omega) + P(\omega) = \left[\epsilon_0 - \frac{nq^2}{m} \frac{1}{\omega^2 + i\gamma\omega} \right] E(\omega), \quad (2.34)$$

where we find

$$\frac{\epsilon(\omega)}{\epsilon_0} = 1 - \frac{ne^2}{m\epsilon_0} \frac{1}{\omega^2 + i\gamma\omega}. \quad (2.35)$$

From Eq. (2.24) the conductivity is

$$\sigma(\omega) = \frac{\sigma_0}{1 - i\omega\tau}, \quad \sigma_0 = \frac{ne^2\tau}{m}, \quad (2.36)$$

where σ_0 is the static conductivity. From this, we see the ac conductivity reduces the dc one by setting $\omega = 0$. As a matter of fact the real and imaginary parts of conductivity characterize energy dissipation and transport in the medium. Furthermore,

due to the complex nature of the conductivity, there is an attributed phase which indicates the time delay between the applied perturbation field and the medium response. For instance, let's consider the stimuli to be a chromatic electromagnetic field in the long wavelength limit such as

$$E(t) = E \cos(\omega t). \quad (2.37)$$

From Eq. (2.7) we obtain the magnitude of current density

$$J(t) = \frac{\sigma_0}{\sqrt{1 + \omega^2 \tau^2}} E \cos(\omega t - \phi), \quad \phi = \tan^{-1} \left[\frac{\omega \tau}{(1 + \omega^2 \tau^2)^2} \right], \quad (2.38)$$

where ϕ describes the phase difference between the input field and the medium response. The permittivity and conductivity which have been introduced here are only for a metallic medium. One can extend this toy model for dielectric materials by introducing a restoring force in Eq. (2.25) such as, $F_{res} = -m\omega_0^2 \vec{x}$. One then find the following result

$$\frac{\epsilon(\omega)}{\epsilon_0} = 1 - \frac{\omega_p^2}{\omega^2 - \omega_0^2 + i\gamma\omega}. \quad (2.39)$$

which is known as the Lorentz model [45].

2.3 Plasmons

Plasmons are longitudinal electromagnetic waves which originate from coherent collective excitation of charges in a metallic medium about their equilibrium position [38, 42]. In the framework of the classical regime and the Drude model they can be envisaged as depicted in Fig. 2.2 (a).

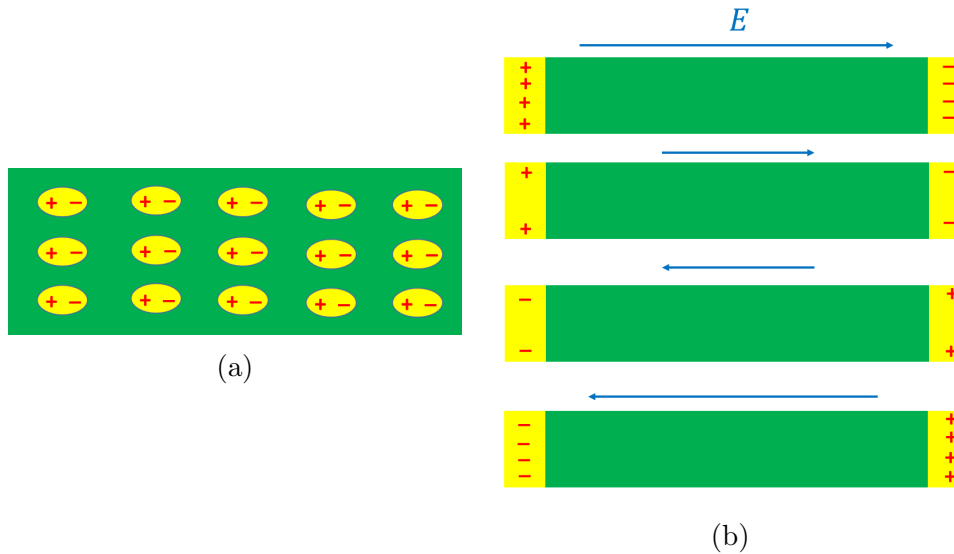


Figure 2.2: Plasmon wave in a metallic system.

In the absence of an external field, the metallic medium is in equilibrium and it is neutral in the sense that it has no extra free charges. By applying a perturbation

which can be an electromagnetic field, beam of electrons, or thermal gradient, momentum would be transferred from this perturbation to the charges and offset them about their equilibrium position. The role of a stimulus can be imagined as a force that acts on an harmonic oscillator. When the mass attached to the spring is pulled and then released, the oscillator starts its harmonic motion in the absence of the external force. The applied perturbation on the metallic medium acts analogue to a harmonic oscillator. The metallic medium is neutral but the external field induces an ensemble of dipole-moments at the nuclear sites which are depicted as the yellow oval shapes in Fig. 2.2 (a). For a simpler description, the former imagination can be visualized as Fig. 2.2 (b) where all internal dipole-moments cancel each other's effect and only that of edges survive. In other words, charges with different signs are accumulated on both sides of the metallic medium. At the beginning of the interaction of stimulus with the metallic medium positive charges accumulate on one side and the negative charge on the other side. Then the generated field in the metallic medium due to this accumulation of charges on both sides exerts a force on them. The negative and positive charges move in parallel and anti-parallel directions of the generated field, respectively. By passing the time the amount of charge on the both sides reduce. Consequently, the strength of the generated field decreases as well. For a moment, the generated field vanishes but due to the acquired momentum negative and positive charges will accumulate on opposite sides compared to earlier. This process continuous for ever if we assume that there is no dissipation in the metallic medium. This oscillation of charge density known as plasma and the quantum of it is called a plasmon. As mentioned, the condition for the existence of a longitudinal electromagnetic wave is given by

$$\epsilon(q, \omega) = 0. \quad (2.40)$$

Within the Drude model, neglecting loss or dissipation means the γ parameter vanishes from Eqs. (2.35) and (2.40) and the plasmon frequency of a metallic medium can be obtained as

$$\omega_p^2 = \frac{ne^2}{m\epsilon_0}, \quad (2.41)$$

where p stands for plasmon. With Eq. (2.41) at our disposal we can rewrite the Drude model as

$$\frac{\epsilon(\omega)}{\epsilon_0} = 1 - \frac{\omega_p^2}{\omega^2 + i\gamma\omega}. \quad (2.42)$$

2.4 Surface Plasmons

A surface plasmon (SP) is an evanescent electromagnetic field propagating between the interface of two media under specific condition, like in a metal-dielectric joint [46]. The most striking feature of surface plasmons is its wavelength which is smaller than that of light in vacuum. In spite of plasmon which exist only in one form where the electric field and propagation are in the same direction, surface plasmon have two types, TM and TE. In the case of TM surface plasmons, the component of electric field which is perpendicular to the interface of two media decays exponentially. The magnetic field components of the TE surface plasmons play the

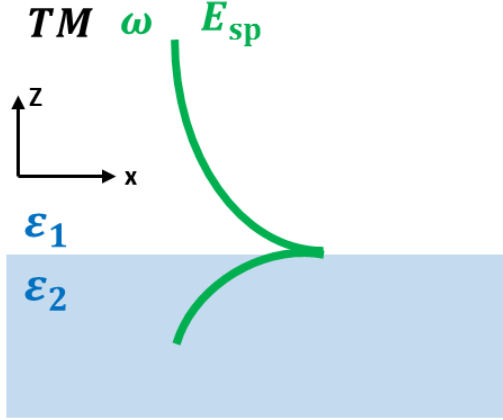


Figure 2.3: TM surface plasmon profile propagating at the interface of two media with permittivities ϵ_1 and ϵ_2 .

same role that of electric field of TM surface plasmons. First we evaluate the TM surface plasmons for the simplest case, consisting of two media with permittivities ϵ_1 and ϵ_2 . Using the time Fourier transform, Eq. (2.10) becomes

$$\vec{\nabla}(\vec{\nabla} \cdot \vec{E}) - \vec{\nabla}^2 \vec{E} = \omega^2 \mu \epsilon \epsilon_0 \vec{E}, \quad (2.43)$$

For TEM electromagnetic fields, it reduces to

$$\vec{\nabla}^2 \vec{E} + \frac{\omega^2}{c^2} \epsilon \vec{E} = 0. \quad (2.44)$$

which is known as Helmholtz equation. First we treat TM surface plasmons and then we treat that of TE surface plasmons. From Eqs. (2.3) and (2.44) for $z > 0$, as shown in Fig. 2.3, the components of electric and magnetic fields are given by

$$H_y(z) = C_2 e^{ik_x x} e^{-k_{2z} z}, \quad (2.45)$$

$$E_x(z) = \frac{iC_2}{\omega \epsilon_1} e^{ik_x x} e^{-k_{2z} z}, \quad (2.46)$$

$$E_z(z) = -\frac{C_2 k_x}{\omega \epsilon_1} e^{ik_x x} e^{-k_{2z} z}. \quad (2.47)$$

For $z < 0$ we have

$$H_y(z) = C_1 e^{ik_x x} e^{k_{1z} z}, \quad (2.48)$$

$$E_x(z) = \frac{iC_1}{\omega \epsilon_2} e^{ik_x x} e^{k_{1z} z}, \quad (2.49)$$

$$E_z(z) = -\frac{C_1 k_x}{\omega \epsilon_2} e^{ik_x x} e^{k_{1z} z}, \quad (2.50)$$

where the frequency and wave-vectors are related by

$$\frac{\omega^2}{c^2} = k_x^2 + k_{iz}^2, \quad i = 1, 2, \quad (2.51)$$

here k_x stands for the surface plasmon wave-vector and k_z is the perpendicular wave-vector. This implies the damping of the surface plasmon field. Furthermore, C_1 and C_2 are constants that can be determined by conservation of energy between the applied perturbation and the surface plasmon. Satisfying the boundary conditions for normal and tangential components of the electric field at $z = 0$ yields

$$\frac{k_{2z}}{k_{1z}} + \frac{\epsilon_1}{\epsilon_2} = 0. \quad (2.52)$$

Since k_{1z} and k_{2z} are positive quantities that satisfy the former condition we can conclude that the permittivity sign for two media need to be different. This implies one of them has to be dielectric and the other one metallic. This is the specific condition mentioned in the definition of surface plasmon. Combining Eqs. (2.51) and (2.52) we obtain the general expression for the TM surface plasmon of two media with permittivities $\epsilon_1(k, \omega)$, and $\epsilon_2(k, \omega)$ which is

$$k_x = \frac{\omega}{c} \sqrt{\frac{\epsilon_1(k, \omega)\epsilon_2(k, \omega)}{\epsilon_1(k, \omega) + \epsilon_2(k, \omega)}}. \quad (2.53)$$

In the same manner, for the TE surface plasmon the Helmholtz equation for the components of the electric and magnetic fields for $z > 0$ become

$$E_y(z) = D_2 e^{ik_x x} e^{-k_{2z} z}, \quad (2.54)$$

$$H_x(z) = -iD_2 \frac{k_{2z}}{\omega\mu_0} e^{ik_x x} e^{-k_{2z} z}, \quad (2.55)$$

$$H_z(z) = D_2 \frac{k_x}{\omega\mu_0} e^{ik_x x} e^{-k_{2z} z}, \quad (2.56)$$

and for $z < 0$ they are

$$E_y(z) = D_1 e^{ik_x x} e^{k_{1z} z}, \quad (2.57)$$

$$H_x(z) = -iD_1 \frac{k_{1z}}{\omega\mu_0} e^{ik_x x} e^{-k_{1z} z}, \quad (2.58)$$

$$H_z(z) = D_1 \frac{k_x}{\omega\mu_0} e^{ik_x x} e^{k_{1z} z}, \quad (2.59)$$

where D_1 and D_2 are constants that need to be determined by energy conservation. Satisfying boundary conditions leads to

$$D_1 (k_{1z} + k_{2z}) = 0. \quad (2.60)$$

Since D_1 cannot be zero, $k_{1z} + k_{2z}$ should be zero but we know that both of k_{1z} and k_{2z} are positive quantities. Therefore, we can conclude that there are no TE surface plasmons at the interface of the two media. One of the interesting things about the TM and TE surface plasmons is that the pole of reflection or transmission of their coefficients gives Eqs. (2.53) and (2.60). For the TM electromagnetic field, using the geometry depicted in Fig.2.1 (a) and satisfying the boundary conditions for the normal and tangential components of the electric field, we obtain

$$t(k, \omega) = 2 \left[\frac{n_2}{n_1} + \frac{\sin \theta_T}{\sin \theta_I} \right]^{-1}, \quad (2.61)$$

$$r(k, \omega) = 1 - \frac{\sin \theta_T}{\sin \theta_I} t(k, \omega), \quad (2.62)$$

where we used Snell's law $n_1 \cos \theta_I = n_2 \cos \theta_T$ and $\theta_I = \theta_R$. Note that here we assume that the two media have constant permittivities such as $n_i^2 \epsilon_0 = \epsilon_i, i = 1, 2$. For the TE electromagnetic field, which is shown in Fig.2.1 (b), the same approach yields

$$1 - r = t \frac{n_1 \sin \theta_T}{n_2 \sin \theta_I}, \quad (2.63)$$

$$1 + r = t. \quad (2.64)$$

Here Snell's law states $\theta_I = \theta_R$ and $n_1 \cos \theta_T = n_2 \cos \theta_I$. There is an advantage to employ this approach instead of Helmholtz equation's solutions. As we mentioned when we were discussing the TM and TE surface plasmons, the constant coefficients $C_1, C_2, D_1,$ and D_2 must be determined through the conservation of energy. However, using the reflection and transmission coefficients it simplifies things further and we will be able to determine the quality factor of the surface plasmons. We follow this approach for evaluating surface plasmons for novel structures.

2.5 Classical TM surface plasmons within Drude model

According to Eq. (2.54) the TM surface plasmons at the interface of two media can be evaluated using the dielectric and metallic permittivities. For simplicity, we assume the dielectric medium to be air, $\epsilon = \epsilon_0$. If we can provide the metallic permittivity using quantum mechanics, then we can find the quantum TM surface plasmon. Here, we use the Drude model to evaluate of permittivity, which is given by Eq. (2.42). From Eqs. (2.42) and (2.53), and neglecting loss and dissipation, ($\gamma = 0$), the spectrum of the TM surface plasmon within the Drude approximation can be evaluated as shown in Fig. 2.4, where the red graph is the surface plasmon dispersion and the blue one is the light dispersion in free space (FS). Note that the surface plasmon frequency and wave-vector are expressed in terms of dimensionless parameters to make the results independent of the electron density. As seen, for a fixed frequency the surface plasmon's wave-vector is larger than that of light in a vacuum. This implies that the surface plasmon wavelength is smaller than that of light. This is the most striking feature of surface plasmons. Due to this we can go beyond the diffraction limit using surface plasmon. Due to this property it can be concluded from the conservation of energy that the strength of surface plasmon field is very large compare to that of light .

There are many techniques to excite and launch surface plasmon, in the following we talk about the Kretschmann technique, the simple technique known [47]. Indeed, to excite a surface plasmon two conditions need to be satisfied; momentum and energy conservations. This is known as the phase matching condition. As mentioned, the surface plasmons wave-vector is larger than that of light. If we want to excite a surface plasmon with light we need to change the tangential component of the light's momentum. In other words, we need to incline the blue line to the green one in Fig. 2.5 (a). This can be achieved by using a prism like what is depicted

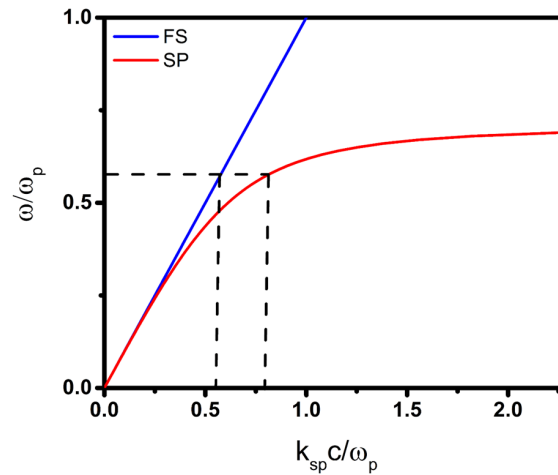


Figure 2.4: TM surface plasmon dispersion for a joint dielectric-metallic medium.

in Fig. 2.5 (b). By changing the incident angle, the slope of the blue line in 2.5 (a) changes. Then at the specific angle where the tangential component of light's momentum becomes equal to the momentum of the surface plasmon provided that the frequency conservation already has been into account. Then a surface plasmon will launch at the interface of two the media.

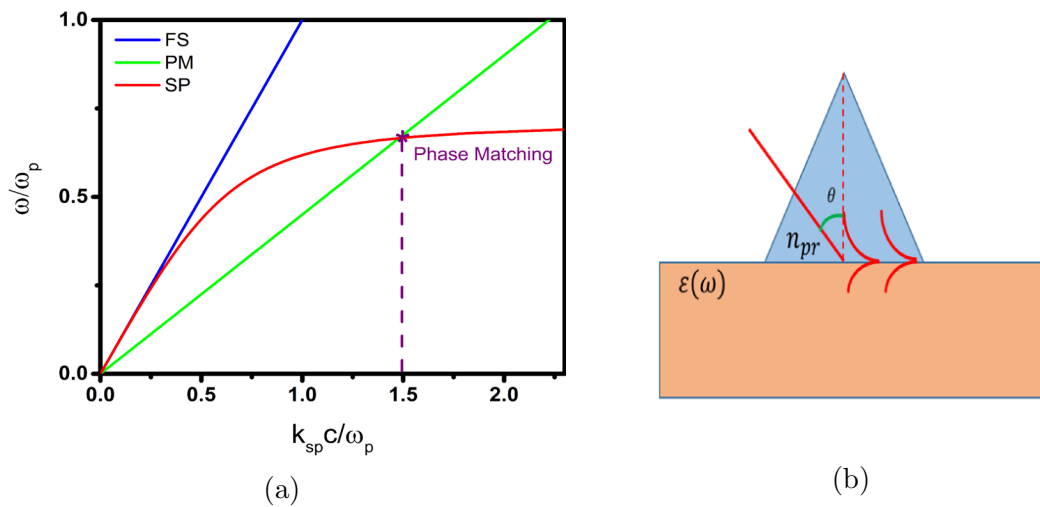


Figure 2.5: (a) Phase matching condition for TM surface plasmon of a joint dielectric-metallic medium. (b) Kretschmann technique geometry.

3 Quantum Linear Response Theory

3.1 Introduction

In the previous chapter we reviewed and treated a classical toy model to explain the transportation and optical properties of a metallic medium. There are also a few quantum mechanical approaches such as quantum Boltzmann equation (QBE), density functional theory, Quantum master equation, and Quantum linear response theory (QLRT) to evaluate these quantities [41, 48, 49, 50, 51]. Linear response theory has a wealth of information and it is very powerful and simple method that can provide for instance, static screening, effective interactions, collective modes, electron energy-loss spectra and Raman spectra at zero and finite temperature. In the following we investigate the main steps in the derivation of QLRT. The main idea in QLRT is that a system is at equilibrium before acting of any external perturbation. If a stimuli at a time like what is shown in Fig. (3.1), t_0 , acts on the system. This couples to a degree of freedom and the system is in a non-equilibrium states.

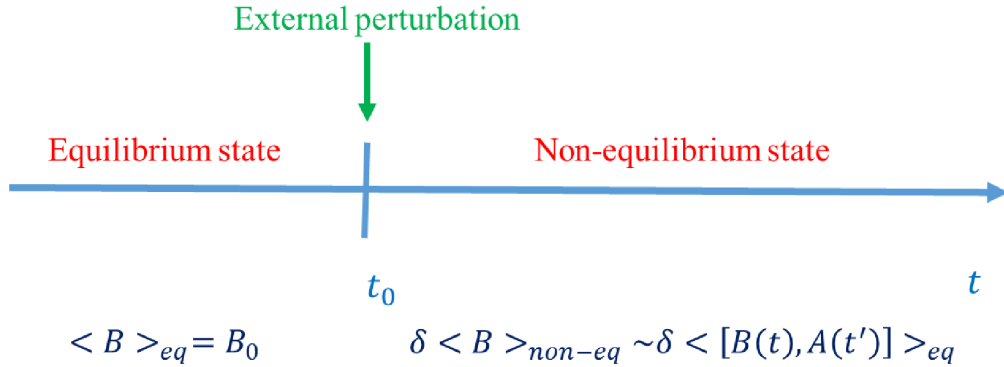


Figure 3.1: A schematic of linear response theory for a system which is at equilibrium before the interaction with external perturbation.

If the stimuli is weak then the new state is close to the equilibrium and we can apply a quantum mechanical perturbation. In other words, in QLRT we suppose that an external field couples to an operator such as A of the system. We are interested in evaluating the value of an operator like B in the time just after the stimuli. The Hamiltonian of the system is given by

$$\hat{H} = \hat{H}_0 + \hat{A}F(t), \quad (3.1)$$

where H_0 is the system Hamiltonian at equilibrium. \hat{A} is an operator of the system which $F(t)$ as an external perturbation couples to it. In particular, when we state

that the external perturbation needs to be weak it means $\langle \hat{A}F(t) \rangle \ll \langle H_0 \rangle$. This external stimuli can be for example an electromagnetic field or a magnetic field that couples to density and magnetic dipole respectively as shown in table. 3.1.

Table 3.1: External perturbation Examples.

| External perturbation | | |
|--|-------------------------------------|--------------------|
| $\hat{A}F(t)$ | $F(t)$ | \hat{A} |
| $\int V_{ext}(\vec{r}, t) \hat{n}(\vec{r}) d\vec{r}$ | $\int V_{ext}(\vec{r}, t) d\vec{r}$ | $\hat{n}(\vec{r})$ |
| $-\vec{M} \cdot \vec{B}_{ext}(t)$ | $-\vec{M} \cdot \vec{B}_{ext}(t)$ | \vec{M} |

Since there is an ensemble, the average value of an operator is given by

$$\langle B \rangle_0 = \frac{1}{Z_0} Tr [\rho_0 B] = \frac{1}{Z_0} \sum_i \langle \psi_i | \hat{B} | \psi_i \rangle e^{-\beta E_i}, \quad (3.2)$$

where $\langle \dots \rangle_0$ stands for an average at thermal equilibrium and $|\psi_i\rangle$ and E_i are the i th eigenfunction and eigenvalue of system respectively at equilibrium. Z_0 is the equilibrium partition function

$$Z_0 = \sum_i e^{-\beta E_i}, \quad (3.3)$$

and ρ_0 is the density operator defined as

$$\rho_0 = e^{-\beta H_0} = \sum_i |i\rangle \langle i| e^{-\beta E_i}, \quad (3.4)$$

with $\beta = 1/k_B T$ where k_B and T are Boltzmann constant and temperature respectively. The expectation value of B over time is given by

$$\langle B \rangle_F(t) = \frac{1}{Z_0} Tr [\rho(t) B] = \frac{1}{Z_0} \sum_i \langle \psi_i(t) | \hat{B} | \psi_i(t) \rangle e^{-\beta E_i}, \quad (3.5)$$

where $|\psi_i(t)\rangle$ is the i th eigenfunction at time t when the system is close to equilibrium. In the interaction picture $|\psi_i(t)\rangle$ and $|\psi_i(0)\rangle$ are related by [52]

$$|\psi_i(t)\rangle = \hat{U}(t, t_0) |\psi_i(0)\rangle, \quad (3.6)$$

where $\hat{U}(t, t_0)$ is a time-evaluation unitary transformation. In the absence of perturbation $\hat{U}(t, t_0)$ is given by

$$\hat{U}(t, t_0) = e^{-i\hat{H}_0(t-t_0)/\hbar}, \quad (3.7)$$

while in its presence is

$$\hat{U}(t, t_0) = e^{-i\hat{H}_0(t-t_0)/\hbar} \hat{U}_F(t, t_0), \quad (3.8)$$

with $\hat{U}_F(t, t_0)$ defined as

$$\hat{U}_F(t, t_0) = T_t \left[\exp \left(-\frac{i}{\hbar} \int_{t_0}^t \hat{A}(t' - t_0) F(t') dt' \right) \right], \quad (3.9)$$

and T_t denoting the time ordering operator, see appendix A. By the first order Eq. (3.9) reduces to

$$\hat{U}_F(t, t_0) = \hat{1} - \frac{i}{\hbar} \int_{t_0}^t \hat{A}(t' - t_0) F(t') dt'. \quad (3.10)$$

From Eqs. (3.2), (3.5), (3.6), and (3.10) by some simple algebra we obtain

$$\langle B \rangle_F(t) - \langle B \rangle_0 = -\frac{i}{\hbar} \int_{t_0}^t \langle [\hat{B}(t), \hat{A}(t')] \rangle_0 F(t') dt'. \quad (3.11)$$

By introducing

$$\langle B \rangle_F(t) - \langle B \rangle_0 \equiv \langle B \rangle_1(t), \quad (3.12)$$

and changing the time variable in Eq.(3.11) like $\tau = t - t_0$ we can rewrite the commutation relation as

$$\langle [\hat{B}(t), \hat{A}(t')] \rangle_0 = \langle [\hat{B}(\tau), \hat{A}] \rangle_0. \quad (3.13)$$

Combining Eqs. (3.11) and (3.12) leads to

$$\langle B \rangle_1(t) = \int_0^{t-t_0} \chi_{BA}(\tau) F(t - \tau) d\tau, \quad (3.14)$$

where $\chi_{BA}(\tau)$ is defined as

$$\chi_{BA}(\tau) \equiv -\frac{i}{\hbar} \Theta(\tau) \langle [\hat{B}(\tau), \hat{A}] \rangle_0, \quad (3.15)$$

where Θ is step function. Physically, χ_{BA} is the response of a system when we are trying to measure the average value of an operator such as B at time τ in the case that an external perturbation has been coupled to an operator like A at an earlier time $t - \tau$. This response is called retarded or causal response due to the aforementioned fact. Since there is no preferential initial time of reference, t_0 , we can set it as $-\infty$ provided that at this time the perturbation vanishes. In other words, the system can be regarded as in equilibrium in the far past, then we can rewrite Eq.(3.15) as

$$\langle B \rangle_1(t) = \int_0^\infty \chi_{BA}(\tau) F(t - \tau) d\tau. \quad (3.16)$$

3.2 Density-density response function

One of the most interesting thing about the response function which has a very close connection with the transportation and optical properties of a system is density-density response function also is known as polarization function. We regard a system whose Hamiltonian is

$$\hat{H} = \hat{H}_0 + \int V_{ext}(\vec{r}', t) \hat{\rho}(\vec{r}') d\vec{r}'. \quad (3.17)$$

Here the polarization function is defined as

$$\chi^0(\vec{r}, t; \vec{r}', t') = -\frac{i}{\hbar} \Theta(t - t') \left\langle \Phi_0 \left| \left[\rho(\vec{r}, t), \rho(\vec{r}', t') \right] \right| \Phi_0 \right\rangle, \quad (3.18)$$

where Φ_0 is the system wave function at equilibrium and ρ is the number density operator which in second quantization formalism is given by

$$\rho(\vec{r}, t) = \psi^\dagger(\vec{r}, t) \psi(\vec{r}, t) = \sum_{ij} c_i^\dagger(t) c_j(t) \phi_i^*(\vec{r}) \phi_j(\vec{r}), \quad (3.19)$$

where c^\dagger and c are creation and annihilation operators and ϕ_i is the system's i th single particle eigenfunction [41, 52, 53]. In addition, the new distribution of the density can be evaluated by

$$\rho_1(\vec{r}, t) = \int_0^\infty d\tau \int d\vec{r}' \chi^0(\vec{r}, \vec{r}', t) V_{ext}(\vec{r}', t - \tau). \quad (3.20)$$

Indeed, χ^0 is proportional to the probability of finding an electron at position \vec{r}' and time t' knowing its position \vec{r} at time t . Here, naught as a superscript means polarization function without regarding any interactions between electrons or environment effects. The quantity in the bracket from Eq. (3.18), by employing (3.19), becomes

$$\sum_{i,j} \sum_{m,n} \left\langle \Phi_0 \left| \left[c_i^\dagger(t) c_j(t) \phi_i^*(\vec{r}) \phi_j(\vec{r}), c_m^\dagger(t') c_n(t') \phi_m^*(\vec{r}') \phi_n(\vec{r}') \right] \right| \Phi_0 \right\rangle. \quad (3.21)$$

Since commutation has no effect on the single particle wave function they can be extracted. This simplifies the result and leads to

$$\sum_{i,j} \sum_{m,n} \phi_i^*(\vec{r}) \phi_j(\vec{r}) \phi_m^*(\vec{r}') \phi_n(\vec{r}') \left\langle \Phi_0 \left| \left[c_i^\dagger(t) c_j(t), c_m^\dagger(t') c_n(t') \right] \right| \Phi_0 \right\rangle. \quad (3.22)$$

The time evolution of an operator is given by [41, 52]

$$c_l(t) = e^{iH_0 t/\hbar} c_l e^{-iH_0 t/\hbar} = c_l e^{-iE_l t/\hbar}, \quad (3.23)$$

where substituting it into Eq.(3.22) gives rise to

$$\sum_{i,j} \sum_{m,n} \phi_i^*(\vec{r}) \phi_j(\vec{r}) \phi_m^*(\vec{r}') \phi_n(\vec{r}') e^{-i(E_i - E_j)(t - t')/\hbar} \left\langle \Phi_0 \left| \left[c_i^\dagger c_j, c_m^\dagger c_n \right] \right| \Phi_0 \right\rangle. \quad (3.24)$$

The expression in the above commutation by some simple algebra becomes

$$\left[c_i^\dagger c_j, c_m^\dagger c_n \right] = (c_i^\dagger c_i - c_j^\dagger c_j) \delta_{i,n} \delta_{j,m} = (\hat{n}_i - \hat{n}_j) \delta_{ni} \delta_{jm}, \quad (3.25)$$

where \hat{n} indicate the number operator and δ is the Kronecker delta. The thermal average of Eq. (3.25) yields

$$\left\langle \Phi_0 \left| \left[c_i^\dagger c_j, c_m^\dagger c_n \right] \right| \Phi_0 \right\rangle = (f_i - f_j) \delta_{ni} \delta_{jm}, \quad (3.26)$$

where f denotes the Fermi-Dirac distribution function

$$f_i = \frac{1}{e^{\beta(E_i - \mu)} + 1}, \quad (3.27)$$

with μ being the chemical potential. From Eqs. (3.26) and (3.22) we can evaluate the polarization function which is given by

$$\chi^0(\vec{r}, t; \vec{r}', t') = -\frac{i}{\hbar} \Theta(t - t') \sum_{i,j} \phi_i^*(\vec{r}) \phi_j(\vec{r}) \phi_j^*(\vec{r}') \phi_i(\vec{r}') e^{-i(E_i - E_j)(t - t')/\hbar} (f_i - f_j). \quad (3.28)$$

By modifying the time it can be rewritten as

$$\chi^0(\vec{r}, t; \vec{r}', t') = \chi^0(\vec{r}, t - t'; \vec{r}', 0) = \chi^0(\vec{r}, \vec{r}', t), \quad (3.29)$$

where its time Fourier component is given by

$$\chi^0(\vec{r}, \vec{r}', \omega) = \int_{-\infty}^{\infty} \chi^0(\vec{r}, \vec{r}', t) e^{i\omega t} dt. \quad (3.30)$$

According to Eq. (3.30) by some algebra we can obtain the time Fourier component of the polarization function

$$\chi^0(\vec{r}, \vec{r}', \omega) = \lim_{\nu \rightarrow 0} \sum_{i,j} \frac{(f_i - f_j)}{E_i - E_j + \hbar(\omega + i\nu)} \phi_i^*(\vec{r}) \phi_j(\vec{r}) \phi_j^*(\vec{r}') \phi_i(\vec{r}'), \quad (3.31)$$

where parameter ν has been introduced in the integration over time to avoid the divergence and to satisfy causality. Here, we rename χ^0 to χ_{non}^0 , to indicate this is for the case of no impurities or collisions

$$\chi^0(\vec{r}, \vec{r}', \omega) = \chi_{non}^0(\vec{r}, \vec{r}', \omega). \quad (3.32)$$

In addition to the time Fourier, the space Fourier can be calculated by

$$\chi(\vec{q}, \vec{q}', \omega) \equiv \frac{1}{L^d} \int d^d r e^{-i\vec{q} \cdot \vec{r}} \int d^d r' e^{i\vec{q}' \cdot \vec{r}'} \int_0^{\infty} dt \chi(\vec{r}, \vec{r}', t) e^{i\omega t}. \quad (3.33)$$

Since $\chi(\vec{r}, \vec{r}', t)$ only depends on the difference of $\vec{r} - \vec{r}'$ the above integral vanishes unless $\vec{q} = \vec{q}'$ which implies

$$\chi(\vec{q}, \vec{q}', \omega) = \frac{1}{V^d} \chi(\vec{q}, \omega) \delta_{\vec{q}, \vec{q}'}, \quad (3.34)$$

where V^d denotes the volume in dimensions. Note that $\chi_{non}^0(\vec{q}, \omega)$ is known as the Lindhard polarization function.

3.3 Quantum wells, wires, and dots

In a bulk system electrons are treated as free electron gas whose wave functions are plane waves with energy $E = \hbar^2 k^2 / 2m$ where k is the amplitude of their wave-vector. However, if the motion of electrons is restricted by imposing potentials on directions of motions which are on the order of the de Broglie wavelength, this results

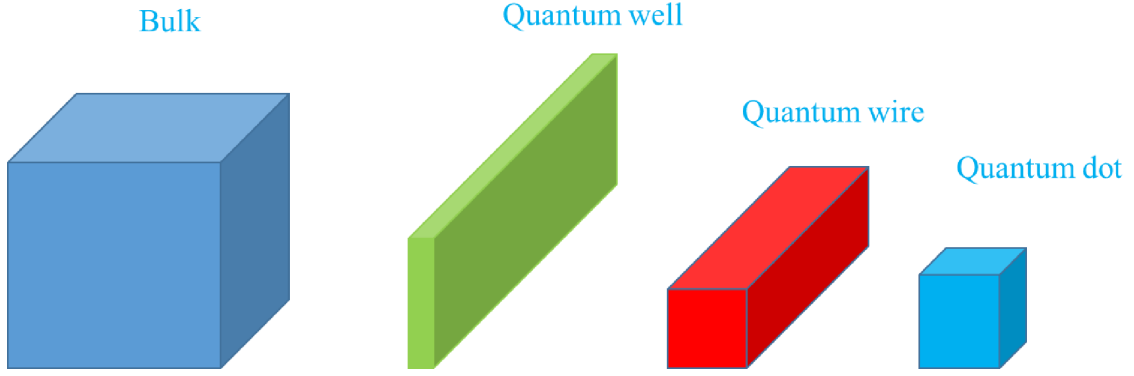


Figure 3.2: Bulk, Quantum well, wire and dot systems.

in drastic changes in transport and optical properties of the system. If the electrons' motion becomes limited as shown in Fig. 3.2 in one, two, or three dimensions, these new systems are known as quantum wells, wires, and dots respectively. In the case where the electron-ion interaction is disregarded the bulk, quantum well and quantum wire can also be considered as electron gases in 3D, 2D and 1D respectively [45, 54]. In spite of the bulk system which has a continuous quantum number, in these novel structures there is at least one discrete quantum number which refers to sub-band. The wave function of an electron gas in these systems is given by

$$\Psi(\vec{r}) = \begin{cases} C_{3D}e^{i\vec{k}\cdot\vec{r}} & 3D, \\ C_{2D}e^{i(k_x x + k_y y)}\phi_l(z) & 2D, \\ C_{1D}e^{i(k_x x)}\phi_l(z)\phi_m(y) & 1D, \end{cases} \quad (3.35)$$

where $\phi_l(z)$ and $\phi_m(y)$ are the eigenvalues in the z and y directions that can be determined according to the boundary conditions that are imposed on the system. In addition, C_{3D} , C_{2D} , and C_{1D} can be evaluated through normalization of the wave function. The energy eigenvalues of these systems are

$$E = \begin{cases} \frac{\hbar^2 k^2}{2m}, & \vec{k} = k_x \hat{e}_x + k_y \hat{e}_y + k_z \hat{e}_z, & 3D, \\ \frac{\hbar^2 k^2}{2m} + E_l, & \vec{k} = k_x \hat{e}_x + k_y \hat{e}_y, & 2D, \\ \frac{\hbar^2 k^2}{2m} + E_l + E_m, & \vec{k} = k_x \hat{e}_x, & 1D, \end{cases} \quad (3.36)$$

where E_l and E_m are eigenvalues in the z and y directions. Furthermore, the Fermi wave-vector for these systems at zero temperature is related to the electron density, n , by

$$k_F = \begin{cases} (3\pi^2 n)^{\frac{1}{3}}, & 3D, \\ (2\pi n)^{\frac{1}{2}}, & 2D, \\ n\pi/2, & 1D. \end{cases} \quad (3.37)$$

3.4 Many-body effects

Many-body effects such as Coulomb potential between electron-electron, electron-ion, ion-ion, or impurity and defects, or even electron-phonon coupling have profound

impacts on the transport and optical properties of the novel structure. Here we address the question of when many-body effects become important? The Hamiltonian of a many-body system, in the simplest case where only the Coulomb potential between electrons has been regarded and is given by

$$H = \sum_{i=1}^N \frac{p_i^2}{2m} + \frac{e^2}{4\pi\epsilon_0} \sum_{i<j} \frac{1}{|\vec{r}_i - \vec{r}_j|} \quad (3.38)$$

where p_i and \vec{r}_i indicate the momentum and position of the i th electron. By introducing the dimensionless parameters for momentum and position such as $\vec{P} = \vec{p}/r_s a_B$ and $\vec{R} = \vec{r}/r_s a_B$ where a_B and r_s refer to Bohr and Wigner-Seitz radii [42]. Therefore, by these dimensionless parameters Eq.(3.38) can be rewritten

$$H = \frac{Ry}{r_s^2} \left[- \sum_{i=1}^N \nabla_{\vec{R}}^2 + r_s \sum_{i<j} \frac{1}{|\vec{R}_i - \vec{R}_j|} \right], \quad (3.39)$$

where Ry is the Rydberg energy and r_s indicates the radius of an imaginary sphere whose volume is equal to that of an electron. There is a very constructive relation between this natural length, $r_s a_B$, and the electron density in 3D, 2D, and 1D which is given by

$$\frac{1}{n} = \begin{cases} 4\pi(r_s a_B)^3/3, & 3D, \\ \pi(r_s a_B)^2, & 2D, \\ 2r_s a_B, & 1D. \end{cases} \quad (3.40)$$

According to Eq.(3.39) when r_s becomes negligible, the Coulomb potential can be neglected and the system can be treated as an electron gas. We can see from Eq. (3.40) in the 3D $r_s \sim n^{-1/3}$. Since the electron density is high the second term in the Hamiltonian can be disregarded. However, for 2D and 1D r_s has a meaningful value that cannot be neglected. Therefore, many-body effects show important impacts on all properties of the system. Indeed, we expect that due to the fact that the Fermi-wavelength for the 1D system is much greater than of the 2D. In the similar way, the Fermi wavelength of the 2D is larger than of the 3D as indicated in Eq. (3.37).

3.5 The random-phase approximation

When the Coulomb potential term in the Hamiltonian becomes important, we should come up with a new, powerful and brilliant approach to solve it. Since we are dealing with a system with particle number on the order of 10^{23} where even with the most advanced modern computers, we are unable to solve it exactly. Therefore, we have to employ some approximations to resolve this issue, to obtain some constructive and intuitive results that can tell us about this many-body effect on system's properties. In other word, how does this many-body effect modify the system polarization function and what is the connection between the new and old polarization function? Indeed, when an external field is applied and coupled to a system, it induces a new charge distribution which renders a Coulomb potential

originated from this distribution. Then, we can express the total potential seen by a typical electron in the system by

$$V_{sc}(\vec{r}, t) = V_{ext}(\vec{r}, t) + \frac{e^2}{4\pi\epsilon_0} \int d^d r' \frac{\delta\rho(\vec{r}', t)}{|\vec{r} - \vec{r}'|}, \quad (3.41)$$

where $V_{sc}(\vec{r}, t)$ indicates the total potential. On the right hand side of Eq. (3.41), V_{ext} refers to external potential and second term states the mean field theory concept which has been employed implicitly [52]. Indeed, mean field theory says that the effect of other particles is included as a mean density. This concept is depicted in Fig. 3.3 schematically. The relation between the induced charged, $\delta\rho$, and the external potential is given by

$$\delta\rho(\vec{r}, t) = \int dt \int d^d r' \chi(\vec{r}, \vec{r}', t, t') V_{ext}(\vec{r}', t'), \quad (3.42)$$

where χ is the system polarization function. From Eq. (2.1) we have

$$\vec{\nabla}^2 V_{sc}(\vec{r}, t) = -e\delta(\vec{r}, t)/\epsilon_0. \quad (3.43)$$

If we take the space and time Fourier transforms of Eq. (3.43)

$$-q^2 V_{sc}(\vec{q}, \omega) = -e\delta(\vec{q}, \omega)/\epsilon_0, \quad (3.44)$$

the Fourier transform of Eq. (3.42)

$$\delta\rho(\vec{q}, \omega) = \chi(\vec{q}, \omega) V_{ext}(\vec{q}, \omega), \quad (3.45)$$

and the Fourier transform of the external potential

$$V_{ext}(\vec{q}, \omega) = \int d^d r e^{i\vec{q}\cdot\vec{r}} \int e^{i\omega t} V_{ext}(\vec{r}, t), \quad (3.46)$$

then combing Eqs. (3.44), (3.45), and (3.46) and applying them to the Fourier transform of Eq. (3.41) we obtain

$$V_{sc}(\vec{q}, \omega) = V_{ext}(\vec{q}, \omega) + V(q)\delta\rho(\vec{q}, \omega) = [1 + V(q)\chi(\vec{q}, \omega)] V_{ext}(\vec{q}, \omega), \quad (3.47)$$

where $V(q)$ indicates the Fourier components of the Coulomb potential. Eq. (3.47) can be rewritten in a more compact form

$$V_{sc}(\vec{q}, \omega) = \frac{V_{ext}(\vec{q}, \omega)}{\epsilon(\vec{q}, \omega)}, \quad (3.48)$$

where $\epsilon(\vec{q}, \omega)$ is given by

$$\epsilon^{-1}(\vec{q}, \omega) = 1 + V(q)\chi(\vec{q}, \omega). \quad (3.49)$$

It is worth to point out that Eq. (3.48) indicates the fact that the external potential has been modified. In other words, it has been screened. The subscript *SC* in Eq. (3.41) stands for the screened potential. The total potential seen by an electron in the system is this screened potential.

To obtain the polarization function when the Coulomb potential is already regarded we can rewrite the induced charge density in term of the “proper” density response, $\tilde{\chi}(\vec{q}, \omega)$, which is given by

$$\delta\rho(\vec{q}, \omega) = \tilde{\chi}(\vec{q}, \omega)V_{sc}(\vec{q}, \omega). \quad (3.50)$$

If we replace $\delta\rho(\vec{q}, \omega)$ and $V_{sc}(\vec{q}, \omega)$ from Eqs. (3.45) and (3.47), respectively, we arrive at

$$\chi(\vec{q}, \omega) = \tilde{\chi}(\vec{q}, \omega)[1 + V(q)\chi(\vec{q}, \omega)], \quad (3.51)$$

where it can be written in the following form

$$\chi(\vec{q}, \omega) = \frac{\tilde{\chi}(\vec{q}, \omega)}{1 - V(q)\tilde{\chi}(\vec{q}, \omega)}. \quad (3.52)$$

Within the random-phase approximation (RPA) [41, 55, 56], one approximates the proper polarization function to be equal to non-interacting polarization function, in the sense that the induced charge density can be expressed by

$$\delta\rho(\vec{q}, \omega) = \tilde{\chi}(\vec{q}, \omega)V_{sc}(\vec{q}, \omega) \simeq \chi^0(\vec{q}, \omega)V_{sc}(\vec{q}, \omega), \quad (3.53)$$

where the connection between the RPA polarization function and that of the non-interacting is given by

$$\chi^{RPA}(q, \omega) = \frac{\chi^0(q, \omega)}{1 - V(q)\chi^0(q, \omega)}. \quad (3.54)$$

As seen, within the RPA the effect of the Coulomb potential changes the polarization function. As we mentioned, all optical properties can be obtain from the system permittivity. Here we find the relation between the permittivity and the proper polarization function. From Eqs. (3.49) and (3.52) by some algebra we can obtain

$$\epsilon(\vec{q}, \omega) = 1 - V(q)\tilde{\chi}(\vec{q}, \omega), \quad (3.55)$$

where within the RPA it becomes

$$\epsilon^{RPA}(\vec{q}, \omega) = 1 - V(q)\chi^0(\vec{q}, \omega). \quad (3.56)$$

Here we represent the relation between the system conductivity and its polarization function. The space and time Fourier transforms of the current density continuity equation is

$$i\vec{q} \cdot \vec{J}(\vec{q}, \omega) - i\omega\rho(\vec{q}, \omega) = 0. \quad (3.57)$$

If we express the current density in terms of the conductivity, electric field, and density we find from Eq. (3.45)

$$\sigma(\vec{q}, \omega)\vec{q} \cdot \vec{E}(\vec{q}, \omega) = \omega\chi(\vec{q}, \omega)V_{ext}(\vec{q}, \omega), \quad (3.58)$$

where by substituting the Fourier transform of $E(\vec{r}, t) = -\vec{\nabla}V_{ext}(\vec{r}, t)$, the above equation yields

$$\sigma(\vec{q}, \omega) = \frac{ie^2\omega\chi(\vec{q}, \omega)}{q^2}. \quad (3.59)$$

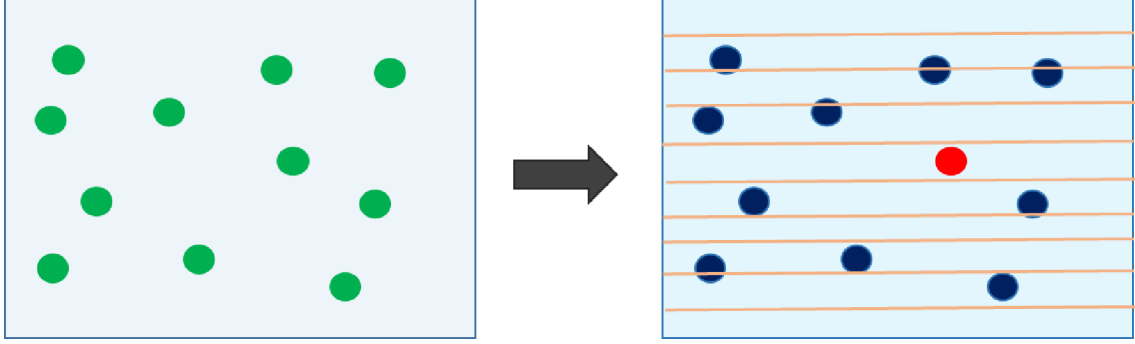


Figure 3.3: Sketch of the mean field idea. The real physical system where the interaction gives rise to correlation between the particle motions is shown in left box. The interactions felt by the red particle is replaced by an average interaction due to the average density of the blue particles.

One can obtain the conductivity within the Lindhard and RPA by substituting Eqs. (3.32) and (3.54) respectively into Eq.(3.59). In other words, they are given by

$$\sigma^0(\vec{q}, \omega) = \frac{ie^2\omega\chi^0(\vec{q}, \omega)}{q^2}, \quad (3.60)$$

$$\sigma^{RPA}(\vec{q}, \omega) = \frac{ie^2\omega\chi^{RPA}(\vec{q}, \omega)}{q^2}. \quad (3.61)$$

3.6 Exchange and correlation effects

If electrons in the system were distinguishable the average interaction energy of an electron with the positively charged background would be canceled. However, it has been observed that even in the absence of the Coulomb interaction the amount of total energy is less than what is expected. According to the Pauli exclusion principle the wave function of an electron system need to be anti-symmetry which implies that there is a high degree of correlation between the positions of two electrons with the same spin orientation. Therefore, there is a region where the density of the same-spin electron is smaller than average. In other words, each electron is surrounded by an hole which is known also “exchange hole”. This gives rise to the fact that the positive background charge is not exactly canceled. The interaction of an electron surrounded by the exchange hole with the positive charge yields to the exchange energy [40, 41]. This alters the polarization function of a system. Indeed, the exchange and correlation effects can be introduced by local field factor where modifies the polarization function as

$$\chi(q, \omega) = \frac{\chi^0(q, \omega)}{1 - V(q) [1 - G_+(q, \omega)] \chi^0(q, \omega)}, \quad (3.62)$$

where G_+ is

$$G_+ = \frac{G_{\uparrow\uparrow} + G_{\uparrow\downarrow}}{2}. \quad (3.63)$$

\uparrow and \downarrow are symbols for the spin up and down respectively. The proper polarization function is given by

$$\tilde{\chi}(\vec{q}, \omega) = \frac{\chi^0(q, \omega)}{1 + V(q)G_+(q, \omega)\chi^0(q, \omega)}, \quad (3.64)$$

and for the permittivity we have

$$\epsilon(q, \omega) = 1 - \frac{V(q)\chi^0(q, \omega)}{1 + V(q)G_+(q, \omega)\chi^0(q, \omega)}. \quad (3.65)$$

If one, for simplicity, assume that the local field factor be frequency independent then it yields to the Hubbard approximation

$$G(q, \omega) \approx G(q), \quad (3.66)$$

which for 3D, 2D, and 1D systems is [57]

$$G(q) = \begin{cases} q^2/q^2 + k_F^2, & 3D, \\ q/\sqrt{q^2 + k_F^2}, & 2D, \\ V(\sqrt{q^2 + k_F^2})/2V(q), & 1D. \end{cases} \quad (3.67)$$

In the Hubbard approximation Eqs. (3.62) and (3.65) become

$$\chi^{Hub}(q, \omega) = \frac{\chi^0(q, \omega)}{1 - V(q)[1 - G(q)]\chi^0(q, \omega)}, \quad (3.68)$$

$$\epsilon^{Hub}(q, \omega) = 1 - \frac{V(q)\chi^0(q, \omega)}{1 + V(q)G(q)\chi^0(q, \omega)}. \quad (3.69)$$

3.7 The Lindhard polarization function of a free electron gas

According to Eq. (3.31) in order to obtain the polarization function of a system we need the single-particle wave function and energy spectrum which for a free electron gas are

$$\phi_{\vec{k},s}(\vec{r}) = \frac{e^{i\vec{k}^d \cdot \vec{r}}}{\sqrt{L^d}} X_s, \quad E_{\vec{k},s} = \frac{\hbar^2 |\vec{k}^d|^2}{2m}, \quad (3.70)$$

where L is the system length. Here d denotes the dimension and subscript s indicates the spin eigenvalue. Here for the free electron gas in 2D and 1D we limit our calculation to one sub-band. By employing Eq. (3.70) and setting it into Eq. (3.31) we obtain

$$\chi_{non}^0(\vec{r}, \vec{r}', \omega) = \lim_{\nu \rightarrow 0} \sum_{\vec{k},s} \sum_{\vec{k}',s'} \frac{(f_{\vec{k},s} - f_{\vec{k}',s'})}{E_{\vec{k},s} - E_{\vec{k}',s'} + \hbar(\omega + i\nu)}$$

$$\times \left(\frac{1}{L^d} \right)^2 e^{i(\vec{k}' - \vec{k}) \cdot \vec{r}} e^{-i(\vec{k}' - \vec{k}) \cdot \vec{r}'} \underbrace{(X_s^\dagger X_{s'})^2}_{\delta_{ss'}}, \quad (3.71)$$

where $\delta_{ss'}$ refers to the Kronecker delta. By taking its space Fourier transform we arrive at

$$\chi_{non}^0(\vec{q}, \omega) = \chi_{non}^0(q, \omega) = \lim_{\nu \rightarrow 0} \frac{1}{L^d} \sum_{\vec{k}, s} \frac{(f_{\vec{k}, s} - f_{\vec{k} + \vec{q}, s})}{E_{\vec{k}, s} - E_{\vec{k} + \vec{q}, s} + \hbar(\omega + i\nu)}, \quad (3.72)$$

where, by some algebra, it can be rewritten as

$$\chi_{non}^0(q, \omega) = \lim_{\nu \rightarrow 0} \frac{1}{L^d} \sum_{\vec{k}, s} f_{\vec{k}, s} \left[\frac{1}{E_{\vec{k}, s} - E_{\vec{k} + \vec{q}, s} + \hbar(\omega + i\nu)} + \frac{1}{E_{\vec{k}, s} - E_{\vec{k} - \vec{q}, s} - \hbar(\omega + i\nu)} \right]. \quad (3.73)$$

Using the identity

$$\lim_{\nu \rightarrow 0} \frac{1}{a \pm i\nu} = \text{P.V.} \frac{1}{a} \mp i\pi\delta(a), \quad (3.74)$$

we can separate real and imaginary parts of polarization function

$$\Re\chi^0(q, \omega) = \frac{1}{L^d} \sum_{\vec{k}, s} f_{\vec{k}, s} \left[\frac{1}{E_{\vec{k}, s} - E_{\vec{k} + \vec{q}, s} + \hbar\omega} + \frac{1}{E_{\vec{k}, s} - E_{\vec{k} - \vec{q}, s} - \hbar\omega} \right], \quad (3.75)$$

$$\Im\chi^0(q, \omega) = -\frac{\pi}{L^d} \sum_{\vec{k}, s} f_{\vec{k}, s} \left[\delta \left(E_{\vec{k}, s} - E_{\vec{k} + \vec{q}, s} + \hbar\omega \right) - \delta \left(E_{\vec{k}, s} - E_{\vec{k} - \vec{q}, s} - \hbar\omega \right) \right], \quad (3.76)$$

where $\delta(a)$ is Delta function. To simplify things we limit our calculation at zero temperature. For the 3D free electron gas real and imaginary parts are given by Refs. [41, 58]

$$\Re\chi^0(q', \omega') = N_3 \left[\frac{1 - \omega'^2_-}{4q'} \ln \left| \frac{\omega'_- + 1}{\omega'_- - 1} \right| - \frac{1 - \omega'^2_+}{4q'} \ln \left| \frac{\omega'_+ + 1}{\omega'_+ - 1} \right| - \frac{1}{2} \right], \quad (3.77)$$

$$\Im\chi^0(q', \omega') = \frac{\pi N_3}{4q'} \left[(1 - \omega'^2_+) \Theta(1 - \omega'^2_+) - (1 - \omega'^2_-) \Theta(1 - \omega'^2_-) \right], \quad (3.78)$$

where Θ is the step function. For the 2D free electron gas they are

$$\Re\chi^0(q', \omega') = \frac{N_2}{q'} \left[\frac{\omega'_+}{|\omega'_+|} \Theta(\omega'^2_+ - 1) \sqrt{\omega'^2_+ - 1} - \frac{\omega'_-}{|\omega'_-|} \Theta(\omega'^2_- - 1) \sqrt{\omega'^2_- - 1} - q' \right], \quad (3.79)$$

$$\Im\chi^0(q', \omega') = \frac{N_2}{q'} \left[(1 - \omega'^2_+) \Theta(1 - \omega'^2_+) - (1 - \omega'^2_-) \Theta(1 - \omega'^2_-) \right], \quad (3.80)$$

and finally for the 1D free electron gas the results are

$$\Re\chi^0(q', \omega') = \frac{N_1}{2q'} \left[\ln \left| \frac{\omega'_+ - 1}{\omega'_+ + 1} \right| - \ln \left| \frac{\omega'_- - 1}{\omega'_- + 1} \right| \right], \quad (3.81)$$

$$\Im\chi^0(q', \omega') = \frac{N_1\pi}{2q'} \left[\Theta(1 - \omega'^2_+) - \Theta(1 - \omega'^2_-) \right], \quad (3.82)$$

where N_d , q' , and ω'_\pm are

$$N_d = \frac{nd}{2E_F}, \quad q' = \frac{q}{k_F}, \quad \omega'_\pm = \frac{\omega}{qv_F} \pm \frac{q}{2k_F}, \quad (3.83)$$

where E_F and k_F refer to the Fermi energy and wave-vector.

3.8 Static screening

Eq.(3.48) enables us to evaluate the static screening by setting $\omega = 0$, which results in

$$V_{sc}(\vec{q}) = \frac{V_{ext}(\vec{q})}{\epsilon(\vec{q})}, \quad (3.84)$$

where $V_{ext}(\vec{q})$ is the bare Coulomb interaction. For the 3D free electron gas, within the RPA it can be shown

$$\epsilon(\vec{q}) = 1 - V(q)\chi^0(\vec{q}) = 1 + \frac{\kappa^2}{q^2}, \quad (3.85)$$

with

$$\kappa = \sqrt{\frac{4\pi e^2}{\epsilon_0} \frac{\partial n}{\partial \mu}}. \quad (3.86)$$

Here n and μ are electron number density and Fermi energy, respectively [45]. Combining Eqs. (3.84) and (3.85), then taking its Fourier transform we obtain

$$V_{sc}(r) = \frac{e^2}{\epsilon_0 r} e^{-\kappa r}, \quad (3.87)$$

where κ is the screening wave-vector. This is known also as Yukawa potential.

4 Carbon allotropes

4.1 Introduction

Carbon with atomic number 6 is the second and fourth most abundant chemical element by mass in the universe and in the human body respectively. Its name originated from the Latin word *carbo* which means charcoal [59]. It can be found in every aspect of daily life such as, soot, wood, inks, paints, and so on. The discovery of some of its allotrope in the past century and at the turn of 21th century opened up a new horizons for developing new technology based on them. Due to their intriguing properties they are the most promising candidate for replacing the silicon technology. The electron configuration of carbon is $1s^2 2s^2 2p^2$. Carbon allotrope, are fullerene, carbon nanotubes, diamond, graphite, and graphene as seen in Fig. 4.1 [60]. Diamond, a bulky allotrope of carbon is the most popular gemstone in the world which is the hardness material. The atomic arrangement of carbon atoms in diamond is sp^3 which makes it a good thermal conductor [59]. The mother of all other allotropes is graphene a true 2D material that exist in the 3D world. Wrapping it up leads to Fullerene, a quasi-0D, rolling it yields a carbon nanotube (CNT), a quasi-1D, and stacking it gives rise to graphite. There are single and multilayer carbon nanotubes diameters with the order of few nanometers and length of microns even in some special cases millimeters. The arrangement of carbon atoms in nanotubes is sp^2 . It was discovered in 1992 by Sumio Iijima who worked at that moment at IBM [61]. Its high tensile strength, electrical and thermal conductivity and chemical stability drew attention to it at the end of last century. Before the discovery of nanotubes, fullerenes were made by Kroto et al. in 1985 where their existence was predicted in 1970. It consists of 60 carbon atoms and its diameter is about 1nm. Due to its geometry, fullerene's hardness is greater than that of diamond. Another allotrope of carbon, graphite which is the softest natural material consists of a few layers of graphene. The distance between these layers is about 0.335 nm and are held together by Van der Waals force. Some properties of carbon allotropes can be found in the table 4.1.

Table 4.1: Properties of carbon allotropes.

| Allotropes | Diamonds | Graphene | CNT | Fullerene |
|------------------------------|-----------|------------|---------------|---------------|
| Dimension | 3D | 2D | 1D | 0D |
| Hybridization | sp^3 | sp^2 | sp^2 | sp^2 |
| Bond length (\AA) | 1.54 | 1.42 | 1.42 | 1.42 |
| Density g/cm^3 | 3.5 | 2.6 | 1.2-2 | 1.72 |
| Electronic properties | insulator | semi-metal | semiconductor | semiconductor |

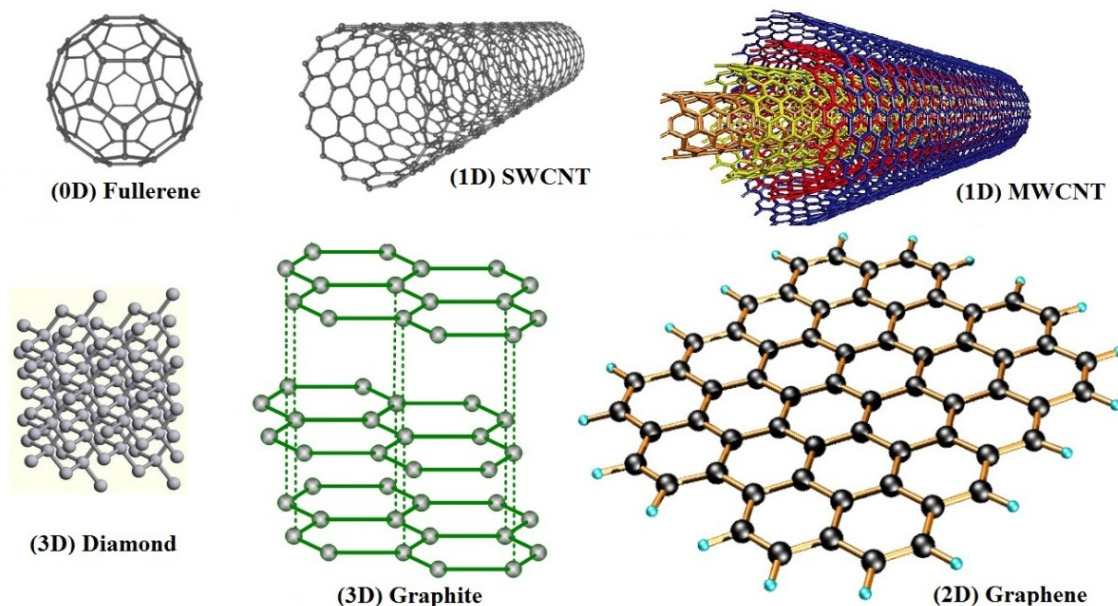


Figure 4.1: Carbon allotropes.

4.2 Graphene

Graphene, the building block of CNT, graphite, and fullerenes, is a single layer of carbon atoms that are arranged in a two-dimensional hexagonal honeycomb lattice where the distance between two carbon atoms is 0.142 nm. Graphene was discovered in 2004 by Andre Geim and Konstantin Novoselov [62]. Indeed, this hexagonal lattice is not a Bravais lattice but can be regarded as a Bravais lattice with two bases. In graphene every carbon atom shares one s orbital with two p orbitals and form three sp^2 orbitals with wave functions given by [63]

$$\begin{aligned}\Psi_1 &= \frac{1}{\sqrt{3}}\phi_{2s} + \sqrt{\frac{2}{3}}\phi_{2p_x}, \\ \Psi_2 &= \frac{1}{\sqrt{3}}\phi_{2s} - \frac{1}{\sqrt{6}}\phi_{2p_x} + \frac{1}{\sqrt{2}}\phi_{2p_y}, \\ \Psi_3 &= \frac{1}{\sqrt{3}}\phi_{2s} - \frac{1}{\sqrt{6}}\phi_{2p_x} - \frac{1}{\sqrt{2}}\phi_{2p_y}.\end{aligned}\tag{4.1}$$

These three wave functions are strongly binded together in the 2D planar layer. This makes graphene the hardest existing material . The fourth electron of carbon occupies the p_z orbital and makes π and anti- π bindings as shown in Fig. 4.2 (adopted from the Ref. [64].)

Some of the striking features of graphene are: *a)* it is the purest form of carbon: *b)* its Young modulus is extremely high which is on the order of 1 TPA: *c)* it has highest intrinsic mobility which is about $2 \times 10^5 \text{ cm}^2\text{V}^{-1}\text{s}^{-1}$: *d)* the thermal conductivity of graphene is about $5000 \text{ Wm}^{-1}\text{K}^{-1}$ which is exceptionally high: *e)* a suspended graphene can transmit 98 percent of light, and *f)* it has zero band-gap and so on. [62, 65, 66]. If graphene is confined to one direction it leads to a new 1D

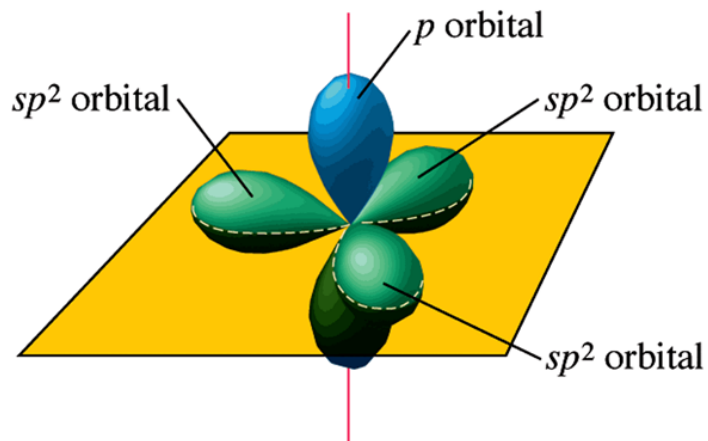
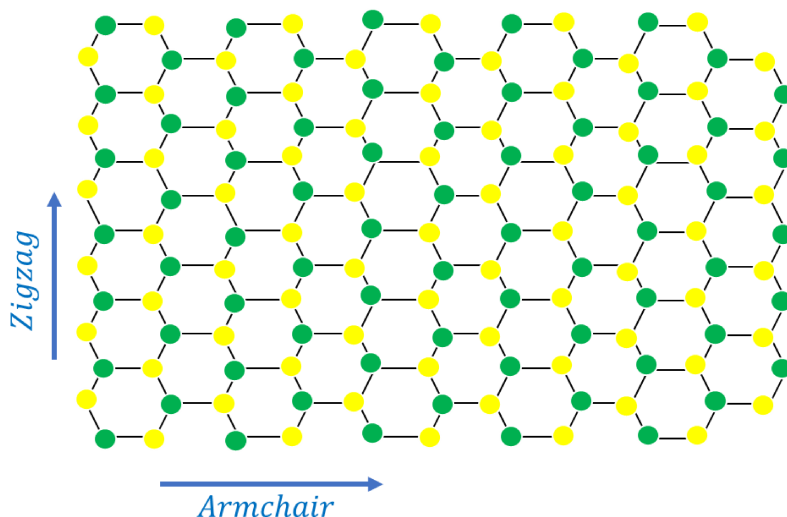
Figure 4.2: sp^2 configuration in graphene.

Figure 4.3: The crystal of arm-chair and zigzag graphene nanoribbons.

novel structure known as graphene nanoribbon. There are two kinds of nanoribbons; armchair and zigzag which are defined in terms of their edges as depicted in Fig. 4.3. To evaluate the electrical and optical properties of graphene and its nanoribbons we need to obtain their wave functions which is the subject of the following section.

4.3 The tight-binding model

To evaluate any quantity of a system, we need to solve the Schrodinger equation and obtain its eigenvalues and eigenfunctions. The total Hamiltonian of system is given by

$$H_{total} = \sum_i \frac{p_i^2}{2m} + \sum_i \frac{P_i^2}{2M} + V_{e-e} + V_{i-i} + V_{nucl}, \quad (4.2)$$

where the first and second terms indicate kinetic energy of electrons and nuclei respectively. V_{e-e} , V_{i-i} , and V_{nucl} are the electron-electron, nucleus-nucleus, and

electron-nucleus Coulomb potential energies respectively which are given by

$$\begin{aligned}
 V_{e-e} &= \frac{1}{2} \sum_{i \neq j} \frac{e^2}{|\vec{r}_i - \vec{r}_j|}, \\
 V_{i-i} &= \frac{1}{2} \sum_{I \neq J} \frac{e^2 z_I z_J}{|\vec{R}_I - \vec{R}_J|}, \\
 V_{nucl} &= - \sum_I \frac{e^2 z_I}{|\vec{r} - \vec{R}_I|}.
 \end{aligned} \tag{4.3}$$

To solve this many-body problem there are methods such as Hartree, Hartree-Fock, density functional theory, and Monte Carlo to name but a few. Every of these methods has its own limitation, for instance in the Hartree-Fock method we need to solve 10^{23} coupled equations for a simple system that contains only one electron for every atom, or the Monte Carlo method is valid only for a system with a small number of electrons. All these methods are numerical and can only predicate ground state energy and a few excited states as well. In the many-body methods that are mentioned what we obtain is only for one momentum. Now we can assume how much it is cumbersome to deal with this problem if we want to evaluate it for all points in the Brillouin zone (BZ). One of the simplest models is to regard only the one-electron Schrödinger equation. In this model, we assume some approximations such as the Rigid lattice approximation where the nuclei are considered to be fix at their equilibrium position. In addition, since the mass of the nucleus is much larger than that of an electron the kinetic energy of nucleus can be neglected. This simple model and picture leads to band theory in crystals. There are some methods based on this picture such as tight-binding (TB), orthogonalized plane wave (OPW), Pseudopotential, cellular, augmented plane wave (APW), Green's function, and Lanczos [44]. Note that except for the tight-binding method all the other methods are numerical and one needs to take care of the divergence. Even to obtain a reasonable solution one needs to consider more states. The tight-binding method was introduced by Bloch in 1928. The predicted results by it have some good agreement with the obtained experimental results.

In the tight-binding method the wave function of the crystal is constructed by a linear combination of atomic orbitals (LCAO) [67]. In other words,

$$\Psi_{crystal}(\vec{x}) = \sum_{i,j,l} c_{i,j,l} \phi_{i,j,l}^{orbital}(\vec{x}) \tag{4.4}$$

where l is the index of the orbital in the atom, j refers to the atomic base in the unit cell and i stands for the position of unit cell in the crystal. For graphene as shown in Fig. 4.4, the bases in the unit cell and primitive vectors of its crystal are given by

$$\vec{a}_1 = \frac{a_{cc}}{2}(3, \sqrt{3}), \quad \vec{a}_2 = \frac{a_{cc}}{2}(3, -\sqrt{3}), \tag{4.5}$$

$$\vec{\tau}_1 = a_{cc}(0, 0), \quad \vec{\tau}_2 = a_{cc}(1, 0), \tag{4.6}$$

where a_{cc} is the distance between two carbon atoms. The first Brillouin zone of graphene is also a honey comb as shown in Fig. 4.5 where its reciprocal primitive

vectors are

$$\vec{b}_1 = \frac{2\pi}{3a_{cc}}(1, \sqrt{3}), \quad \vec{b}_2 = \frac{2\pi}{3a_{cc}}(1, -\sqrt{3}). \quad (4.7)$$

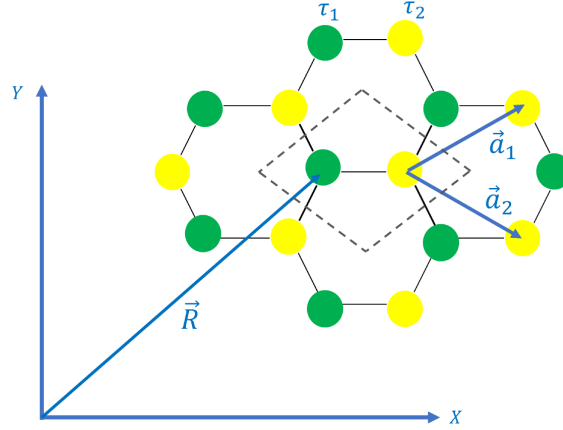


Figure 4.4: Graphene unit cell and its two primitive vectors a_1 and a_2 .

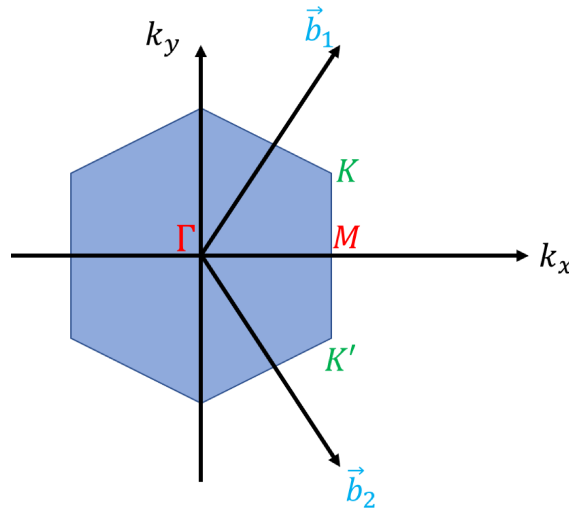


Figure 4.5: The First Brillouin zone of graphene lattice.

In addition, there are two important set of points K and K' in the first Brillouin zone which are defined by

$$K = \frac{2\pi}{3a_{cc}} \left(1, \frac{1}{\sqrt{3}} \right), \quad K' = \frac{2\pi}{3a_{cc}} \left(1, -\frac{1}{\sqrt{3}} \right). \quad (4.8)$$

One of the important features of these points is that we cannot move from one of these points to another by linear combination of the reciprocal primitive vectors.

It turns out from the ab-initio methods that all band structures of graphene for the energy range from -3 eV to 3 eV is due to the p_z orbital. Therefore, the crystal wave function of graphene in that range of energy can be written as

$$\Psi_{\vec{k}}(\vec{x}) = \sum_{\vec{R}} \sum_{\vec{\tau}_i=1}^2 c_{\vec{k}, \vec{R}, \vec{\tau}_i} \phi_{p_z}(\vec{x} - \vec{R} - \vec{\tau}_i), \quad (4.9)$$

where \vec{R} is

$$\vec{R} = n_1 \vec{a}_1 + n_2 \vec{a}_2, \quad n_1, n_2 \in \mathcal{Z}. \quad (4.10)$$

To determine the coefficients in Eq. (4.9), $c_{\vec{k}, \vec{R}}$, we can employ the Bloch condition for wave function which states

$$\Psi_{\vec{k}}(\vec{x} + \vec{R}) = e^{i\vec{k} \cdot \vec{R}} \Psi_{\vec{k}}(\vec{x}), \quad (4.11)$$

where $\Psi_{\vec{k}}(\vec{x} + \vec{R})$ is

$$\begin{aligned} \Psi_{\vec{k}}(\vec{x} + \vec{R}') &= \sum_{\vec{R}} \sum_{\vec{\tau}_i=1}^2 c_{\vec{k}, \vec{R} + \vec{R}', \vec{\tau}_i} \phi_{p_z}(\vec{x} + \vec{R}' - \vec{R} - \vec{\tau}_i) \\ &= \sum_{\vec{R}} \sum_{\vec{\tau}_i=1}^2 c_{\vec{k}, \vec{R} + \vec{R}', \vec{\tau}_i} \phi_{p_z}(\vec{x} - \vec{R} - \vec{\tau}_i). \end{aligned} \quad (4.12)$$

By some simple algebra and combing Eqs. (4.9), (4.11), and (4.12) we find

$$\Psi_{\vec{k}}(\vec{x}) = \frac{1}{\sqrt{N_{un}}} \frac{1}{\sqrt{1 + S(\vec{k})}} \sum_{\vec{R}} \sum_{\vec{\tau}_i=1}^2 c_{\vec{k}, \vec{\tau}_i} \phi_{p_z} e^{i\vec{k} \cdot \vec{R}} (\vec{x} - \vec{R} - \vec{\tau}_i), \quad (4.13)$$

where N_{un} is the number of unit cell and $S(\vec{k})$ is

$$S(\vec{k}) = \sum_{\vec{\delta} \neq 0} e^{i\vec{k} \cdot \vec{\delta}} S(\vec{\delta}), \quad (4.14)$$

with

$$S(\vec{\delta}) = \int d\vec{x} \phi_{p_z}(\vec{x}) \phi_{p_z}(\vec{x} - \vec{\delta}), \quad (4.15)$$

where $\vec{\delta}$ is the distance between two p_z orbitals. For the first nearest neighbor (FNN) approximation, $S(\vec{k}) \simeq 1$. Therefore, the wave function of graphene with the FNN approximation is

$$\Psi_{\vec{k}}(\vec{x}) \simeq \frac{1}{\sqrt{N_{un}}} \sum_{\vec{R}} \sum_{\vec{\tau}_i=1}^2 c_{\vec{k}, \vec{\tau}_i} e^{i\vec{k} \cdot \vec{R}} \phi_{p_z}(\vec{x} - \vec{R} - \vec{\tau}_i), \quad (4.16)$$

where its second quantization representation is

$$|\Psi_{\vec{k}}\rangle = \frac{1}{\sqrt{N_{un}}} \sum_{\vec{R}} \sum_{\vec{\tau}_i=1}^2 c_{\vec{k}, \vec{\tau}_i} e^{i\vec{k} \cdot \vec{R}} |\vec{R}, \vec{\tau}_i; \pi\rangle, \quad (4.17)$$

with $\langle \vec{x} | \vec{R}, \vec{\tau}_i; \pi \rangle \equiv \phi_{p_z}(\vec{x} - \vec{R} - \vec{\tau}_i)$.

A Wannier function can be expanded in terms of Bloch functions. Here, for this problem, the p_z orbital is the Wannier function. Therefore, it can be written as

$$|\vec{R}, \vec{\tau}_i; \pi\rangle = \frac{1}{\sqrt{N_{un}}} \sum_{\vec{k}} e^{-i\vec{k} \cdot \vec{R}} |\vec{k}, \vec{\tau}_i; \pi\rangle, \quad (4.18)$$

and the wave function in terms of Bloch bases becomes

$$|\Psi_{\vec{k}}\rangle = \sum_{\vec{\tau}_i=1}^2 c_{\vec{k},\vec{\tau}_i} |\vec{k}, \vec{\tau}_i; \pi\rangle. \quad (4.19)$$

Note that in second quantization representation a Wannier function can be expressed in terms of creation operator in the following manner

$$|\vec{R}, \vec{\tau}_i; \pi\rangle = \hat{c}^\dagger(\vec{R}, \vec{\tau}_i; \pi) |0\rangle, \quad (4.20)$$

where \hat{c}^\dagger is the creation operator. Therefore, Eq. (4.18) in second quantization representation becomes

$$\hat{c}^\dagger(\vec{R}, \vec{\tau}_i; \pi) = \frac{1}{\sqrt{N_{un}}} \sum_{\vec{k}} e^{-i\vec{k}\cdot\vec{R}} \hat{c}^\dagger(\vec{k}, \vec{\tau}_i; \pi). \quad (4.21)$$

To obtain the energy spectrum of graphene we need to solve the Schrodinger equation

$$H |\Psi_{\vec{k}}\rangle = E(\vec{k}) |\Psi_{\vec{k}}\rangle, \quad (4.22)$$

where the Hamiltonian operator consists of kinetic energy and energy of the periodic potential

$$\hat{H} = \hat{T} + \hat{U}. \quad (4.23)$$

In order to simplify notation, we drop π in the bases after this. Because $|\vec{R}, \vec{\tau}_i\rangle$ is a complete set of bases, in the sense that $\langle \vec{R}, \vec{\tau}_i | \vec{R}', \vec{\tau}_j \rangle = \delta_{\vec{R},\vec{R}'} \delta_{i,j}$ we can express the unitary operator, $\hat{1}$, in terms of these bases

$$\hat{1} = \sum_{\vec{R},\vec{\tau}_i} |\vec{R}, \vec{\tau}_i\rangle \langle \vec{R}, \vec{\tau}_i|. \quad (4.24)$$

Sandwiching the Hamiltonian operator between two unitary operators leads to

$$\hat{H} = \hat{1} \hat{H} \hat{1} = \sum_{\vec{R},\vec{\tau}_i} \sum_{\vec{R}',\vec{\tau}_j} |\vec{R}, \vec{\tau}_i\rangle \langle \vec{R}, \vec{\tau}_i | \hat{H} | \vec{R}', \vec{\tau}_j \rangle \langle \vec{R}', \vec{\tau}_j |, \quad (4.25)$$

where by some algebra and employing the Eq.(4.20) it can be written as

$$\hat{H} = \sum_{\vec{R},\vec{R}'} \sum_{\vec{\tau}_i,\vec{\tau}_j} t_{\vec{\tau}_i,\vec{\tau}_j}^{\vec{R},\vec{R}'} \hat{c}^\dagger(\vec{R}, \vec{\tau}_i) \hat{c}(\vec{R}', \vec{\tau}_j), \quad (4.26)$$

with $t_{\vec{\tau}_i,\vec{\tau}_j}^{\vec{R},\vec{R}'} = \langle \vec{R}, \vec{\tau}_i | \hat{H} | \vec{R}', \vec{\tau}_j \rangle$, where in the real space representation it is

$$t_{\vec{\tau}_i,\vec{\tau}_j}^{\vec{R},\vec{R}'} = \int d\vec{x} \phi_{p_z}^*(\vec{x} - \vec{R} - \vec{\tau}_i) \left[-\frac{\hbar^2}{2m} \vec{\nabla}^2 + \sum_{\vec{R}} U_{ion}(\vec{x} - \vec{x}_{\vec{R}}) \right] \phi_{p_z}(\vec{x} - \vec{R}' - \vec{\tau}_j). \quad (4.27)$$

Eq. (4.26) for FNN gives rise to

$$\hat{H} = \varepsilon_0 \sum_{\vec{R},\vec{\tau}_i=1}^2 \hat{c}^\dagger(\vec{R}, \vec{\tau}_i) \hat{c}(\vec{R}, \vec{\tau}_i) +$$

$$t_0 \sum_{\vec{R}, i=0}^2 \left[\hat{c}^\dagger(\vec{R}, \vec{\tau}_1) \hat{c}(\vec{R} + \vec{a}_i, \vec{\tau}_2) + \hat{c}^\dagger(\vec{R} + \vec{a}_i, \vec{\tau}_2) \hat{c}(\vec{R}, \vec{\tau}_1) \right], \quad (4.28)$$

with $\vec{a}_0 = 0$. The ε_0 and t_0 are on-site and hopping energies, respectively. Physically, on-site energy means the amount of energy that is needed to remove one electron from its site. Similarly, hopping energy means the necessary amount of energy to move an electron from one site to another site.

By using Eq. (4.18) we can write the Hamiltonian, Eq. (4.28), in momentum space

$$\begin{aligned} \hat{H} = \varepsilon_0 \sum_{\vec{k}, \vec{\tau}_i=1}^2 \hat{c}^\dagger(\vec{k}, \vec{\tau}_i) \hat{c}(\vec{k}, \vec{\tau}_i) + \\ t_0 \sum_{\vec{k}} \left[\lambda(\vec{k}) \hat{c}^\dagger(\vec{k}, \vec{\tau}_1) \hat{c}(\vec{k}, \vec{\tau}_2) + \lambda^*(\vec{k}) \hat{c}^\dagger(\vec{k}, \vec{\tau}_2) \hat{c}(\vec{k}, \vec{\tau}_1) \right], \end{aligned} \quad (4.29)$$

where $\lambda(\vec{k})$ is

$$\lambda(\vec{k}) = 1 + e^{i\vec{k} \cdot \vec{a}_1} + e^{i\vec{k} \cdot \vec{a}_2}. \quad (4.30)$$

By multiplying $\langle \vec{k}, \vec{\tau}_i |$ on both sides of Eq. (4.22) we arrive at

$$\langle \vec{k}, \vec{\tau}_i | \hat{H} | \Psi_{\vec{k}} \rangle = E(\vec{k}) \langle \vec{k}, \vec{\tau}_i | \Psi_{\vec{k}} \rangle. \quad (4.31)$$

By some algebra we find

$$\begin{bmatrix} \varepsilon_0 - E(\vec{k}) & t_0 \lambda(\vec{k}) \\ t_0 \lambda^*(\vec{k}) & \varepsilon_0 - E(\vec{k}) \end{bmatrix} \begin{bmatrix} c_{\vec{k}, \vec{\tau}_1} \\ c_{\vec{k}, \vec{\tau}_2} \end{bmatrix} = \begin{bmatrix} 0 \\ 0 \end{bmatrix}, \quad (4.32)$$

which has a solution if the determinant of the 2×2 matrix vanishes. This leads to

$$E_\zeta(\vec{k}) = \varepsilon_0 + \zeta t_0 |\lambda(\vec{k})|, \quad \zeta = \pm 1, \quad (4.33)$$

where $\zeta = +1, -1$ refers to conduction and valence bands. Using Eq. (4.30), we obtain for Eq. (4.33)

$$E_\zeta(\vec{k}) = \varepsilon_0 + \zeta t_0 \sqrt{1 + 4 \cos\left(\frac{\sqrt{3}}{2} k_y a_{cc}\right) \cos\left(\frac{3}{2} k_x a_{cc}\right) + 4 \cos^2\left(\frac{\sqrt{3}}{2} k_y a_{cc}\right)}, \quad (4.34)$$

with $t_0 \sim 2.7$ eV [68]. This value has been evaluated by density functional theory calculations. The energy dispersion of graphene in momentum space is shown in Fig. 4.6. By normalization condition of the wave function, $\langle \Psi_{\vec{k}} | \Psi_{\vec{k}} \rangle = 1$, the coefficients of Eq. (4.19) can be determined. From Eq. (4.32) we have

$$\left(\varepsilon_0 - E(\vec{k}) \right) c_{\vec{k}, \vec{\tau}_1} + t_0 \lambda(\vec{k}) c_{\vec{k}, \vec{\tau}_2} = 0, \quad (4.35)$$

where we replace $E(\vec{k})$ in (4.35) with Eq. (4.33) it becomes

$$c_{\vec{k}, \vec{\tau}_2} = \frac{|\lambda(\vec{k})|}{\lambda(\vec{k})} c_{\vec{k}, \vec{\tau}_1}. \quad (4.36)$$

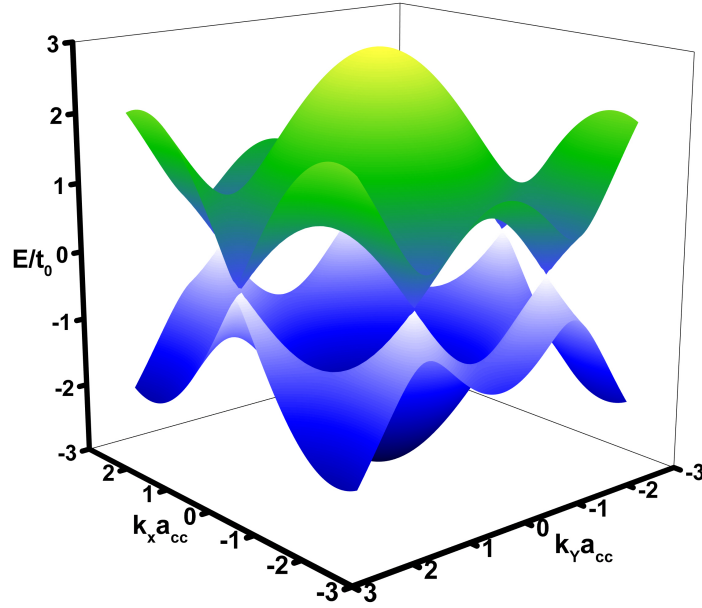


Figure 4.6: The energy spectrum of graphene.

Or in a more compact form

$$c_{\vec{k}, \vec{\tau}_2} = \zeta e^{-i\theta(\vec{k})} c_{\vec{k}, \vec{\tau}_1}, \quad (4.37)$$

where $\theta(\vec{k})$ is defined by

$$e^{-i\theta(\vec{k})} = \frac{|\lambda(\vec{k})|}{\lambda(\vec{k})}, \quad \theta(\vec{k}) = \tan^{-1} \left(\frac{\Re(\lambda(\vec{k}))}{\Im(\lambda(\vec{k}))} \right). \quad (4.38)$$

The normalization condition of the wave function results in

$$c_{\vec{k}, \vec{\tau}_1} = \frac{1}{\sqrt{2}}. \quad (4.39)$$

Therefore, the wave function of graphene becomes

$$|\Psi_{\vec{k}, \zeta}\rangle = \frac{1}{\sqrt{2}} \left(|\vec{k}, \vec{\tau}_1\rangle + \zeta e^{-i\theta(\vec{k})} |\vec{k}, \vec{\tau}_2\rangle \right). \quad (4.40)$$

In Fig. 4.7(a) the contour plot of Fig. 4.6 is shown. At the six corners of the first Brillouin zone the energy vanishes. At these points we can observe that the energy spectrum is like a cone as shown in Fig. 4.7(b). This suggests that the energy spectrum could be linear in those ranges. To investigate this we can expand the Hamiltonian matrix element of Eq. (4.32) about these points. For K , λ becomes

$$\lambda(\vec{q}) = \lambda(\vec{q})|_{\vec{q}=0} + (\vec{q} \cdot \vec{\nabla}_{\vec{k}}) \lambda(\vec{q})|_{\vec{q}=0} = \frac{3t_0 a_{cc}}{2} (q_x + iq_y), \quad \vec{q} = \vec{k} - \vec{K}. \quad (4.41)$$

We can replace $3t_0 a_{cc}/2$ by $\hbar v_F$. This yields

$$\lambda(\vec{q}) = \hbar v_F (q_x + iq_y), \quad (4.42)$$

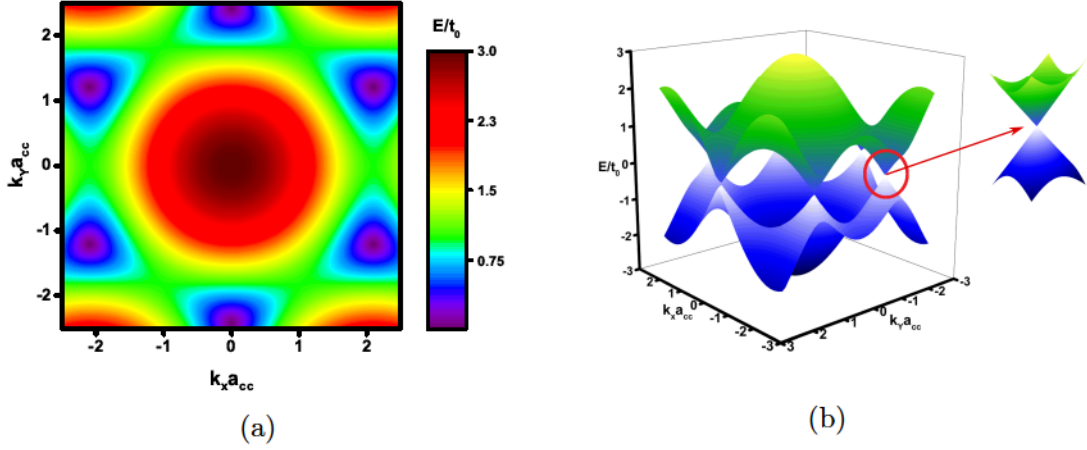


Figure 4.7: (a) Contour plot of energy spectrum in the Brillouin zone. (b) Graphene spectrum at one of the corner of Brillouin zone which is like a cone..

with $v_F \cong 10^6 m/s$. Therefore, the Hamiltonian for point K

$$H_K = \hbar v_F \begin{bmatrix} 0 & q_x + iq_y \\ q_x - iq_y & 0 \end{bmatrix}. \quad (4.43)$$

In the same manner, for K' we find

$$H_{K'} = \hbar v_F \begin{bmatrix} 0 & q_x - iq_y \\ q_x + iq_y & 0 \end{bmatrix}. \quad (4.44)$$

Eigenvalue and eigenfunction of Eqs. (4.43) and (4.44) are

$$E_\zeta(\vec{q}) = \zeta \hbar v_F |\vec{q}|, \quad (4.45)$$

$$\Psi_{\eta,\zeta}(\vec{r}) = \frac{1}{\sqrt{2}} \begin{bmatrix} e^{-i\eta\theta(\vec{q})} \\ \zeta \end{bmatrix} e^{i\vec{q}\cdot\vec{r}}, \quad \eta = \pm 1 \quad (4.46)$$

where $\eta = +1, -1$ indicates K and K' , respectively. This is known as the *k-p method* [45]. It is worth to pointing out that the effective Hamiltonian in Eqs. (4.43) and (4.44) are like the massless *Dirac equation* [68].

4.4 Density of States

One of the important concepts in the treatment of a quantum system is the energy density of states (DOS). Physically, DOS implies the available states between E and $E + dE$ where E indicates the energy. The definition of DOS is given by [67]

$$Dos(\varepsilon) = \sum_i \delta(\varepsilon - E_i) \quad (4.47)$$

where i denotes all quantum number and δ is the Dirac delta function. There are some general representations to express DOS e.g. [69]

$$\delta(\varepsilon - E_i) = \lim_{\nu \rightarrow 0} \frac{1}{\sqrt{2\pi\nu}} e^{-(\varepsilon - E_i)^2 / 2\nu^2}. \quad (4.48)$$

However, we employ the Green's function representation [70]. The definition of Green's function employed to solve an inhomogeneous equation is

$$(z - \hat{H}) \hat{G}(z) = \hat{1}, \quad (4.49)$$

with

$$z = \varepsilon + i\nu. \quad (4.50)$$

\hat{G} , \hat{H} , and $\hat{1}$ are Green's function, Hamiltonian, and unitary operator, respectively. From Eq. (4.49) we can rewrite the Green's function as

$$\hat{G}(z) = \frac{\hat{1}}{z - \hat{H}} = \frac{1}{z - \hat{H}} \sum_{\vec{k}, \zeta} |\vec{k}, \zeta\rangle \langle \vec{k}, \zeta|, \quad (4.51)$$

where we express the unitary operator in terms of the Bloch bases. By using Eq. (4.49), the matrix elements of the Green's function is given by

$$G^{\zeta'\zeta''}(\vec{k}', \vec{k}'', z) = \langle \vec{k}', \zeta' | \hat{G}(z) | \vec{k}'', \zeta'' \rangle = \lim_{\nu \rightarrow 0^+} \frac{\delta_{\vec{k}'\vec{k}''} \delta_{\zeta'\zeta''}}{\varepsilon + i\nu - E_{\zeta''}(\vec{k}'')}. \quad (4.52)$$

The Kronecker delta in Eq. (4.52) implies that only the diagonal terms of Green's function matrix exist. Then we can write

$$G^s(\vec{k}, \varepsilon) = P \frac{1}{\varepsilon - E_s(\vec{k})} - i\pi\delta(\varepsilon - E_s(\vec{k})), \quad (4.53)$$

where P means the principal value. We can see that the imaginary part of the Green's function and the Dirac delta function are related by

$$\Im G^s(\vec{k}, \varepsilon) = -\pi\delta(\varepsilon - E_s(\vec{k})). \quad (4.54)$$

Therefore, the DOS in terms of the Green's function for graphene is

$$Dos(\varepsilon) = \sum_{\vec{k}, \zeta} \delta(\varepsilon - E_{\zeta}(\vec{k})) = -\frac{2}{\pi} \sum_{\vec{k} \in FBZ} \Im G^{\zeta}(\vec{k}, \varepsilon). \quad (4.55)$$

After some algebra we arrive at

$$Dos(\varepsilon) = -\frac{A}{2\pi^3} \lim_{\nu \rightarrow 0^+} \int_{\vec{k} \in FBZ} d\vec{k} \frac{\nu}{(\varepsilon - E(\vec{k}))^2 + \nu^2}, \quad (4.56)$$

where A and FBZ refer to the area and the first Brillouin zone. In Fig. 4.8, DOS for a typical range of energy is shown. As seen, for $|\varepsilon|$ in the vicinity of 1 eV, DOS has its maximum value. This is expected since the dominating color is green.

4.5 Lindhard polarization function of graphene

The building block quantity to determine transport and optical properties of a system is its polarization function which in the simplest approximation, in the absence of Coulomb potential interaction and exchange effects, is known as Lindhard polarization function see Eq. (3.31). For an electron doped graphene as shown in Fig

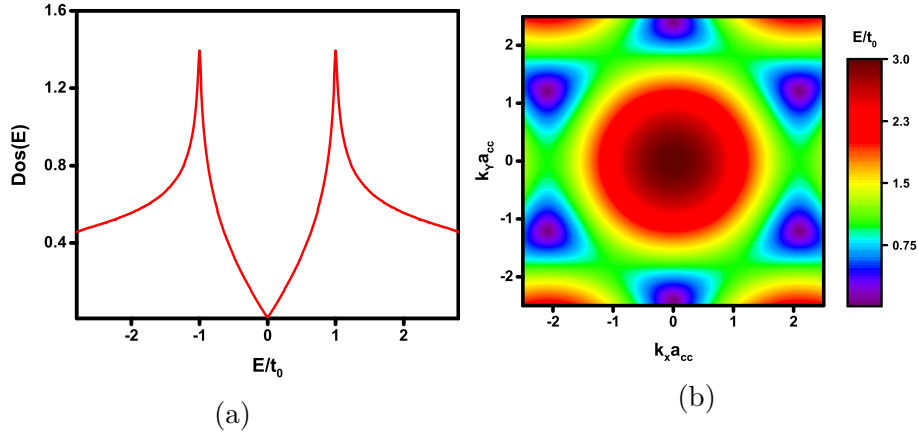


Figure 4.8: DOS of graphene (a) and (b) contour plot of its energy spectrum.

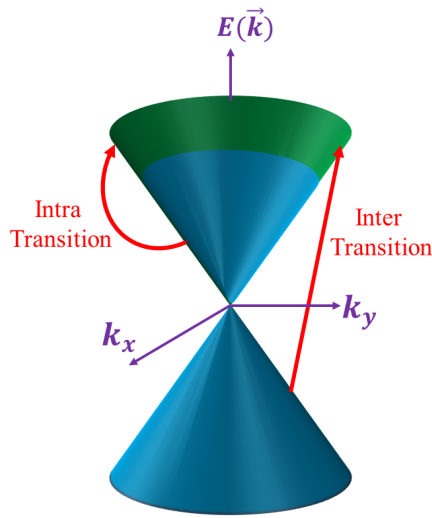


Figure 4.9: Intra- and inter-transitions in the energy spectrum of graphene.

4.9 , the Lindhard polarization function in long wavelength limit for single-band transition known also as intra-transition is given by,

$$\chi^0(q \rightarrow 0, \omega) = \frac{q^2 E_F}{\pi \hbar^2 \omega^2}, \quad (4.57)$$

and for two-band transition, inter-transition, it is,

$$\chi^0(q \rightarrow 0, \omega) = \frac{q^2}{2\pi \hbar \omega} \left[\frac{2E_F}{\hbar \omega} + \frac{1}{2} \left| \frac{2E_F - \hbar \omega}{2E_F + \hbar \omega} \right| - i \frac{\pi}{2} \Theta(\hbar \omega - 2E_F) \right]. \quad (4.58)$$

The evaluation of the Lindhard polarization function for doped graphene with all details for all wavelength can be found at Refs. [71, 72].

5 Armchair Graphene Nanoribbons

5.1 Tight-binding model for AGNRs

In the previous chapter, as an example of a novel quantum well structure we dealt with graphene. To extend our treatment to quantum wires, we consider armchair graphene nanoribbons (AGNRs). Indeed, AGNRs can be constructed from graphene by confining it in one direction and extending it in the other. To evaluate the band structure of AGNRs using the tight-binding model, we need to determine a suitable unit cell. This is depicted in Fig. 5.1, where dm refers to the dimer number. Moreover, the primitive vector is $a_T = 2a_{cc}$.

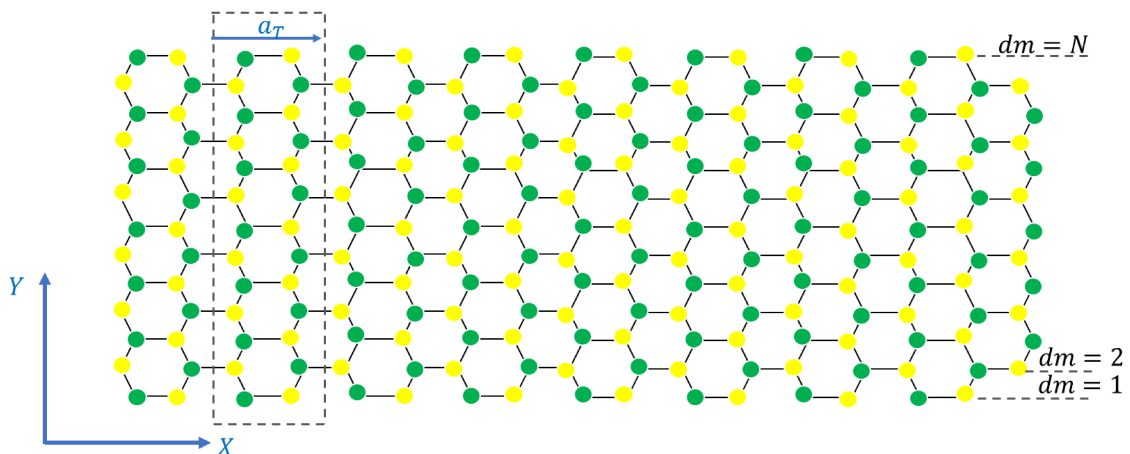


Figure 5.1: The unit cell and primitive vector of an AGNR.

As in graphene we need to employ unitary operators to evaluate the band structure. From Fig. 5.1, given by

$$\hat{1} = \sum_i \sum_{m=1}^N \sum_{j=1}^2 |\vec{i}, m, \vec{j}, \pi\rangle \langle \vec{i}, m, \vec{j}, \pi|, \quad (5.1)$$

where i , m , and j indicate the indices of the unit cell vector, dimer number and basis in a dimer, respectively. Note that in real-space representation we have

$$\langle \vec{x} | \vec{i}, m, \vec{j} \rangle = \phi_{2p_z}(\vec{x} - \hat{e}_x \cdot \vec{i} - \hat{e}_x \cdot \vec{j} - \hat{e}_x \frac{\sqrt{3}}{2} m). \quad (5.2)$$

In order to simplify notation, we drop the vector signs. The $|i, m, j\rangle$ makes a complete set of bases, that is

$$\langle i, m, j | i', m', j' \rangle = \delta_{ii'} \delta_{mm'} \delta_{jj'}. \quad (5.3)$$

Therefore, we can write the second quantization Hamiltonian of the AGNR as

$$\hat{H} = \sum_{ii'} \sum_{jj'} \sum_{mm'} t_{i,m,j}^{i',m',j'} \hat{c}^\dagger(i', m', j') \hat{c}(i, m, j), \quad (5.4)$$

where the hopping parameter is defined by

$$t_{i,m,j}^{i',m',j'} = \langle i, m, j | \hat{H} | i', m', j' \rangle. \quad (5.5)$$

For FNN Eq. (5.4) becomes

$$\begin{aligned} \hat{H} &= \varepsilon_0 \sum_i \sum_m \hat{c}^\dagger(i, m, \tau_1) \hat{c}(i, m, \tau_1) + \hat{c}^\dagger(i, m, \tau_2) \hat{c}(i, m, \tau_2) \\ &\quad - t_0 \sum_i \sum_{m \in \text{odd}} \hat{c}^\dagger(i, m, \tau_1) \hat{c}(i-1, m, \tau_2) - t_0 \sum_i \sum_{m \in \text{even}} \hat{c}^\dagger(i, m, \tau_1) \hat{c}(i, m, \tau_2) \\ &\quad - t_0 \sum_i \sum_m \hat{c}^\dagger(i, m, \tau_1) \hat{c}(i, m+1, \tau_2) + \hat{c}^\dagger(i, m, \tau_1) \hat{c}(i, m-1, \tau_2) + h.c \end{aligned} \quad (5.6)$$

where $h.c$ indicates hermitian conjugate. The relation between the Wannier function and the Bloch basis for an AGNR leads to

$$\langle \vec{x} | i, m, j \rangle = \frac{1}{\sqrt{N_{un}}} \sum_k e^{ikR_i} \langle \vec{x} | k, m, j \rangle, \quad (5.7)$$

which provides us with the connection between operators in these two bases in second quantization representation

$$\hat{c}^\dagger(i, m, j) = \frac{1}{\sqrt{N_{un}}} \sum_k e^{ikR_i} \hat{c}^\dagger(k, m, j), \quad (5.8)$$

where N_{un} stands for the unit cell number. Using Eq. (5.8), we can write the Hamiltonian in momentum space

$$\begin{aligned} \hat{H} &= -t_0 \sum_k \sum_{m \in \text{even}} \hat{c}^\dagger(k, m, \tau_1) \hat{c}(k, m, \tau_2) + \hat{c}^\dagger(k, m, \tau_2) \hat{c}(k, m, \tau_1) \\ &\quad - t_0 \sum_k \sum_{m \in \text{odd}} \hat{c}^\dagger(k, m, \tau_1) \hat{c}(k, m, \tau_2) e^{-ika\tau} + \hat{c}^\dagger(k, m, \tau_2) \hat{c}(k, m, \tau_1) e^{ika\tau} \\ &\quad - t_0 \sum_k \sum_m \hat{c}^\dagger(k, m, \tau_1) \hat{c}(k, m+1, \tau_2) + \hat{c}^\dagger(k, m, \tau_1) \hat{c}(k, m-1, \tau_2) \\ &\quad - t_0 \sum_k \sum_m \hat{c}^\dagger(k, m, \tau_2) \hat{c}(k, m+1, \tau_1) + \hat{c}^\dagger(k, m, \tau_2) \hat{c}(k, m-1, \tau_1). \end{aligned} \quad (5.9)$$

Furthermore, the wave function of the AGNR crystal within the tight-binding approximation for the FNN is

$$\Psi_k(\vec{x}) = \frac{1}{\sqrt{N_{un}}} \sum_i \sum_{m=1}^N \sum_{j=1}^2 C_{\tau_j}(k, m) e^{ikR_i} \phi_{2p_z}(\vec{x} - \vec{i} - \vec{j}(m)), \quad (5.10)$$

in terms of the Bloch basis (using Eq. (5.7))

$$|\Psi_k\rangle = \sum_{m=1}^N \sum_{j=1}^2 C_{\tau_j}(k, m) |k, m, j\rangle. \quad (5.11)$$

To evaluate the eigenvalues and eigenfunctions, it is required to solve the Schroedinger equation

$$\hat{H} |\Psi\rangle = E |\Psi\rangle.$$

Applying Eqs. (5.9) and (5.10) we obtain a set of equations

$$-t_0 \left\{ \underbrace{C_{\tau_2}(k, m)}_{m \in \text{even}} + \underbrace{C_{\tau_2}(k, m)}_{m \in \text{odd}} e^{-ika_T} + C_{\tau_2}(k, m+1) + C_{\tau_2}(k, m-1) \right\} = E(k) C_{\tau_1}(k, m), \quad (5.12)$$

$$-t_0 \left\{ \underbrace{C_{\tau_1}(k, m)}_{m \in \text{even}} + \underbrace{C_{\tau_1}(k, m)}_{m \in \text{odd}} e^{ika_T} + C_{\tau_1}(k, m+1) + C_{\tau_1}(k, m-1) \right\} = E(k) C_{\tau_2}(k, m). \quad (5.13)$$

In order to solve these equations, we assume that $C_{\tau_1}(k, m)$ and $C_{\tau_2}(k, m)$ have the following generic forms

$$C_{\tau_1}(k, m) = A \exp\left(i \frac{\sqrt{3}}{2} m k_y a_{cc}\right) + B \exp\left(-i \frac{\sqrt{3}}{2} m k_y a_{cc}\right), \quad (5.14)$$

$$C_{\tau_2}(k, m) = C \exp\left(i \frac{\sqrt{3}}{2} m k_y a_{cc}\right) + D \exp\left(-i \frac{\sqrt{3}}{2} m k_y a_{cc}\right), \quad (5.15)$$

where A , B , C , and D are arbitrary coefficients. Beyond the width boundaries of the AGNR there are no electrons. This implies that the crystal wave function vanishes there. This imposes that for $m = 0$

$$C_{\tau_1}(k, 0) = 0, \quad (5.16)$$

$$C_{\tau_2}(k, 0) = 0, \quad (5.17)$$

and for $m = N + 1$

$$C_{\tau_1}(k, N + 1) = 0, \quad (5.18)$$

$$C_{\tau_2}(k, N + 1) = 0. \quad (5.19)$$

From Eqs. (5.16) and (5.17), we arrive at the following relations between coefficients

$$B = -A, \quad D = -C. \quad (5.20)$$

By combining Eqs. (5.18) and (5.20), we obtain

$$C_{\tau_1}(k, N+1) = A \sin\left(\frac{\sqrt{3}}{2}(N+1)k_y a_{cc}\right) = 0, \quad (5.21)$$

where the coefficient A cannot vanish, otherwise the wave function vanishes everywhere. This indicates

$$\frac{\sqrt{3}}{2}(N+1)k_y a_{cc} = \pi r \Rightarrow k_y = \frac{\pi r}{(N+1)\sqrt{3}a_{cc}}, \quad 1 \leq r \leq N, \quad (5.22)$$

where r is an integer. In order to simplify the following calculations, we use this new variable

$$k_y(r) = \frac{\sqrt{3}}{2}a_{cc}k_y. \quad (5.23)$$

Therefore, The generic solutions become

$$C_{\tau_1}(k, m) = A [e^{imk_y(r)} - e^{-imk_y(r)}], \quad (5.24)$$

$$C_{\tau_2}(k, m) = C [e^{imk_y(r)} - e^{-imk_y(r)}]. \quad (5.25)$$

The set of equations, Eqs. (5.12) and (5.13) for $m = 0$ result in

$$-t_0 \underbrace{\{C_{\tau_2}(k, 1) + C_{\tau_2}(k, 1)\}}_{m \in \text{even}} e^{-ika_T} + \underbrace{C_{\tau_2}(k, 0) + C_{\tau_2}(k, 2)}_{m \in \text{odd}} = E(k)C_{\tau_1}(k, 1), \quad (5.26)$$

and

$$-t_0 \underbrace{\{C_{\tau_1}(k, 1) + C_{\tau_1}(k, 1)\}}_{m \in \text{even}} e^{ika_T} + C_{\tau_1}(k, 2) + \underbrace{C_{\tau_1}(k, 0)}_{=0} = E(k)C_{\tau_2}(k, 1), \quad (5.27)$$

where, after simplifying, they become

$$-t_0 \{C_{\tau_2}(k, 1)e^{-ika_T} + C_{\tau_2}(k, 2)\} = E(k)C_{\tau_1}(k, 1), \quad (5.28)$$

$$-t_0 \{C_{\tau_1}(k, 1)e^{ika_T} + C_{\tau_1}(k, 2)\} = E(k)C_{\tau_2}(k, 1). \quad (5.29)$$

From Eqs. (5.24), (5.25), (5.28), and (5.29) we find the following set of equations

$$-t_0 C \{e^{ika_T} + 2 \cos(k_y(r))\} = AE(k), \quad (5.30)$$

$$-t_0 A \{e^{-ika_T} + 2 \cos(k_y(r))\} = CE(k), \quad (5.31)$$

which can be expressed as

$$\begin{bmatrix} E(k) & t_0 (e^{-ika_T} + 2 \cos(k_y(r))) \\ t_0 (e^{ika_T} + 2 \cos(k_y(r))) & E(k) \end{bmatrix} \begin{bmatrix} A \\ C \end{bmatrix} = \begin{bmatrix} 0 \\ 0 \end{bmatrix}. \quad (5.32)$$

This implies that there is a solution if the matrix determinant vanishes, which gives rise to

$$E_{r,\eta}(k) = \eta t_0 \sqrt{1 + 2\lambda(r) \cos(ka_T) + \lambda^2(r)}, \quad \eta = \pm 1, \quad (5.33)$$

with

$$\lambda(r) = 2 \cos(k_y(r)). \quad (5.34)$$

Here $\eta = +1, -1$ refers to the conduction and valence bands, respectively.

The arbitrary coefficients A and C in the Eq. (5.32) can be determined by the normalization condition of the wave function, which for an AGNR is

$$\langle \Psi_{k,r} | \Psi_{k,r} \rangle = \sum_{m=1}^N |C_{\tau_1}(k, m)|^2 + |C_{\tau_2}(k, m)|^2 = 1. \quad (5.35)$$

Because the energy spectrum is a function of momentum, band index and the parameter η , it can be concluded that the coefficients of the wave function have the same dependencies. In other words, Eqs. (5.24) and (5.25) become

$$C_{\tau_1}(k, m) = A_{k,r,\eta} \sin(mk_y(r)), \quad (5.36)$$

$$C_{\tau_2}(k, m) = C_{k,r,\eta} \sin(mk_y(r)). \quad (5.37)$$

From Eq. (5.30), we have

$$E_{r,\eta}(k) A_{k,r,\eta} + t_0 (e^{-ika_T} + 2 \cos(k_y(r))) C_{k,r,\eta} = 0, \quad (5.38)$$

which yields

$$C_{k,r,\eta} = -\frac{E_{r,\eta}(k) A_{k,r,\eta}}{t_0 (e^{-ika_T} + 2 \cos(k_y(r)))}, \quad \Rightarrow |C_{k,r,\eta}|^2 = |A_{k,r,\eta}|^2. \quad (5.39)$$

Combing Eqs. (5.35) and (5.39) leads to

$$\sum_{m=1}^N 2|A_{k,r,\eta}|^2 \sin^2(mk_y(r)) = 1. \quad (5.40)$$

Since $A_{k,r,\eta}$ is independent of sum index it factors out of the sum and we have to evaluate the sine squared term, which is

$$\begin{aligned} \sum_{m=1}^N \sin^2(mk_y(r)) &= \frac{N}{2} - \frac{1}{4} \left[\frac{\sin(2(N+1)k_y(r))}{\sin(k_y(r))} \right] \\ &= \frac{1}{2} \left[N - \frac{\sin(2(N+1)k_y(r))}{2 \sin(k_y(r))} \right]. \end{aligned} \quad (5.41)$$

Finally, we obtain the coefficients $A_{k,r,\eta}$

$$A_{k,r,\eta} = \pm \left[N - \frac{\sin(2(N+1)k_y(r))}{2 \sin(k_y(r))} \right]^{-1/2}. \quad (5.42)$$

From Eq. (5.39), after some algebra we arrive at

$$C_{k,r,\eta} = -\eta e^{i\theta(k,r)} A_{k,r,\eta}, \quad (5.43)$$

with

$$\theta(k, r) = \tan^{-1} \left[\frac{\sin(ka_T)}{2 \cos(k_y(r)) + \cos(ka_T)} \right]. \quad (5.44)$$

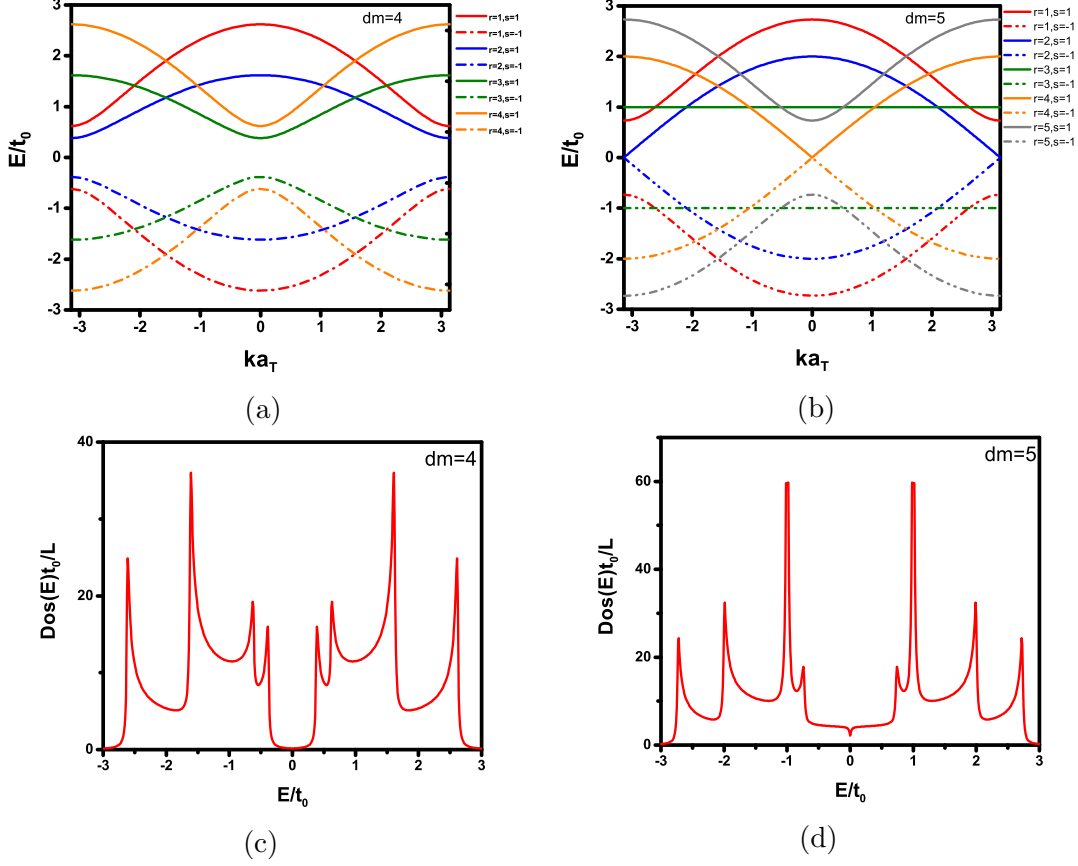


Figure 5.2: Energy spectrum of AGNR for (a) $dm = 4$ (b) $dm = 5$ and their DOS.

5.2 DOS of AGNRs

Similar to the DOS for graphene, for the AGNR we find

$$Dos(\varepsilon) = \sum_{\eta, r=1}^N \sum_k \delta(\varepsilon - E_{r,\eta}(k)) = -\frac{2}{\pi} \sum_{\eta, r=1}^N \sum_{k \in FBZ} \Im m G^{\eta, r}(k, \varepsilon), \quad (5.45)$$

which, after some algebra becomes

$$Dos(\varepsilon) = -\frac{L}{\pi^2} \lim_{\nu \rightarrow 0^+} \sum_{\eta, r=1}^N \int_{k \in FBZ} dk \frac{\nu}{(\varepsilon - E_{r,\eta}(k))^2 + \nu^2}, \quad (5.46)$$

where L indicates the length of the AGNR.

In Figs. 5.2 (a) and (b) the energy spectrum of an AGNR with width $dm = 4$ and $dm = 5$ are shown along with their DOS in Figs. 5.2 (c) and (d), respectively. The number of peaks in the DOS spectrum, is equal to indices number of band

indices. Note that, according to the DOS spectrum we can determine whether a system is metal, semiconductor, or insulator. For a metallic system the DOS is gapless. However, for a semiconductor or insulator in some range of energies it has a gap. It is worth pointing out that the gap in an insulator is much larger than that of a semiconductor. Therefore, we can state that AGNRs with $dm = 4$ and $dm = 5$ are semiconducting and metallic systems, respectively. In order to find a connection between the width of an AGNR and whether it is metallic or not, in Fig. 5.3 we have shown DOS spectrum for some typical widths. It can be observed that for $dm = 3z + 2$ where z is an integer, the AGNR is metallic. It is worth pointing out that by increasing the dimer number, we expect to obtain the same results as graphene. As seen in Fig. 5.3 (f) for $dm = 100$, the DOS behavior is similar to Fig. 4.8. In addition, the energy spectrum of an AGNR for $dm = 101$ is shown in Fig. 5.4 (a) which corresponds to the cross section of the energy spectrum of graphene, Fig. 5.4 (b).

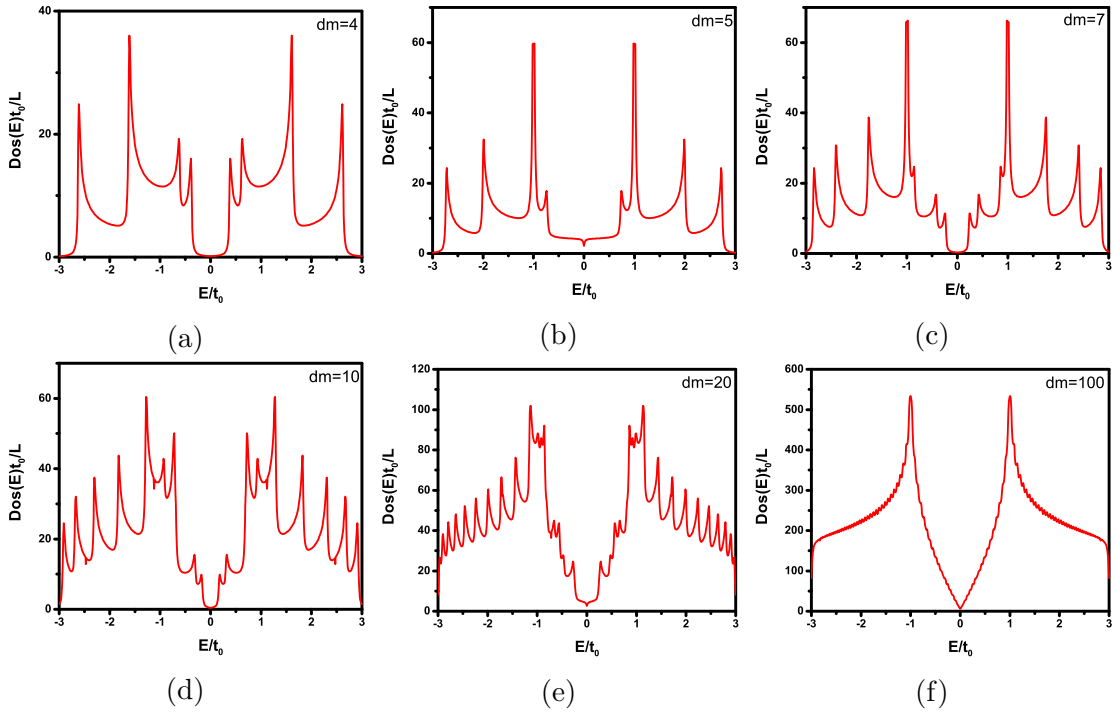


Figure 5.3: DOS spectrum for (a) $dm = 4$, (b) $dm = 5$, (c) $dm = 7$, (d) $dm = 10$, (e) $dm = 20$, and (f) $dm = 100$.

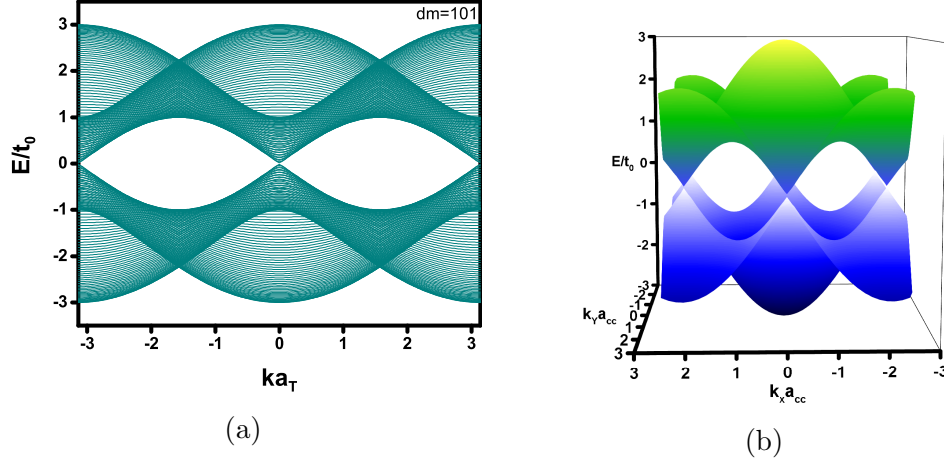


Figure 5.4: (a) Energy spectrum of AGNR for dimer number $dm = 101$ (b) graphene energy spectrum.

5.3 The $k \cdot p$ method for AGNRs

For a metallic AGNR, there is a sub-band with linear dispersion. To determine the value of this sub-band it is sufficient to set $k = 0$ in Eq. (5.33). This leads to

$$\lambda(r) = -1. \quad (5.47)$$

By employing Eqs. (5.23) and (5.34), we obtain the sub-band index

$$r = \frac{2}{3}(dm + 1). \quad (5.48)$$

As an example, for $dm = 5$ (as shown in Fig. 5.2 (b)), the desired linear sub-band index is $r = 4$. Since the dispersion is linear, for this sub-band, as in the case of graphene in the low energy limit, we can employ the $k \cdot p$ method to evaluate its eigenvalues and eigenfunctions. In this case, the Dirac points are

$$\vec{K} = (0, K), \quad \vec{K}' = (0, -K), \quad (5.49)$$

with $K = 4\pi/3a_{cc}\sqrt{3}$. In contrast to graphene, these points are degenerate in momentum space due to the fact that AGNR is a 1D system. The $k \cdot p$ Hamiltonian, using the same approach that we applied to graphene, is

$$H_{k,p} = H_K \otimes I_{K'} + I_K \otimes H_{K'}, \quad (5.50)$$

which is a 4×4 matrix

$$H_{k,p} = v_F \begin{bmatrix} 0 & p_y - ip_x & 0 & 0 \\ p_y + ip_x & 0 & 0 & 0 \\ 0 & 0 & 0 & p_y + ip_x \\ 0 & 0 & p_y - ip_x & 0 \end{bmatrix}. \quad (5.51)$$

The Schroedinger equation in the $k \cdot p$ method is

$$H_{k,p}\mathcal{U}(\vec{x}) = E\mathcal{U}(\vec{x}), \quad (5.52)$$

which leads to two sets of block diagonal Hamiltonians pertaining to K and K'

$$H_K \begin{pmatrix} \varphi_A(y) \\ \varphi_B(y) \end{pmatrix} e^{ikx} = E \begin{pmatrix} \varphi_A(y) \\ \varphi_B(y) \end{pmatrix} e^{ikx}, \quad (5.53)$$

$$H_{K'} \begin{pmatrix} \varphi'_A(y) \\ \varphi'_B(y) \end{pmatrix} e^{ikx} = E \begin{pmatrix} \varphi'_A(y) \\ \varphi'_B(y) \end{pmatrix} e^{ikx}. \quad (5.54)$$

Therefore, the Bloch wave function is

$$\mathcal{U}(\vec{x}) = \begin{pmatrix} \varphi_A(y) \\ \varphi_B(y) \\ \varphi'_A(y) \\ \varphi'_B(y) \end{pmatrix} e^{ikx} = \begin{pmatrix} \mathcal{U}_{\tau_1}^K(\vec{x}) \\ \mathcal{U}_{\tau_2}^K(\vec{x}) \\ \mathcal{U}'_{\tau_1}(\vec{x}) \\ \mathcal{U}'_{\tau_2}(\vec{x}) \end{pmatrix} \equiv \begin{pmatrix} \mathcal{U}_{\tau_1}(\vec{x}) \\ \mathcal{U}_{\tau_2}(\vec{x}) \\ \mathcal{U}'_{\tau_1}(\vec{x}) \\ \mathcal{U}'_{\tau_2}(\vec{x}) \end{pmatrix}. \quad (5.55)$$

The total wave function can be regarded as that of two bases at τ_1 and τ_2 where each of them has two terms pertaining to the two Dirac points. In other words,

$$\Psi_{\tau_1}(\vec{x}) = \mathcal{U}_{\tau_1}(\vec{x}) e^{i\vec{K}\cdot\vec{x}} + \mathcal{U}'_{\tau_1}(\vec{x}) e^{i\vec{K}'\cdot\vec{x}} = \varphi_A(y) e^{i\vec{K}\cdot\vec{x}+ikx} + \varphi'_A(y) e^{i\vec{K}'\cdot\vec{x}+ikx}, \quad (5.56)$$

$$\Psi_{\tau_2}(\vec{x}) = \mathcal{U}_{\tau_2}(\vec{x}) e^{i\vec{K}\cdot\vec{x}} + \mathcal{U}'_{\tau_2}(\vec{x}) e^{i\vec{K}'\cdot\vec{x}} = \varphi_B(y) e^{i\vec{K}\cdot\vec{x}+ikx} + \varphi'_B(y) e^{i\vec{K}'\cdot\vec{x}+ikx}. \quad (5.57)$$

The wave function vanishes at the edge of AGNR, that is

$$\Psi_{\tau_1}(\vec{x})|_{y=0} = \varphi_A(0) e^{ikx} + \varphi'_A(0) e^{ikx} = 0, \quad (5.58)$$

$$\Psi_{\tau_1}(\vec{x})|_{y=W} = \varphi_A(W) e^{iKW+ikx} + \varphi'_A(W) e^{-iKW+ikx} = 0, \quad (5.59)$$

$$\Psi_{\tau_2}(\vec{x})|_{y=0} = \varphi_B(0) e^{ikx} + \varphi'_B(0) e^{ikx} = 0, \quad (5.60)$$

$$\Psi_{\tau_2}(\vec{x})|_{y=W} = \varphi_B(W) e^{iKW+ikx} + \varphi'_B(W) e^{-iKW+ikx} = 0, \quad (5.61)$$

with W being the width of ribbon. We obtain the following relation at $y = 0$

$$\varphi_A(0) + \varphi'_A(0) = 0, \quad (5.62)$$

$$\varphi_B(0) + \varphi'_B(0) = 0, \quad (5.63)$$

and at $y = W$

$$\varphi_A(W) e^{iKW} + \varphi'_A(W) e^{-iKW} = 0, \quad (5.64)$$

$$\varphi_B(W) e^{iKW} + \varphi'_B(W) e^{-iKW} = 0. \quad (5.65)$$

In order to determine φ_A and φ_B , we solve Eq. (5.53) in real space

$$v_F \begin{pmatrix} 0 & p_y - ip_x \\ p_y + ip_x & 0 \end{pmatrix} \begin{pmatrix} \varphi_A(y) \\ \varphi_B(y) \end{pmatrix} e^{ikx} = E \begin{pmatrix} \varphi_A(y) \\ \varphi_B(y) \end{pmatrix} e^{ikx}, \quad (5.66)$$

with $p_x = -i\hbar\partial_x$ and $p_y = -i\hbar\partial_y$. After some algebra we arrive at

$$\hbar v_F (-i\partial_y - ik) \varphi_B(y) = E \varphi_A(y), \quad (5.67)$$

$$\hbar v_F (-i\partial_y + ik) \varphi_A(y) = E \varphi_B(y). \quad (5.68)$$

Applying $(-\partial_y + ik)$ to both sides of Eq. (5.67), we find

$$(\hbar v_F)^2 (-\partial_y^2 + k^2) \varphi_B(y) = E^2 \varphi_B(y). \quad (5.69)$$

Employing the same approach for K' yields

$$(\hbar v_F)^2 (-\partial_y^2 + k^2) \varphi'_B(y) = E^2 \varphi'_B(y). \quad (5.70)$$

The generic solutions for Eqs. (5.69) and (5.70) have the following form

$$\varphi_B(y) = Ae^{ik_y y} + Be^{-ik_y y}, \quad (5.71)$$

$$\varphi'_B(y) = Ce^{ik_y y} + De^{-ik_y y}, \quad (5.72)$$

where A , B , C , and D are arbitrary coefficients. From Eqs. (5.63), (5.65), (5.71), and (5.72), we find

$$A + B + C + D = 0, \quad (5.73)$$

$$Ae^{i(K+k_y)W} + De^{-i(K+k_y)W} + Be^{-i(k_y-K)W} + Ce^{i(k_y-K)W} = 0. \quad (5.74)$$

One of the possible choices to satisfy the above conditions is

$$B = C = 0, \quad A = -D. \quad (5.75)$$

Applying it to Eq. (5.74) results in

$$\sin((K + k_y)W) = 0 \Rightarrow k_y(n) = \frac{n\pi}{W} - \frac{4\pi}{3a_{cc}\sqrt{3}}. \quad (5.76)$$

Therefore, φ_B and φ'_B become

$$\varphi_B(y) = Ae^{ik_y(n)y}, \quad (5.77)$$

$$\varphi'_B(y) = -Ae^{ik_y(n)y}. \quad (5.78)$$

Combing them with Eqs. (5.69) and (5.70) results in

$$E = \eta \hbar v_F \sqrt{k_y^2(n) + k^2}, \quad \eta = \pm 1, \quad (5.79)$$

where $\eta = +1, -1$ stands for the conduction and valence bands. Using the normalization condition for the wave function we can determine the coefficient A to be

$$\int_0^W dy \varphi_B^*(y) \varphi_B(y) = 1, \quad A = \frac{1}{\sqrt{W}}. \quad (5.80)$$

From Eq. (5.67), we can determine $\varphi_A(y)$

$$\varphi_A(y) = \frac{\eta e^{ik_y(n)y}}{\sqrt{W}} e^{-i\theta(k, k_y(n))}, \quad (5.81)$$

with

$$\theta(k, k_y(n)) = \tan^{-1} \left(\frac{k}{k_y(n)} \right). \quad (5.82)$$

Therefore, the wave function of AGNR within the k·p method is

$$\mathcal{U}(x, y) = \mathcal{U}_{k, k_y(n), \eta}(x, y) = \frac{1}{\sqrt{4LW}} \begin{pmatrix} \left(\begin{matrix} \eta e^{-i\theta(k, k_y(n))} \\ 1 \end{matrix} \right) e^{ik_y(n)y} \\ \left(\begin{matrix} -\eta e^{-i\theta(k, k_y(n))} \\ 1 \end{matrix} \right) e^{-ik_y(n)y} \end{pmatrix} e^{ikx}. \quad (5.83)$$

5.4 Lindhard polarization function of AGNR

In contrast to graphene, we have derived the Lindhard polarization function of AGNR with detailed calculations for intra-band transition as shown in Fig. 5.5.

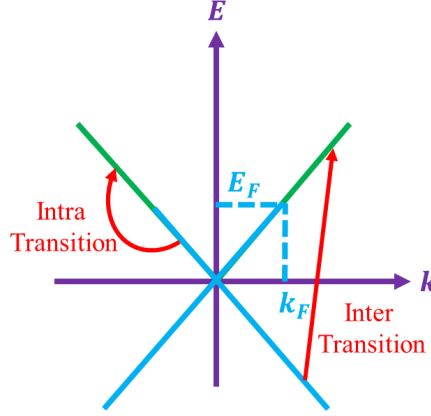


Figure 5.5: Intra- and inter-transitions in the energy spectrum of AGNR.

Employing Eqs. (5.83), (5.79), and (3.31) and after some algebra, for the real part of the Lindhard polarization function of AGNR in momentum space, we obtain

$$\Re \chi_{nn'}^0(q, \omega) = \frac{L}{2\pi} \frac{1}{4W} (I + II), \quad (5.84)$$

with

$$I = \int dk \frac{(1 + \eta\eta' \cos \alpha_{nn'}(k, k+q) f(E_n^\eta(k)))}{E_n^\eta(k) - E_{n'}^{\eta'}(k+q) + \hbar\omega}, \quad (5.85)$$

$$II = \int dk \frac{(1 + \eta\eta' \cos \alpha_{nn'}(k-q, k) f(E_n^{\eta'}(k)))}{E_{n'}^{\eta'}(k) - E_n^\eta(k-q) - \hbar\omega}, \quad (5.86)$$

where the form factor, $\alpha_{nn'}$, is

$$\alpha_{nn'}(k, k') = \theta(k, k_y(n)) - \theta(k', k_y(n')). \quad (5.87)$$

Since we limit our calculations to the single band of an electron doped AGNR, we have $n = n'$ and $\eta = \eta' = +$. In this case, since $k_y(n)$ vanishes for the metallic AGNR the energy spectrum becomes

$$E_n^+(k) = \gamma|k|, \quad \gamma \equiv \hbar v_F. \quad (5.88)$$

The form factor determines the nonvanishing range of the integral. For $|q| < |k_F|$, this interval must be $[-k_F, -q] \cup [0, k_F]$ and for $|q| > |k_F|$, $[0, k_F]$. Therefore, inserting Eq. (5.88) into Eq. (5.85) we arrive at

$$I = \int dk \frac{f(E_n^\eta(k))}{\gamma|k| - \gamma\sqrt{k^2 + q^2} + 2kq \cos \phi + \hbar\omega},$$

with $\cos \phi = \pm 1$ since we are dealing with a one-dimensional integral. Next, integrating over ϕ gives

$$I = \int dk \frac{f(E_n^\eta(k))}{\gamma|k| - \gamma|k+q| + \hbar\omega} + \int dk \frac{f(E_n^\eta(k))}{\gamma|k| - \gamma|k-q| + \hbar\omega}. \quad (5.89)$$

To make it clear, we assign the subscript 1 to the integrals for $|q| < |k_F|$ and the subscript 2 for $|q| > |k_F|$. Eq. (5.89) for $|q| < |k_F|$ becomes

$$\begin{aligned}
 I_1 = & \int_{-k_F}^{-q} dk \underbrace{\frac{f(E_n^+(k))}{\gamma|k| - \gamma|k+q| + \hbar\omega}}_{M_1} + \int_0^{k_F} dk \underbrace{\frac{f(E_n^+(k))}{\gamma|k| - \gamma|k-q| + \hbar\omega}}_{M_2} \\
 & + \int_{-k_F}^{-q} dk \underbrace{\frac{f(E_n^+(k))}{\gamma|k| - \gamma|k-q| + \hbar\omega}}_{M_3} + \int_0^{k_F} dk \underbrace{\frac{f(E_n^+(k))}{\gamma|k| - \gamma|k+q| + \hbar\omega}}_{M_4}, \quad (5.90)
 \end{aligned}$$

and for $|q| > |k_F|$ it becomes

$$I_2 = \int_0^{k_F} dk \underbrace{\frac{f(E_n^+(k))}{\gamma|k| - \gamma|k+q| + \hbar\omega}}_{M_5} + \int_0^{k_F} dk \underbrace{\frac{f(E_n^+(k))}{\gamma|k| - \gamma|k-q| + \hbar\omega}}_{M_6}. \quad (5.91)$$

The modulus terms in Eqs. (5.90) and (5.91) are determined by examining the intervals of integrals. The moduli M_1 through M_6 are

$$M_1 \Rightarrow -k_F < k < -q \Rightarrow |k+q| = -(k+q),$$

$$M_2 \Rightarrow 0 < k < k_F \Rightarrow \begin{cases} 0 < k < q & \Rightarrow |k-q| = -(k-q), \\ q < k < k_F & \Rightarrow |k-q| = (k-q), \end{cases}$$

$$M_3 \Rightarrow -k_F < k < -q \Rightarrow |k-q| = -(k-q),$$

$$M_4 \Rightarrow 0 < k < k_F \Rightarrow |k+q| = (k+q),$$

$$M_5 \Rightarrow 0 < k < k_F \Rightarrow |k+q| = (k+q),$$

$$M_6 \Rightarrow 0 < k < k_F \Rightarrow |k-q| = -(k-q).$$

After some algebra, Eqs. (5.90) and (5.91) become

$$\begin{aligned}
 \gamma I_1 = & \int_{-k_F}^{-q} dk \frac{f(E_n^+(k))}{-k + (k+q) + \omega'} + \int_0^q dk \frac{f(E_n^+(k))}{k + (k-q) + \omega'} \\
 & + \int_q^{k_F} dk \frac{f(E_n^+(k))}{k - (k-q) + \omega'} + \int_{-k_F}^{-q} dk \frac{f(E_n^+(k))}{-k + (k-q) + \omega'} \\
 & + \int_0^{k_F} dk \frac{f(E_n^+(k))}{k - (k+q) + \omega'}, \\
 \gamma I_2 = & \int_0^{k_F} dk \frac{f(E_n^+(k))}{k - (k+q) + \omega'} + \int_0^{k_F} dk \frac{f(E_n^+(k))}{k + (k-q) + \omega'},
 \end{aligned}$$

with $\omega' \equiv \hbar\omega/\gamma$. The Fermi-Dirac distribution function

$$f(E_n^+(k)) = \frac{1}{1 + e^{\beta(\gamma|k| - \mu)}}, \quad (5.92)$$

at zero temperature becomes $f(E_n^+(k)) = 1$. Evaluating the integrals in Eqs. (5.90) and (5.91) result in

$$\gamma I_1 = \frac{2(k_F - q)}{\omega' + q} + \frac{2k_F - q}{\omega' - q} + \frac{1}{2} \ln \left(\frac{\omega' + q}{\omega' - q} \right), \quad (5.93)$$

$$\gamma I_2 = \frac{k_F}{\omega' - q} + \frac{1}{2} \ln \left(\frac{2k_F - q + \omega'}{\omega' - q} \right). \quad (5.94)$$

The non-vanishing intervals of integration in case *II* for $|q| < |k_F|$ is $[-k_F, 0] \cup [q, k_F]$ and for $|q| > |k_F|$ is $[-k_F, 0]$. Similar to the evaluation of *I*, we find

$$\begin{aligned} \gamma II_1 = & \int_{-k_F}^0 dk \underbrace{\frac{f(E_n^+(k))}{|k| - |k - q| - \omega'}}_{M_1} + \int_{-k_F}^0 dk \underbrace{\frac{f(E_n^+(k))}{|k| - |k + q| - \omega'}}_{M_2} \\ & + \int_q^{k_F} dk \underbrace{\frac{f(E_n^+(k))}{|k| - |k - q| - \omega'}}_{M_3} + \int_q^{k_F} dk \underbrace{\frac{f(E_n^+(k))}{|k| - |k + q| - \omega'}}_{M_4}. \end{aligned} \quad (5.95)$$

$$\gamma II_2 = \int_{-k_F}^0 dk \underbrace{\frac{f(E_n^+(k))}{|k| - |k - q| - \omega'}}_{M_5} + \int_{-k_F}^0 dk \underbrace{\frac{f(E_n^+(k))}{|k| - |k + q| - \omega'}}_{M_6}. \quad (5.96)$$

The modulus terms in M_1 to M_6 are

$$M_1 \Rightarrow -k_F < k < 0 \Rightarrow |k - q| = -(k - q),$$

$$M_2 \Rightarrow -k_F < k < 0 \Rightarrow \begin{cases} -k_F < k < -q \Rightarrow |k + q| = -(k + q), \\ -q < k < 0 \Rightarrow |k + q| = (k + q), \end{cases}$$

$$M_3 \Rightarrow q < k < k_F \Rightarrow |k - q| = (k - q),$$

$$M_4 \Rightarrow q < k < k_F \Rightarrow |k + q| = (k + q),$$

$$M_5 \Rightarrow -k_F < k < 0 \Rightarrow |k - q| = -(k - q),$$

$$M_6 \Rightarrow -k_F < k < 0 \Rightarrow |k + q| = (k + q).$$

which gives rise to

$$\begin{aligned} \gamma II_1 = & \int_{-k_F}^0 dk \frac{f(E_n^+(k))}{-k + (k - q) - \omega'} + \int_{-k_F}^{-q} dk \frac{f(E_n^+(k))}{-k + (k + q) - \omega'} \\ & + \int_{-q}^0 dk \frac{f(E_n^+(k))}{-k - (k + q) - \omega'} + \int_q^{k_F} dk \frac{f(E_n^+(k))}{k - (k - q) - \omega'} \\ & + \int_q^{k_F} dk \frac{f(E_n^+(k))}{k - (k + q) - \omega'}. \end{aligned} \quad (5.97)$$

$$\gamma II_2 = \int_{-k_F}^0 dk \frac{f(E_n^+(k))}{-k + (k - q) - \omega'} + \int_{-k_F}^0 dk \frac{f(E_n^+(k))}{-k - (k + q) - \omega'}. \quad (5.98)$$

Evaluating the integrals in Eqs. (5.97) and (5.98) result in

$$\gamma II_1 = \frac{q - 2k_F}{\omega' + q} + \frac{2(k_F - q)}{q - \omega'} - \frac{1}{2} \ln \left(\frac{\omega' + q}{\omega' - q} \right), \quad (5.99)$$

$$\gamma II_2 = \frac{-k_F}{\omega' + q} - \frac{1}{2} \ln \left(\frac{\omega' + q}{-2k_F + q + \omega'} \right). \quad (5.100)$$

Finally, by combing Eqs. (5.93), (5.94), (5.99), and (5.100) and considering the spin effect, for $|q| < |k_F|$ we find

$$\frac{1}{L} \Re \chi_{++}^0(q, \omega) = \frac{1}{W} \frac{1}{\gamma \pi} \left(\frac{q^2}{\omega'^2 - q^2} \right), \quad (5.101)$$

and for $|q| > |k_F|$

$$\frac{1}{L} \Re \chi_{++}^0(q, \omega) = \frac{1}{W} \frac{1}{\gamma \pi} \left(\frac{qk_F}{\omega'^2 - q^2} + \frac{1}{4} \ln \left[\frac{\omega'^2 - (2k_F - q)^2}{\omega'^2 - q^2} \right] \right). \quad (5.102)$$

The imaginary part of the Lindhard polarization function can be evaluated similar to the real part

$$I' = -\pi \int dk [1 + \eta \eta' \cos \alpha_{nn'}(k, k+q) f(E_n^\eta(k))] \delta(E_n^\eta(k) - E_{n'}^{\eta'}(k+q) + \hbar\omega), \quad (5.103)$$

$$II' = \pi \int dk [1 + \eta \eta' \cos \alpha_{nn'}(k-q, k) f(E_n^{\eta'}(k))] \delta(E_n^{\eta'}(k) - E_n^\eta(k-q) - \hbar\omega). \quad (5.104)$$

Following the preceding derivation

$$\begin{aligned} -\gamma I'/\pi &= \int_{-k_F}^{-q} \delta(q + \omega') dk + \int_0^q \delta(2k - q + \omega') dk + \int_q^{k_F} \delta(q + \omega') dk \\ &+ \int_{-k_F}^{-q} \delta(-q + \omega') dk + \int_0^{k_F} \delta(-q + \omega') dk + \int_0^{k_F} \delta(-q + \omega') dk \\ &+ \int_0^{k_F} \delta(2k - q + \omega') dk, \end{aligned} \quad (5.105)$$

$$\begin{aligned} \gamma II'/\pi &= \int_{-k_F}^0 \delta(-q - \omega') dk + \int_{-k_F}^{-q} \delta(q - \omega') dk + \int_{-q}^0 \delta(-2k - q - \omega') dk \\ &+ \int_q^{k_F} \delta(q - \omega') + \int_q^{k_F} \delta(-q - \omega') dk + \int_{-k_F}^0 \delta(-q - \omega') dk \\ &+ \int_{-k_F}^0 \delta(-2k - q - \omega') dk, \end{aligned} \quad (5.106)$$

which results in

$$-\gamma I'/\pi = \theta(q - \omega') [\theta(q + \omega') + \theta(2k_F - q + \omega')], \quad (5.107)$$

$$\gamma II'/\pi = \theta(q + \omega') [\theta(q - \omega') + \theta(2k_F - q - \omega')]. \quad (5.108)$$

Finally, the imaginary part of Lindhard polarization function of AGNR for intra-band transition is given by

$$\begin{aligned} \frac{1}{L} \Im \chi_{++}^0(q, \omega) &= \frac{1}{2\gamma W} [\theta(q + \omega') \theta(2k_F - q - \omega') \\ &- \theta(q - \omega') \theta(2k_F - q + \omega')]. \end{aligned} \quad (5.109)$$

6 Transport and optical properties of AGNRs

6.1 Introduction

As an application of QLRT, below we evaluate the optical properties and surface plasmons of an AGNR. We consider an AGNR on a substrate as shown in Fig. 6.1.

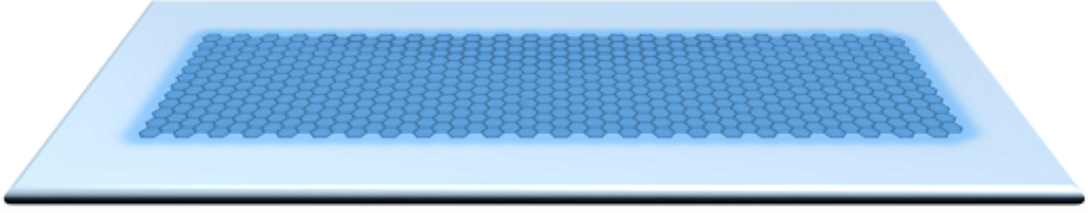


Figure 6.1: An AGNR on a substrate.

To evaluate the properties of AGNR in interacting with a TM field we use the conventions that are depicted in Fig. 6.2. Satisfying the boundary condition for normal components of the electric field

$$\epsilon_1 E_1^\perp - \epsilon_2 E_2^\perp = \rho_s, \quad (6.1)$$

where ρ_s is surface charge density, leads to

$$\epsilon_1 (E_I \cos \theta_I + E_R \cos \theta_R) - \epsilon_1 E_T \cos \theta_T = \rho_s, \quad (6.2)$$

where E_I , E_R , and E_T are the amplitudes of incident, reflected, and transmitted electric field of electromagnetic wave respectively. The θ_I , θ_R , and θ_T stand for the angles of incidence, reflection, and transmission respectively. For the tangential components of electric field

$$E_1^\parallel - E_2^\parallel = 0, \quad (6.3)$$

which at the boundary between two media results in

$$(E_I \sin \theta_I - E_R \sin \theta_R) - E_T \sin \theta_T = 0. \quad (6.4)$$

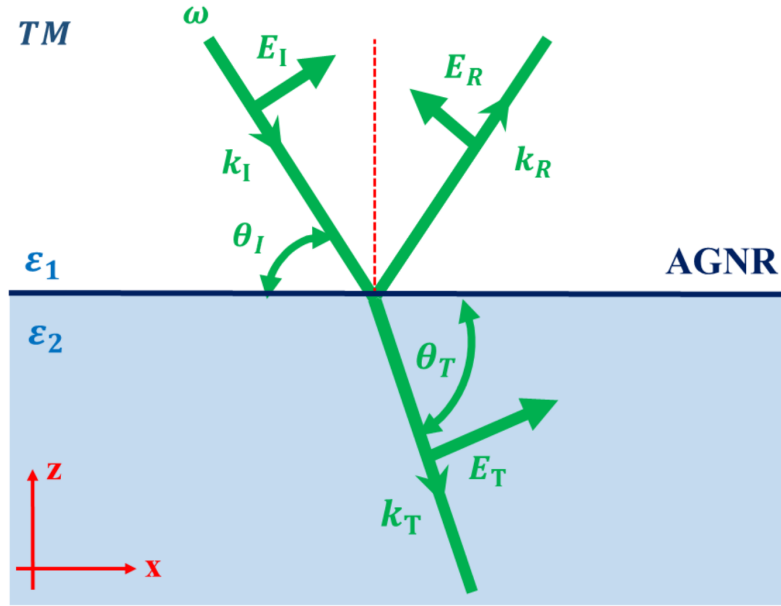


Figure 6.2: An AGNR at the interface of two media with permittivities ϵ_1 and ϵ_2 .

To find a relation between the charge density and the electric field we can exploit the current density continuity equation which by Fourier transforming of it we obtain

$$-\omega\rho_s(q, \omega) + k_x J_x(q, \omega) = 0, \quad (6.5)$$

where according to Fig. 6.2 for the tangential component of wave vector we have, $k_x = k_T \cos \theta_T$. Setting

$$J_x(q, \omega) = \sigma(q, \omega) E_x(q, \omega), \quad (6.6)$$

and noticing $E_x(q, \omega) = E_T(q, \omega) \sin \theta_T$ yields

$$\rho_s(q, \omega) = \frac{\sigma(q, \omega)}{\omega} k_T E_T \sin \theta_T \cos \theta_T. \quad (6.7)$$

We now use Snell's law $n_1 \cos \theta_I = n_2 \cos \theta_T$, $\theta_I = \theta_R$, and write $E_R = r E_I$, $E_T = t E_I$ where r and t are reflection and transmission coefficients respectively. Furthermore, we have $\epsilon_1/\epsilon_2 = n_1^2/n_2^2$, $k_T = n_2 \omega/c$, and $\epsilon_i/\epsilon_0 = n_i^2$, $i = 1, 2$. Then Eqs. (6.2) and (6.4) become

$$(1 + r) \cos \theta_I = \frac{t}{\epsilon_1} \cos \theta_T \left(\epsilon_2 + \frac{\sigma(q, \omega)}{\omega} k_T \sin \theta_T \right), \quad (6.8)$$

$$(1 - r) \sin \theta_I = t \sin \theta_T. \quad (6.9)$$

Solving Eqs. (6.8) and (6.9) for r and t gives rise to

$$t(k, \omega) = 2 \left[\frac{n_2}{n_1} + \frac{\sin \theta_T}{\sin \theta_I} + \frac{\sin \theta_T}{n_1 \varepsilon_0 c} \sigma(k, \omega) \right]^{-1}, \quad (6.10)$$

$$r(k, \omega) = 1 - \frac{\sin \theta_T}{\sin \theta_I} t(k, \omega). \quad (6.11)$$

For our purpose to express conductivity in terms of polarization function we can write the surface charge density ρ_s in Eq. (6.2) as

$$\begin{aligned} \rho_s(\vec{x}, t) &= \sum_{i=1}^N \int \int \rho(x, y, z, t) \delta(y - y_i) \delta(z) dy dz \\ &= N \rho(x, t), \end{aligned} \quad (6.12)$$

where by combining with Eq. (3.45),

$$\rho(q, \omega) = e^2 \chi(q, \omega) \phi_{ext}(q, \omega),$$

and Eq. (6.5) we find

$$\sigma(q, \omega) = \frac{iN e^2 \omega}{q^2} \chi(q, \omega). \quad (6.13)$$

The Lindhard polarization function for AGNR for intra-band transition, $q \leq k_F$ has only the real part, see Eq.(5.101), which is given by

$$\chi^0 = \Re \chi_{++}^0(q, \omega) = \frac{L}{W} \frac{1}{\hbar \pi} \left(\frac{v_F q^2}{\omega^2 - v_F^2 q^2} \right). \quad (6.14)$$

RPA, Eq. (3.54), takes into account Coulomb interaction which polarization function within is given by

$$\chi^{RPA}(q, \omega) = \frac{\chi^0(q, \omega)}{1 - V(q) \chi^0(q, \omega)},$$

here $V(q)$ is the Fourier transform of the matrix element of the 2D screened Coulomb potential, with respect to x , $V(x, y) = e^{-k_s r} / r$, $r^2 = x^2 + y^2$,

$$V(q) = \frac{2e^2}{\epsilon_0} \int_0^1 \int_0^1 K_0[\delta_\lambda |(y - y')|] dy dy', \quad (6.15)$$

where $\delta_\lambda = W(k_s^2 + q^2)^{1/2} = W k_F (\lambda^2 + k_s'^2)^{1/2}$, $\lambda = q/k_F$, $k_s' = k_s/k_F$, and K_0 is the zeroth order modified Bessel function, and k_s measures the strength of screening, see appendix B. As a test, if we set $k_s = 0$ we obtain the usual $q \rightarrow 0$ logarithmic divergence. If one takes into account the exchange interaction between electrons as well as correlation effects, the polarization function becomes more accurate. In this Hubbard approach, Eq. (3.68), one obtains

$$\chi^{Hub}(q, \omega) = \frac{\chi^0(q, \omega)}{1 - V(q) [1 - G(q)] \chi^0(q, \omega)},$$

where $G(q)$ is the local field factor which for 1D systems $G(q)$, Eq. (3.67), is

$$G(q) = V((q^2 + k_F^2)^{1/2}) / 2V(q).$$

We plot $V(q)$ versus q/k_F in Fig. 6.3 for different k_s . As seen, $V(q)$ decreases with k_s but only for very small q , i.e., only in the long-wavelength limit, and is insensitive to k_s for $q/k_F \geq 0.2$. This behaviour is contrasted with the screened $V(q)$ for 2D graphene in panels (b) and (c): (b) is the RPA result, Eq. (2.23) of Ref. [73] with $1/q \rightarrow 1/\sqrt{q^2 + k_s^2}$ and $\epsilon = \epsilon_0 + (\pi/2)e^2/\hbar v_F$ the effective dielectric constant, while (c) is the Thomas-Fermi one, Eq. (2.23) of Ref. [73] with $V_{sc}^{TF}(q) = (1/\epsilon_0)(2\pi e^2/(q + q_{TF}))$, $q_{TF} = 2\pi e^2 D(E_F)/\epsilon_0$ the Thomas-Fermi wave-vector, and $D(E_F)$ the density of states at the Fermi level. If $D(E_F)$ is broadened due to scattering, q_{TF} can take several values depending on the level width γ . Notice that in (a) $q \equiv q_x$ whereas in (b) and (c) q is the 2D wave vector and $q'_{TF} \equiv q_{TF}/k_F$. Note also that for $k_s \rightarrow 0$, the results in (a) and (b) diverge for $q \rightarrow 0$.

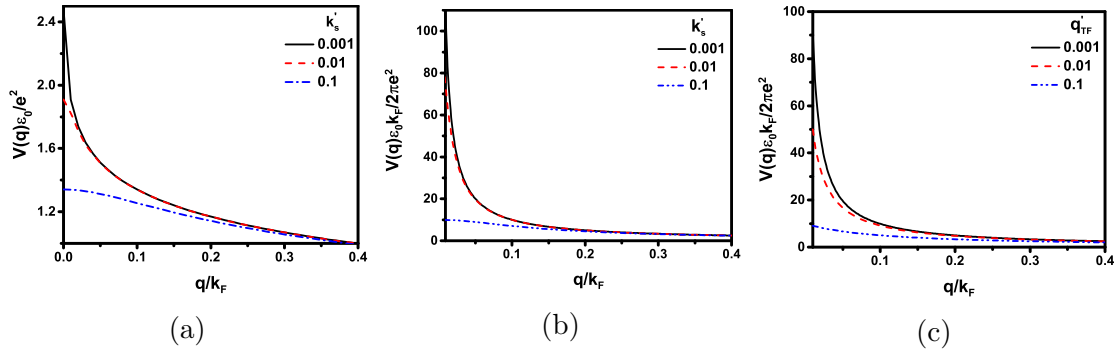


Figure 6.3: Matrix element of the screened potential vs q/k_F in (a) an AGNR for $dm = 14$, $E_F = 0.1$ eV, and 2D graphene in (b) the RPA and (c) Thomas-Fermi approaches.

We now turn to the conductivity given by Eq. (6.13). *In the absence of scattering* we use Eqs. (6.14), (3.54) and (3.68) for $\chi(q, \omega)$, and plot it in Fig. 6.4. For left panel the three “lines” shown in the contour plots follow the roots of the denominators in $\chi(q, \omega)$. We also see that the slope of the Lindhard case increases as we move to the Hubbard and RPA results. This reflects the change in the denominators of χ due to the factors $V(q)$ and $G(q)$ in Eqs. (3.54) and (3.68). The right panel in Fig. 6.4 shown 3D surfaces of the left panel.

To better appreciate the differences between the three approaches we plot cross sections of Fig. 6.4 in Fig. 6.5(a) for fixed $q/k_F = 0.18$ and in Fig. 6.5(b) for fixed $\hbar\omega/E_F = 0.48$. The dependence of the Hubbard conductivity on the width of the AGNR is shown in Fig. 6.6 for widths $dm = 8, 14, 20$. As seen, the dips move to the right with increasing dm . However, we cannot increase dm indefinitely because the 1D potential $V(q)$, given by Eq. (6.15), is less and less valid for increasing dm .

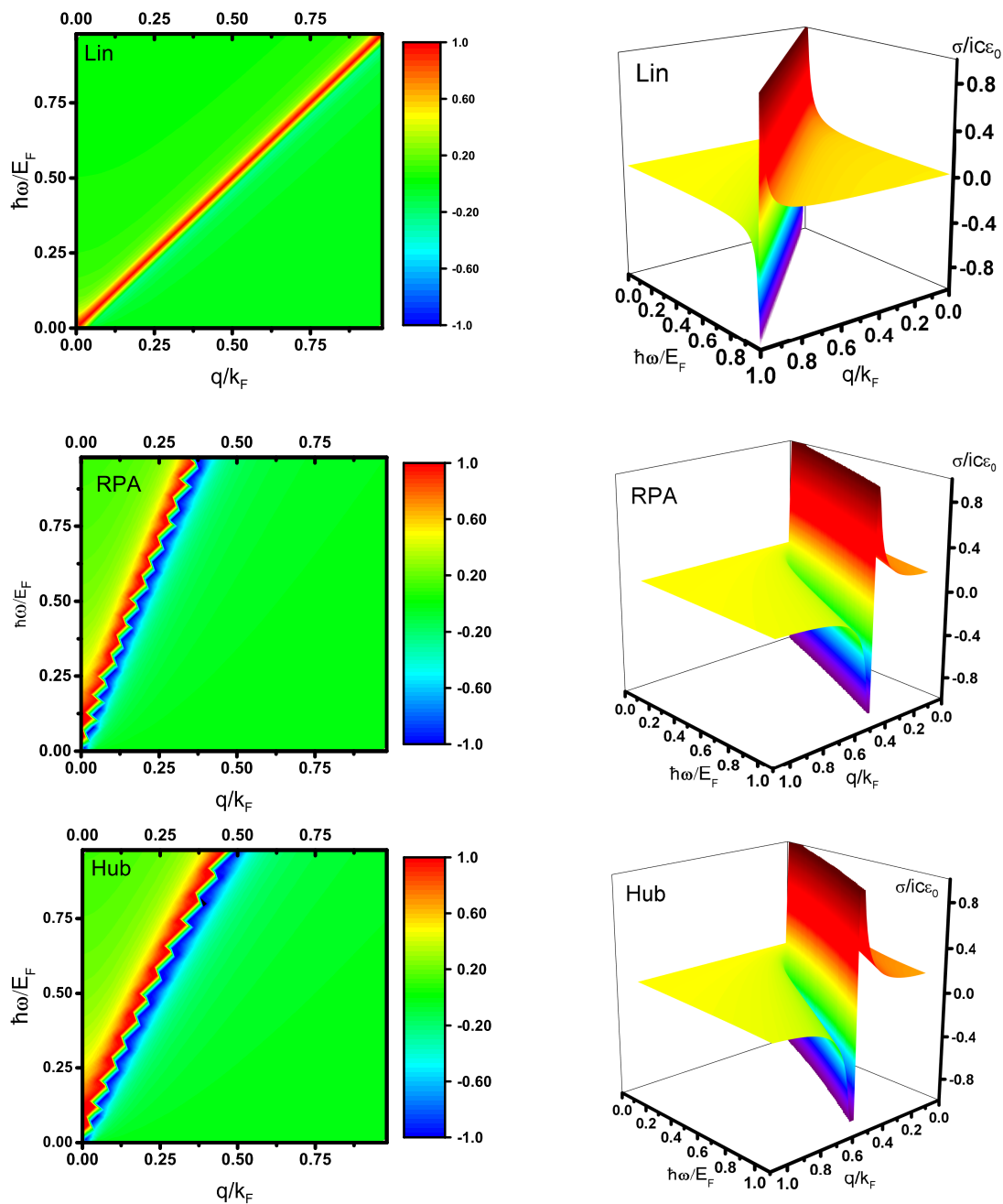


Figure 6.4: 3D surfaces and (ω, q) contour plots of the RPA, Hubbard, and Lindhard conductivities of a metallic AGNR for $dm = 14$ and $E_F = 0.1$ eV.

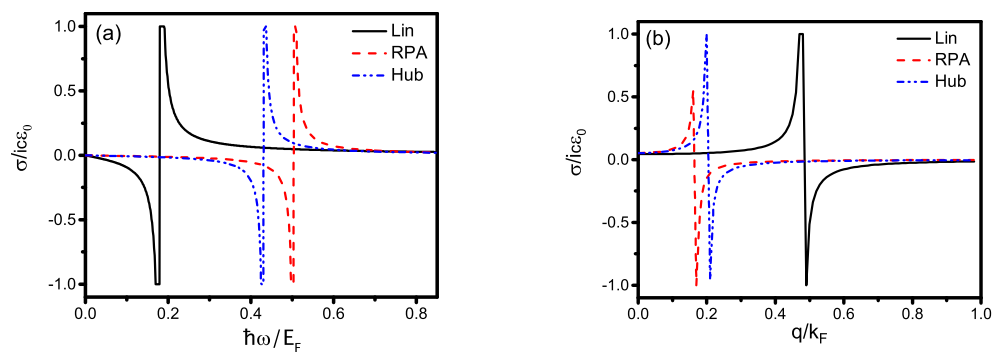


Figure 6.5: Cross sections of Fig. 6.4 for (a) $q/k_F = 0.18$ and (b) $\hbar\omega/E_F = 0.48$.

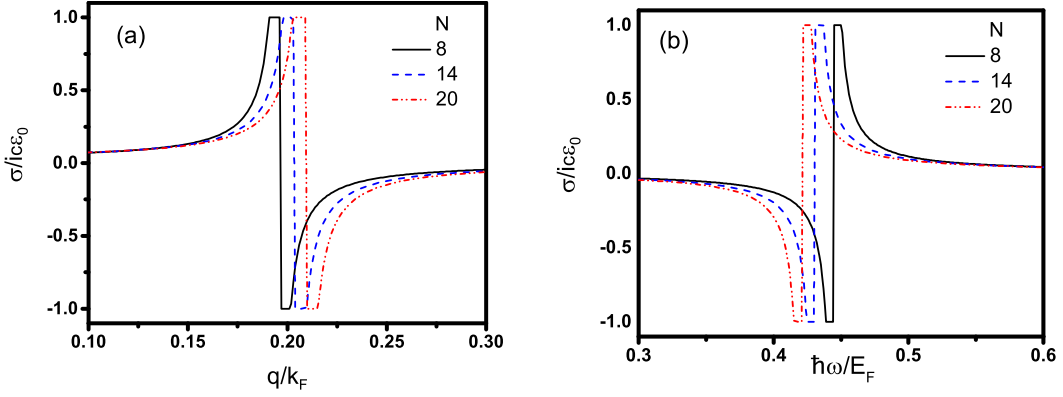


Figure 6.6: Hubbard conductivity for $dm = 8, 14, 20$ and $E_F = 0.1$ eV. Panel (a) is for fixed $\hbar\omega/E_F = 0.48$ and panel (b) for fixed $q/k_F = 0.18$.

6.2 Scattering effect on the polarization function

For scattering by impurities the polarization function in the long-wavelength limit becomes [41]

$$\chi_{im}^0(q, \omega) = \frac{(1 - i\omega\tau) \chi^0(q, \omega + i\gamma)}{1 - i\omega\tau + [\chi^0(q, \omega + i\gamma)/\chi^0(q, 0) - 1]}, \quad (6.16)$$

with $\gamma = 1/\tau$ and τ the relaxation time. In the presence of scattering the conductivity has a real and an imaginary part. In Fig. 6.7 we plot its magnitude, in the long-wavelength limit, for $dm = 14$ and $E_F = 0.1$ eV. The top panels are for $\gamma' = 0$, the middle ones for $\gamma' = 0.001$, and the bottom panels for $\gamma' = 0.03$. As seen, increasing the scattering strength γ , drastically changes its magnitude especially for the right part of the panels in the third row. At the same time we see that increasing γ reduces the slopes of the straight “lines” in Fig. 6.5 and slightly shortens the $\hbar\omega/E_F$ regions of maximal conductivity. As indicated by Eq. (6.16), when scattering is present χ becomes complex and its imaginary part measures the surface plasmon strength [41]. We will consider only the RPA result in the long-wavelength limit. Then

$$\text{Im} \chi^{RPA} = \frac{\text{Im} \chi_{im}^0}{[1 - V(q) \text{Re} \chi_{im}^0]^2 + [V(q) \text{Im} \chi_{im}^0]^2} \quad (6.17)$$

is a measure of the surface plasmon strength that we will plot. Regarding the surface plasmon strength we present, in Fig. 6.8, a (ω, q) contour plot of $-\pi\hbar v_F \text{Im} \chi^{RPA}$. On the first row the three panels are for $\gamma' = 0.001, 0.005, 0.009$, respectively, and screening is neglected. On the second one screening is included and the panels are for $\gamma' = 0.001$, and $k'_s = 0.001, 0.01, 0.1$, respectively.

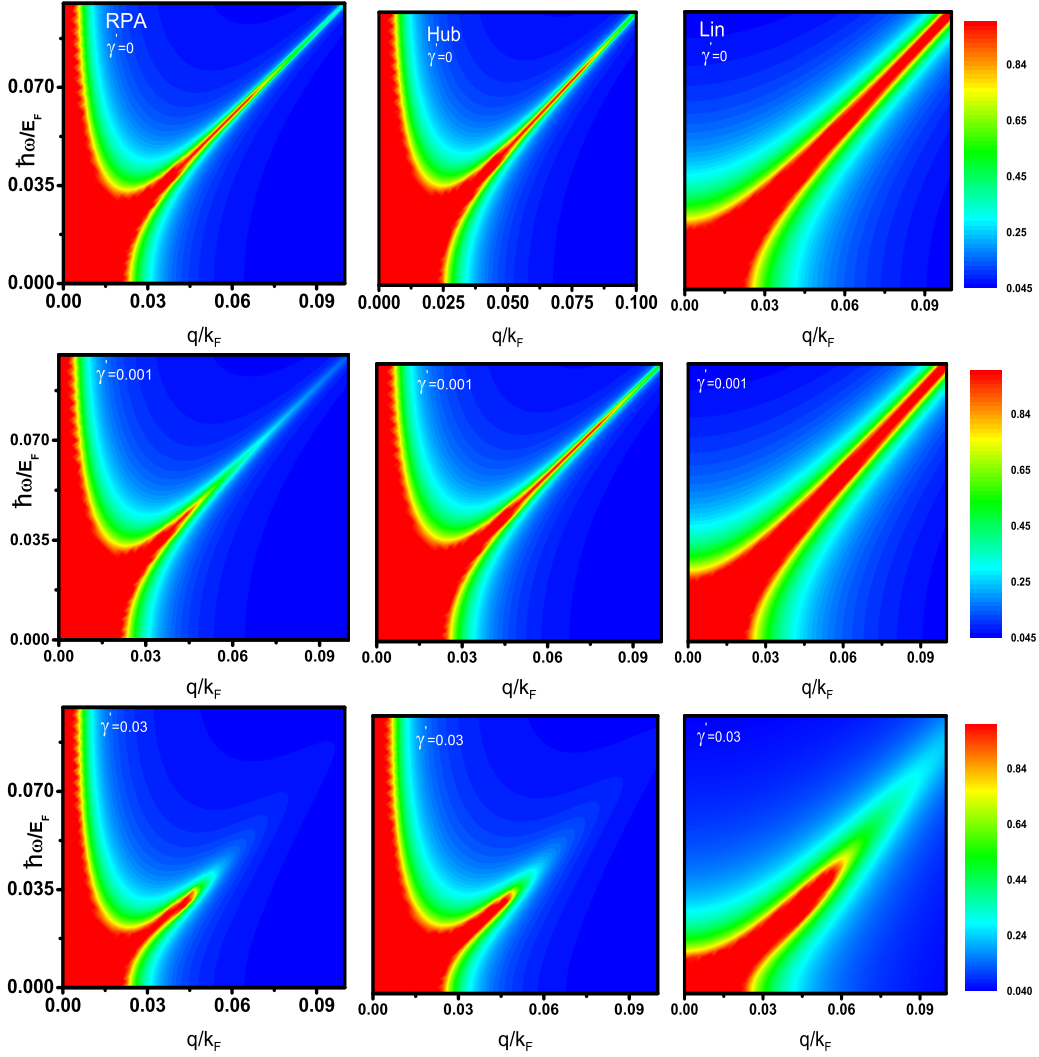


Figure 6.7: (ω, q) amplitude contour plot of the RPA, Hubbard, and Lindhard conductivities of a metallic AGNR, in the long-wavelength limit, for $dm = 14$ and $E_F = 0.1$ eV. The top panels are for $\gamma' = 0$, the middle ones for $\gamma' = 0.001$, and the bottom panels for $\gamma' = 0.03$.

6.3 Reflection amplitude

The reflection amplitude is given by

$$R(\theta, \omega) = (1 - \delta_{\theta, \theta_B}) |r|^2, \quad (6.18)$$

with θ the angle of incidence and θ_B the Brewster angle [74]. In the experiments when phase matching occurs, for a fixed frequency the wave-vector of the incoming field is the same as the surface plasmon, the reflected field that reaches the detector, which measures its amplitude, vanishes. It also vanishes at the Brewster angle. In Figs. 6.9 (a) we plot the RPA reflection amplitude R , given by Eq. (6.18) versus the angle of incidence θ for $dm = 14$, $E_F = 0.1$ eV, $n_1 = 1$ and $n_2 = 2$ in the absence of screening and scattering. A cross section of this graph for $\hbar\omega/E_F = 0.5$ is shown

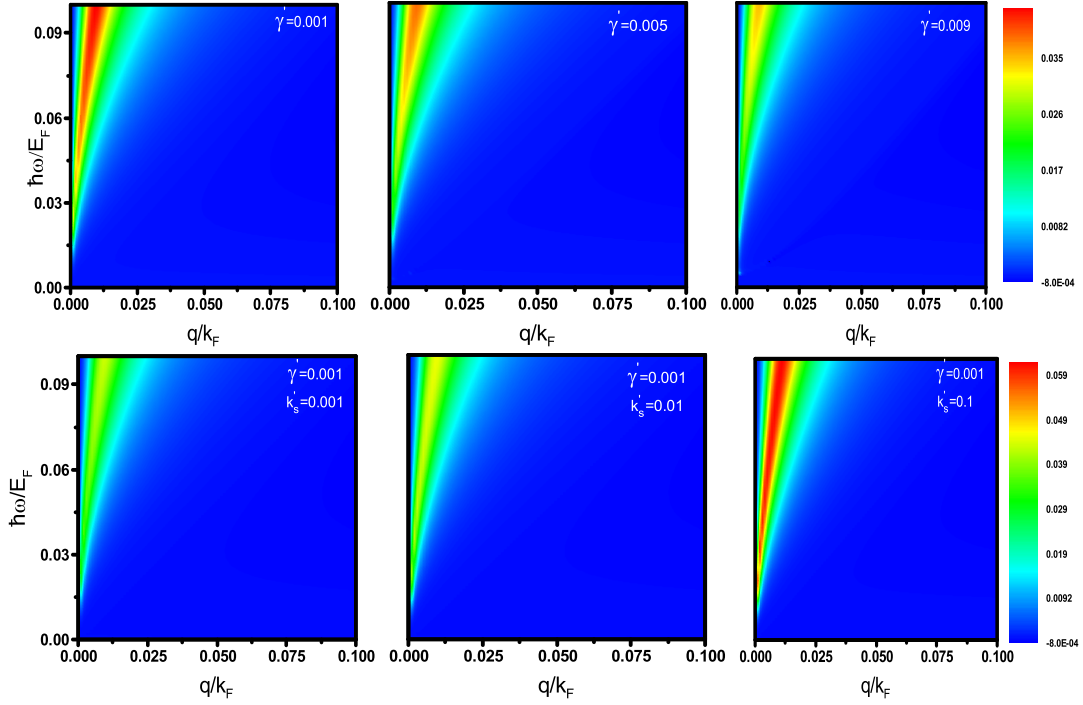


Figure 6.8: (ω, q) contour plot of $-\pi\hbar v_F \text{Im} \chi^{RPA}$ for a metallic AGNR with $dm = 14$ and $E_F = 0.1$ eV. The first row of panels is for an *unscreened* potential with $\gamma' = 0.001, 0.005$, and 0.009 ., the second row for a *screened* one with $\gamma' = 0.001$ and $k'_s = 0.001, 0.01, 0.1$.

in Fig. 6.9 (b) together with the 2D substrate result (dot-dashed blue curve) which shows that the substrate supports Brewster angles. Notice that the two results differ drastically and that there is no Brewster angle in an AGNR. This means that, e.g., in the Kretschmann geometry, if the detector shows a zero value the surface plasmon has been launched.

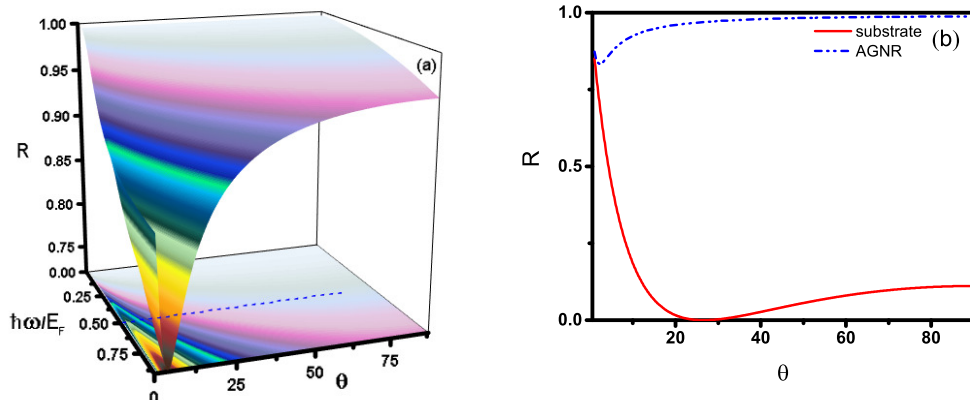


Figure 6.9: (a) RPA Reflection coefficient for $dm = 14$, $E_F = 0.1$ eV, $n_1 = 2$ and $n_2 = 1$ in the absence of screening and scattering. (b) contour of (a). (c) The solid red curve is a cross section of (a) for $\hbar\omega/E_F = 0.5$ and the dot-dashed blue one the result for a 2D substrate.

6.4 AGNR surface plasmons

The pole of reflection coefficient gives rise to surface plasmon. For AGNR from Fig. 6.2 we readily have $\sin \theta_T = k_{2z}/k_2 = k_{2z}c/n_2\omega$ and $\sin \theta_I = k_{1z}/k_1 = k_{1z}c/n_1\omega$. Inserting these expressions in the denominator of Eq. (6.11), set equal to zero, we arrive at

$$\epsilon_1 \left[q^2 - n_1 \frac{\omega^2}{c^2} \right]^{-1/2} + \epsilon_2 \left[q^2 - n_2 \frac{\omega^2}{c^2} \right]^{-1/2} = \frac{\sigma(q, \omega)}{i\omega}. \quad (6.19)$$

Since the wave-vector of surface plasmon is much greater than that of electromagnetic field in vacuum, $\omega/c \ll q$, we can obtain the general expression for surface plasmon as

$$q \simeq \frac{i\omega(\epsilon_1 + \epsilon_2)}{\sigma(q, \omega)}. \quad (6.20)$$

The surface plasmon dispersions are obtained by substituting Eq. (6.13) into Eq. (6.20) and by using $W = \sqrt{3}(dm + 1)a_{cc}/2$ with a_{cc} the carbon-carbon bond length. The results are

$$\hbar\omega/E_F = \sqrt{\lambda^2 + \zeta\lambda}, \quad \text{Lindhard}, \quad (6.21)$$

$$\hbar\omega/E_F = \sqrt{\lambda^2(1 + \lambda\beta_\lambda) + \zeta\lambda}, \quad \text{RPA}, \quad (6.22)$$

$$\hbar\omega/E_F = \sqrt{\lambda^2(1 + \lambda\gamma_\lambda) + \zeta\lambda}, \quad \text{Hubbard}. \quad (6.23)$$

Here $dm = 3m - 1$, m is an integer,

$$\zeta = 2e^2 / [\pi\sqrt{3}(\epsilon_1 + \epsilon_2)a_{cc}E_F] (N/(N + 1)), \quad (6.24)$$

$$\beta_\lambda = \frac{2e^2}{\hbar v_F \epsilon_0} \int_0^1 \int_0^1 K_0[\delta_\lambda |(y - y')|] dy dy', \quad \lambda \equiv q/k_F \quad (6.25)$$

with $\gamma_\lambda = \beta_\lambda - 0.5\beta_{\lambda'}$, and $\lambda' = (\sqrt{1 + \lambda^2})$. As a test, we expect that in the long-wavelength limit the surface plasmon dispersion becomes that of graphene [71] for W or N sufficiently large. Indeed, for N very large $N/(N + 1) \rightarrow 1$ and $\lambda \ll 1$ we have $\hbar\omega/E_F \propto \sqrt{\lambda}$ as in graphene's case [71, 75, 76, 77, 78, 79]. Furthermore, in the long-wavelength limit the surface plasmon field is proportional to $\zeta^{1/2}$ or $1/\sqrt{W}$ in line with expectations [80, 81, 82] and observations Ref [83, 84].

In Fig. 6.10 we plot the Lindhard and Hubbard TM surface plasmon dispersions for different widths ($dm = 5, 8, 20$) of a metallic AGNR, with $n_1 = 1, n_2 = 2$, and $E_F = 0.1$ eV. For fixed energy, especially in the long-wavelength limit, the surface plasmon wavelength increases with the width W of the AGNR and so does the surface plasmon group velocity. The opposite occurs when W is decreased. The RPA result is similar to the fully numerical ones of Refs. [85, 86, 87, 88].

The dm dependence shown in Fig. 6.10 can be understood as follows. The energy of a system in an electromagnetic field is directly related to the induced polarization which leads to a charge density oscillation. The polarization can be considered as an ensemble of dipole moments. For an oscillation with specific displacement from equilibrium, by increasing the number of dipole moments, which in an AGNR is

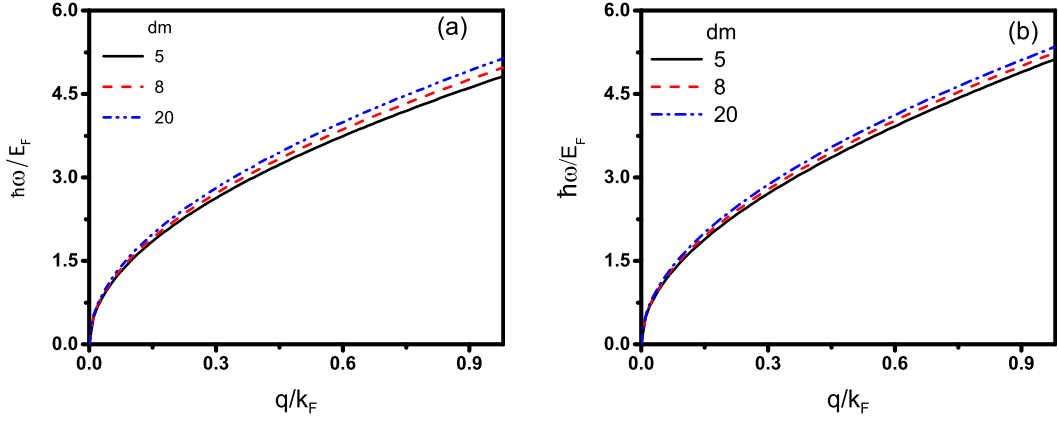


Figure 6.10: (a) TM Lindhard and (b) Hubbard surface plasmon dispersions in a metallic AGNR with $n_1 = 2, n_2 = 1$, and $E_F = 0.1$ eV. From top to bottom the AGNR width is $dm = 5, 8, 20$.

proportional to the width W (or the dimmer number dm), the generated electromagnetic field has more energy. Therefore, we expect that, as shown in Fig. 4, its frequency or photon energy to increase with the AGNR width W .

In Fig. 6.11 (a) we contrast the TM Lindhard, RPA, and Hubbard SP dispersions for $dm = 8$. As Fig. 6.11 (b) shows, even in the long-wavelength limit there is a small but noticeable difference between them.

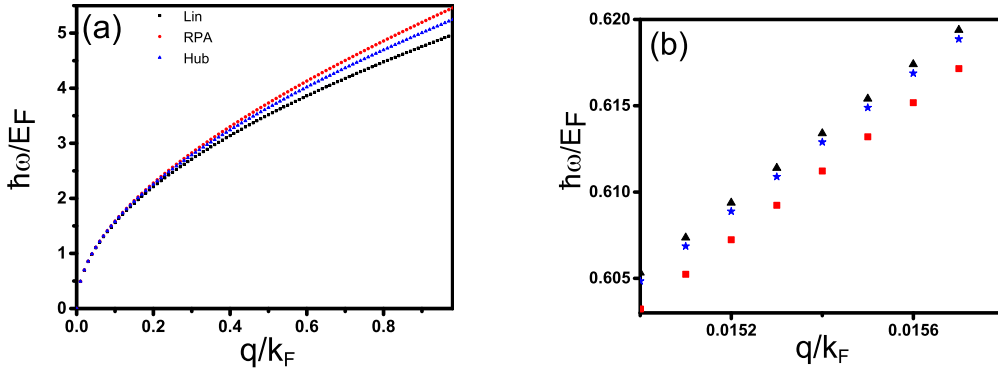


Figure 6.11: TM Lindhard, RPA, and Hubbard surface plasmon dispersions in a AGNR for $E_F = 0.1$ eV and width $dm = 8$ for (a) $q/k_F \leq 1$ and (b) long wavelength limit, $q/k_F \rightarrow 0$.

The difference between the dispersions shown in Fig. 6.11 can be understood as follows. The strength of the charge displacement/polarization due to a electromagnetic field is reduced when, e.g., we take into account electron-electron interaction and go from Eq. (8) to Eq. (9) and subsequently to Eq. (11) upon including exchange. To have the same polarization, which determines the surface plasmon photon energy, as in the case without electron-electron interaction, the charge displacement must be increased. Then the uncertainty principle indicates that the modified momentum ($\propto q$) is smaller. In addition, from photon energy conservation one can conclude that for a specific surface plasmon mode its intensity in the Lindhard case is stronger than in Hubbard and RPA cases because of the surface plasmon wavelength increase in the former case as compared to the latter ones.

6.5 TE transmission and reflection coefficients

By satisfying the boundary conditions for the normal and tangential components of the magnetic field B in Maxwell's equations, see Fig. 6.2 with the electric field E replaced by $B = \mu H$, the tangential components give

$$H_2^{\parallel} - H_1^{\parallel} = \vec{k}_f \times \hat{n}, \quad (6.26)$$

with \vec{k}_f the vector of free surface current, and the normal components

$$B_2^{\perp} - B_1^{\perp} = 0. \quad (6.27)$$

For simplicity we assume $\mu_1 = \mu_2 = \mu_0$. Also, $\theta_I = \theta_R$ and $n_2 \cos \theta_T = n_1 \cos \theta_I$. Then Eqs. (6.26) and (6.27) are first rewritten in terms of B_I, B_R , and B_T , similar to Eqs. (6.2) and (6.4), and then in terms of the refractive indices like Eqs. (6.8) and (6.9). The result is

$$1 - r = t \left(\frac{n_1}{n_2} + \frac{\sigma_{yy}}{n_2 \epsilon_0 \sin \theta_T} \right) \frac{\sin \theta_T}{\sin \theta_I}, \quad (6.28)$$

$$1 + r = t. \quad (6.29)$$

From Eqs. (6.28) and (6.29) we readily obtain

$$t = 2 \left[1 + \left(\frac{n_1}{n_2} + \frac{\sigma_{yy}}{n_2 \epsilon_0 \sin \theta_T} \right) \frac{\sin \theta_T}{\sin \theta_I} \right]^{-1}. \quad (6.30)$$

For graphene nanoribbons we have $\sigma_{yy} = 0$. Then the pole of the transmission amplitude does not lend any support to TE surface plasmons [89].

7 Scattering effects on linear response theory

7.1 Introduction

Let's assume that the system is at thermal equilibrium. Indeed, this is a consequence of the connection between dissipation and fluctuations in the system. The former is responsible for an irreversible decay of observables towards their equilibrium and the latter is intertwined with the preservation of the correct statistical distribution. As a matter of fact, in the classical regime energy dissipation in a system is related to the statistical fluctuations which occur in thermal equilibrium. Brownian motion is a prime example; its analysis provides great insight into the concept of energy dissipation in a system. For the sake of simplicity, we limit our calculations to one-dimensional systems. Newton's second law of motion for a particle with mass is

$$m \frac{dv}{dt} = \mathfrak{F}(t) + F(t), \quad (7.1)$$

where \mathfrak{F} denotes the external field which can be, for instance, an electromagnetic field. $F(t)$ stands for the net force that tends to restore the particle to equilibrium. Since $F(t)$ describes the interaction of a particle with all other degrees of freedom, it is expected to have fluctuating behavior over time. Therefore, the particle velocity and the net force can be written as

$$v = \bar{v} + v', \quad (7.2)$$

$$F = \bar{F} + F', \quad (7.3)$$

where \bar{v} and \bar{F} are the average parts and v' and F' are the rapidly fluctuating parts whose average value vanishes. \bar{F} is a function of \bar{v} , which can be expressed in terms of power series of \bar{v} [90]. Hence, we can rewrite \bar{F} as

$$\bar{F} = -\alpha\bar{v} + \beta'\bar{v}^2 - \gamma'\bar{v}^3 + \dots \quad (7.4)$$

For the linear case, we have

$$\bar{F} = -\alpha\bar{v}, \quad (7.5)$$

where the coefficient, α , is positive due to the fact that \bar{v} needs to decrease as time increases. In general, Eq. (7.1) becomes

$$m \frac{d\bar{v}}{dt} = \mathfrak{F} + \bar{F} = \mathfrak{F} - \alpha\bar{v}, \quad (7.6)$$

where it can be written in terms of v as

$$m \frac{dv}{dt} = \mathfrak{F} - \alpha v + F'(t). \quad (7.7)$$

In Eq. (7.7) we assumed $\alpha \bar{v} \approx \alpha v$. Eq. (7.7) is known as the ‘‘Langevin equation.’’ Note that, $-\alpha v$ indicates the existence of processes, that is frictional forces, which are associated with the dissipation of energy. It is useful to point out that what we did in the Drude model derivation is analogous to the Eq. (7.7). The solution for the average ensemble of Eq. (7.7) is

$$m \langle v(t + \tau) - v(t) \rangle = \mathfrak{F}(t)\tau - \frac{1}{k_B T} \int_t^{t+\tau} dt' \int_{t-t'}^0 ds K(s), \quad (7.8)$$

where $\langle \dots \rangle_0$ indicates the mean value, k_B is Boltzmann constant, and $K(s)$ is the ensemble average

$$K(s) = \langle F(t')F(t' + s) \rangle_0, \quad (7.9)$$

which is also called the ‘‘correlation function.’’ After some algebra, we obtain

$$m \langle v(t + \tau) - v(t) \rangle = \mathfrak{F}(t)\tau - \alpha \bar{v}(t)\tau, \quad (7.10)$$

where α is given by

$$\alpha \equiv \frac{1}{k_B T} \int_{-\infty}^{\infty} ds \langle F(0)F(s) \rangle_0. \quad (7.11)$$

By assuming that $\bar{v} = \langle v \rangle$ changes slowly over time intervals on the order of τ , Eq. (7.10) leads to Eq. (7.6). It is worth pointing out that α in the Drude model corresponds to γ in Eq. (2.26). Notice there is a very close connection between the correlation function and the energy dissipation of a system. In the quantum regime, the structure factor $S(\vec{q}, \omega)$ is given by [50]

$$S(\vec{q}, \omega) = \int_{-\infty}^{\infty} dt e^{i\omega t} \langle \hat{\rho}(\vec{q}, t) \hat{\rho}(-\vec{q}, 0) \rangle. \quad (7.12)$$

Furthermore, the definition of the polarization function in momentum and frequency space is

$$\chi^0(\vec{q}, \omega) = -\frac{i}{\hbar V} \int_{-\infty}^{\infty} dt e^{i\omega t} \theta(t) [\langle \hat{\rho}(\vec{q}, t) \hat{\rho}(-\vec{q}, 0) \rangle - \langle \hat{\rho}(-\vec{q}, 0) \hat{\rho}(\vec{q}, t) \rangle], \quad (7.13)$$

after algebraic manipulation yields

$$\chi^0(\vec{q}, \omega) = \frac{1}{\hbar V} \int_{-\infty}^{\infty} \frac{d\nu}{2\pi} \frac{S(\vec{q}, \nu) - S(\vec{q}, -\nu)}{\omega - \nu + i\eta}, \quad (7.14)$$

which we used

$$\theta(t) = \lim_{\eta \rightarrow 0^+} \frac{1}{i2\pi} \int_{-\infty}^{\infty} d\omega \frac{e^{i\omega t}}{\omega - i\eta}. \quad (7.15)$$

Using the eigenvalue and eigenfunction of the Hamiltonian

$$H |n\rangle = E_n |n\rangle$$

Eq. (7.12) becomes

$$S(\vec{q}, \omega) = 2\pi\hbar \sum_{i,j} \frac{e^{-\beta E_i}}{Z} |\langle i | \hat{\rho}(\vec{q}, 0) | j \rangle|^2 \delta(E_i - E_j + \hbar\omega). \quad (7.16)$$

Note that $S(\vec{q}, \omega) \geq 0$. We also have the following relation [41]

$$S(-\vec{q}, \omega) = S(\vec{q}, \omega) = e^{\beta\hbar\omega} S(\vec{q}, -\omega). \quad (7.17)$$

From Eqs. (7.14) and (7.17) we find

$$(e^{-\beta\hbar\omega} - 1) S(\vec{q}, \omega) = 2\hbar V \Im \chi^0(\vec{q}, \omega), \quad (7.18)$$

which states the connection between the structure factor and the imaginary part of the polarization function. Indeed, we see the dissipation of a system is related to the imaginary part of its polarization function.

7.2 A challenge for quantum linear response theory

We expect that the results we obtained from linear response theory in the quantum regime reduce to the classical ones in the appropriate limit. For instance, Eq. (3.56), which expresses the permittivity of a system, gives rise to Eq. (2.42) in the long wavelength limit for a free electron gas. Applying the long-wavelength limit to Eq (3.56), we have

$$\epsilon(q \rightarrow 0, \omega) = 1 - V(q) \chi^0(q \rightarrow 0, \omega), \quad (7.19)$$

which, using Eq. (3.72), gives

$$\epsilon(q \rightarrow 0, \omega) = 1 - \frac{4\pi e^2}{\epsilon_0 q^2} \frac{1}{L^d} \lim_{\nu \rightarrow 0} \sum_{\vec{k}} f(\vec{k}) \left[\frac{E(\vec{q} + \vec{k}) - E(\vec{k})}{(\hbar\omega + i\nu)^2} + \frac{[E(\vec{q} + \vec{k}) - E(\vec{k})]^3}{(\hbar\omega + i\nu)^4} + \dots \right], \quad (7.20)$$

where, by substituting the energy spectrum from Eq. (3.70), we obtain

$$\epsilon(q \rightarrow 0, \omega) = 1 - \frac{4\pi e^2}{\epsilon_0 q^2} \frac{1}{L^d} \lim_{\nu \rightarrow 0} \sum_{\vec{k}} f(\vec{k}) \left[\frac{1}{(\hbar\omega + i\nu)^4} \frac{\hbar^2 q^2}{2m} + \frac{1}{(\hbar\omega + i\nu)^4} \frac{\hbar^6}{2m^3} 12q^2 (\vec{k} \cdot \vec{q})^2 + O(q^6) \right]. \quad (7.21)$$

Note that

$$\frac{1}{L^d} \sum_{\vec{k}} f(\vec{k}) = n \quad \text{and} \quad \frac{1}{L^3} \sum_{\vec{k}} f(\vec{k}) \left(\frac{\hbar k}{m} \right)^2 = \frac{3}{10} v_F^2 n,$$

where n is the electron density. Employing the above expressions, Eq. (7.21) becomes

$$\epsilon(q \rightarrow 0, \omega) = 1 - \frac{\omega_p^2}{(\omega + i\nu/\hbar)^2} - \frac{3}{5} \frac{\omega_p^2}{(\omega + i\nu/\hbar)^4} v_F^2 q^2 + \dots, \quad (7.22)$$

where we can neglect higher orders terms. This gives

$$\epsilon(q \rightarrow 0, \omega) = 1 - \frac{\omega_p^2}{\omega^2 + i\omega 2\nu/\hbar}. \quad (7.23)$$

In order to retrieve Eq. (2.35) in the literature usually one replaces $2\nu/\hbar$ with $1/\tau$. In fact, ν designates the coupling of the system to its environment. Then, it is simply replaced by $1/\tau$. But such a interpretation is not correct. Below we argue why. In developing the density-density response function, Eq. (3.30), ν was introduced as an adiabatic switching-on of the perturbation to avoid a divergence in an integration over time and satisfy causality. As seen in Eq. (7.23), to retrieve Drude's result for the conductivity in the long wavelength limit, usually one enters this parameter into the final result phenomenologically [41]. The dissipation should originate from some randomness in the system which should appear in the Hamiltonian. This randomness term, for example, could represent one-body or two-body randomizing collisions [51]. In the next section, we develop a density-density response function for inhomogeneous systems and investigate the influence of this randomness term (or scattering).

7.3 Linear response theory in the presence of impurities

In order to treat the impurity effects, corresponding to frictional forces in the classical regime, we consider a system whose Hamiltonian is given by

$$H = H_0 - AF(t) + \lambda V, \quad (7.24)$$

which contains an extra term, λV , compared to Eq. (3.1). This term introduces the effects of electron-impurity or electron-phonon interaction and so on. The λ determines the strength of these kind of interactions. To be in the linear-response regime some conditions are required to be satisfied which they are

$$\langle AF(t) \rangle, \langle \lambda V \rangle \ll \langle H_0 \rangle. \quad (7.25)$$

Indeed, the introduction of new term in the Hamiltonian alters time evolution of operators which definitely changes the polarization function of a system. The first person who tried to come up with a solution to this was Van Hove in which his publication in 1955 stated that [51]

$$\lambda \rightarrow 0, \quad t/\tau_t \rightarrow \infty, \quad \lambda^2 t = \text{finite}, \quad (7.26)$$

this limit alters the time evolution of an operator in the manner

$$c_l(t) = e^{-\Lambda_l t} c_l + e^{iH_0 t/\hbar} c_l e^{-iH_0 t/\hbar}, \quad (7.27)$$

where τ_t is the transition time and Λ is a super-operator defined by

$$\Lambda \hat{c} \equiv \sum_{i,j} |i\rangle \langle i| [W_{ji} \langle j|\hat{c}|j\rangle - W_{ij} \langle i|\hat{c}|i\rangle]; \quad (7.28)$$

the transition rate W_{ij} given by Fermi's golden rule

$$W_{ij} = (2\pi\lambda^2/\hbar) |\langle i|v|j\rangle|^2 \delta(E_i - E_j). \quad (7.29)$$

It is useful to point out that Eq. (7.27) satisfies the equation of motion, $i\hbar\partial_t c_l(t) = [c_l(t), H_0 + \lambda V]$ in the van Hove limit. For the sake of simplicity in the following calculations we rewrite the Eq. (7.27) as

$$c_l(t) = c_l^{im}(t) + c_l^{non}(t), \quad (7.30)$$

where c_l^{im} and c_l^{non} are

$$c_l^{im}(t) = e^{-\Lambda_l t} c_l, \quad (7.31)$$

$$c_l^{non}(t) = e^{iH_0 t/\hbar} c_l e^{-iH_0 t/\hbar}. \quad (7.32)$$

Here we evaluate the density correlation function which is

$$\langle \Phi'_0 | [\rho(\vec{r}, t), \rho(\vec{r}', t')] | \Phi'_0 \rangle, \quad (7.33)$$

with $|\Phi'_0\rangle$ being

$$|\Phi'_0\rangle = |\Phi_0\rangle \otimes |\xi\rangle \quad (7.34)$$

where $|\Phi_0\rangle$ indicates the wave function of electron and $|\xi\rangle$ refers to that of the impurity or phonon. From Eqs. (7.30) and (7.33) we obtain

$$\langle \Phi'_0 | [\rho^{im}(\vec{r}, t) + \rho^{non}(\vec{r}, t), \rho^{im}(\vec{r}', t') + \rho^{non}(\vec{r}', t')] | \Phi'_0 \rangle, \quad (7.35)$$

by splitting which we have

$$\begin{aligned} & \langle \Phi'_0 | [\rho^{im}(\vec{r}, t), \rho^{im}(\vec{r}', t')] | \Phi'_0 \rangle + \langle \Phi'_0 | [\rho^{non}(\vec{r}, t), \rho^{non}(\vec{r}', t')] | \Phi'_0 \rangle \\ & + \langle \Phi'_0 | [\rho^{im}(\vec{r}, t), \rho^{non}(\vec{r}', t')] | \Phi'_0 \rangle + \langle \Phi'_0 | [\rho^{non}(\vec{r}, t), \rho^{im}(\vec{r}', t')] | \Phi'_0 \rangle, \end{aligned} \quad (7.36)$$

where by some algebra one can find out that the last two terms vanish. From Eqs. (7.31) and (7.32) we obtain

$$\langle \Phi'_0 | [\rho^{im}(\vec{r}, t), \rho^{im}(\vec{r}', t')] | \Phi'_0 \rangle = \sum_{i,j} \sum_{m,n} \phi_i^*(\vec{r}) \phi_j(\vec{r}) \phi_m^*(\vec{r}') \phi_n(\vec{r}') \Upsilon_{ijmn}, \quad (7.37)$$

with

$$\Upsilon_{ijmn} \equiv \langle \Phi'_0 | [e^{-\Lambda_i t} e^{-\Lambda_j t} c_i^\dagger c_j, e^{-\Lambda_m t} e^{-\Lambda_n t} c_m^\dagger c_n] | \Phi'_0 \rangle, \quad (7.38)$$

which becomes

$$\Upsilon_{ijmn} \equiv \langle \xi | e^{-(\Lambda_i + \Lambda_j)t} e^{-(\Lambda_m + \Lambda_n)t'} | \xi \rangle \langle \Phi_0 | [c_i^\dagger c_j, c_m^\dagger c_n] | \Phi_0 \rangle, \quad (7.39)$$

for single-body collisions such as electron-phonon interaction. The second term in the above equation has been evaluated in the derivation of the polarization function. Therefore, we focus on

$$\Upsilon_{ijmn} \equiv \langle \xi | e^{-(\Lambda_i + \Lambda_j)t} e^{-(\Lambda_m + \Lambda_n)t'} | \xi \rangle (f_i - f_j) \delta_{ni} \delta_{jm}. \quad (7.40)$$

If we multiply the correlation function in Eq. (7.33) by $\Theta(t - t')/i\hbar$ we obtain the polarization function. From Eqs. (7.35) and (7.36) we arrive at

$$\begin{aligned} \chi^0(\vec{r}, t; \vec{r}', t') &= -\frac{i}{\hbar}\Theta(t - t') \left\langle \Phi'_0 \left| \left[\rho^{im}(\vec{r}, t), \rho^{im}(\vec{r}', t') \right] \right| \Phi'_0 \right\rangle \\ &\quad - \frac{i}{\hbar}\Theta(t - t') \left\langle \Phi'_0 \left| \left[\rho^{non}(\vec{r}, t), \rho^{non}(\vec{r}', t') \right] \right| \Phi'_0 \right\rangle, \end{aligned} \quad (7.41)$$

or in a more compact form

$$\chi^0(\vec{r}, t; \vec{r}', t') = \chi_{im}^0(\vec{r}, t; \vec{r}', t') + \chi_{non}^0(\vec{r}, t; \vec{r}', t'). \quad (7.42)$$

The second term on the right hand side of Eq.(7.42) leads to the previous results obtained for the polarization function in the absence of λV , which is

$$\begin{aligned} & -\frac{i}{\hbar}\Theta(t - t') \left\langle \Phi'_0 \left| \left[\rho^{non}(\vec{r}, t), \rho^{non}(\vec{r}', t') \right] \right| \Phi'_0 \right\rangle \\ &= -\frac{i}{\hbar}\Theta(t - t') \left\langle \Phi_0 \left| \left[\rho^{non}(\vec{r}, t), \rho^{non}(\vec{r}', t') \right] \right| \Phi_0 \right\rangle \underbrace{\langle \xi | \xi \rangle}_{=1} = \chi_{non}^0(\vec{r}, t; \vec{r}', t'). \end{aligned} \quad (7.43)$$

The first term on the RHS of the Eq.(7.42) becomes

$$\chi_{im}^0(\vec{r}, t; \vec{r}', t') = -\frac{i}{\hbar}\Theta(t - t') \sum_{i,j} \sum_{m,n} \phi_i^*(\vec{r}) \phi_j(\vec{r}) \phi_m^*(\vec{r}') \phi_n(\vec{r}') \Upsilon_{ijmn}. \quad (7.44)$$

By changing $t \rightarrow t - t'$ in Eq. (7.44) by some simple algebra we obtain

$$\chi_{im}^0(\vec{r}, \vec{r}', t) = -\frac{i}{\hbar}\Theta(t) \sum_{i,j} \phi_i^*(\vec{r}) \phi_j(\vec{r}) \phi_j^*(\vec{r}') \phi_i(\vec{r}') \langle \xi | e^{-\Lambda_{ij}t} | \xi \rangle (f_i - f_j), \quad (7.45)$$

with

$$\Lambda_{ij} \equiv \Lambda_i + \Lambda_j. \quad (7.46)$$

By multiplying both sides of Eq. (7.44) by $e^{-i\omega t}$ and integrating it, we obtain Eq. (7.45) in frequency domain

$$\chi_{im}^0(\vec{r}, \vec{r}', \omega) = \sum_{i,j} \phi_i^*(\vec{r}) \phi_j(\vec{r}) \phi_j^*(\vec{r}') \phi_i(\vec{r}') \langle \xi | \frac{1}{\hbar(\omega + i\Lambda_{ij})} | \xi \rangle (f_i - f_j). \quad (7.47)$$

7.4 Current-current density response

In general, quantities such as conductivity are tensors. In order to obtain the components of conductivity tensor we employ current-current response function formula which is defined by

$$\chi_{\alpha\beta}(\vec{r}, \vec{r}', t, t') = -\frac{i}{\hbar}\Theta(t - t') \left\langle \left[j_\alpha(\vec{r}, t), j_\beta(\vec{r}', t') \right] \right\rangle_0, \quad (7.48)$$

whose space-time Fourier transformation is

$$\chi_{\alpha\beta}(\vec{q}, \vec{q}', \omega, \omega') = -\frac{i}{\hbar} \left\langle \left[j_{\alpha}(\vec{q}, \omega), j_{\beta}(\vec{q}', \omega') \right] \right\rangle_0. \quad (7.49)$$

To evaluate the component of current operator, we use continuity equation

$$\frac{\partial \rho(\vec{r}, t)}{\partial t} + \vec{\nabla} \cdot \vec{J}(\vec{r}, t) = 0.$$

By expressing the operators as

$$\begin{aligned} \rho(\vec{r}, t) &= \frac{1}{V} \sum_{\vec{k}} \int_{-\infty}^{\infty} \frac{\partial \omega}{2\pi} \rho(\vec{k}, \omega) e^{i\vec{k} \cdot \vec{r} - \omega t}, \\ \vec{J}(\vec{r}, t) &= \frac{1}{V} \sum_{\vec{k}} \int_{-\infty}^{\infty} \frac{\partial \omega}{2\pi} \vec{J}(\vec{k}, \omega) e^{i\vec{k} \cdot \vec{r} - \omega t}, \end{aligned}$$

after some algebra we arrive at

$$-i\omega \rho(\vec{q}, \omega) + i\vec{q} \cdot \vec{J}(\vec{q}, \omega) = 0 \Rightarrow J_{\alpha}(\vec{q}, \omega) = \frac{\omega}{q_{\alpha}} \rho(\vec{q}, \omega), \quad (7.50)$$

with $\alpha \equiv x, y, z$. Combining Eqs. (7.49) and (7.50) we can rewrite current-current response in terms of density-density response

$$\chi_{\alpha\beta}(\vec{q}, \vec{q}', \omega, \omega') = \frac{\omega \omega'}{q_{\alpha} q'_{\beta}} \left(-\frac{i}{\hbar} \left\langle \left[\rho(\vec{q}, \omega), \rho(\vec{q}', \omega') \right] \right\rangle_0 \right), \quad (7.51)$$

We already know that the quantity in the parentheses is $\chi^0(\vec{q}, \vec{q}', \omega, \omega')$. Then, we have

$$\chi_{\alpha\beta}(\vec{q}, \vec{q}', \omega, \omega') = \frac{\omega \omega'}{q_{\alpha} q'_{\beta}} \chi^0(\vec{q}, \vec{q}', \omega, \omega'). \quad (7.52)$$

In the same manner that we showed $\chi^0(\vec{q}, \vec{q}', \omega, \omega') = \chi^0(\vec{q}, \omega) \delta_{\vec{q}, -\vec{q}'} \delta_{\omega, \omega'}$, It can be shown that

$$\chi_{\alpha\beta}(\vec{q}, \vec{q}', \omega, \omega') = \chi_{\alpha\beta}(\vec{q}, \omega) \delta_{\vec{q}, -\vec{q}'} \delta_{\omega, \omega'}. \quad (7.53)$$

Finally, Eq. (7.52) becomes

$$\chi_{\alpha\beta}(\vec{q}, \omega) = \frac{\omega^2}{q_{\alpha} q_{\beta}} \chi^0(\vec{q}, \omega). \quad (7.54)$$

From the connection between conductivity and current-current response we find

$$\sigma_{\alpha\beta}^0(\vec{q}, \omega) = \frac{ie^2}{\omega} \chi_{\alpha\beta}(\vec{q}, \omega) = \frac{ie^2 \omega}{q_{\alpha} q_{\beta}} \chi^0(\vec{q}, \omega). \quad (7.55)$$

7.5 Plasmons in graphene in the presence of impurities

As we mentioned, from the density-density response function (DDRF) many properties such as plasmons, reflection and transmission amplitudes can be evaluated. Below we investigate graphene plasmons in the random-phase approximation.

For low energies from the Eqs. (4.45) and (4.46) we evaluated single-band (SB) and two-band (TB) transition. Here, for the sake of the simplicity of expression we rewrite them in terms of dimensionless parameters. That is,

$$\chi_{non}^{0,SB}(q', \omega') = \frac{k_F}{\pi \hbar v_F} \frac{q'^2}{\omega'^2}, \quad (7.56)$$

$$\chi_{non}^{0,TB}(q', \omega') = \frac{k_F}{\pi \hbar v_F} \frac{q'^2}{2\omega'} \left[A(\omega') - i \frac{\pi}{2} \Theta(\omega' - 2) \right], \quad (7.57)$$

where we used the dimensionless parameters q' and ω' ($q' \equiv q/k_F$, $\omega' \equiv \hbar\omega/E_F$), with

$$A(\omega') = \frac{2}{\omega'} + \frac{1}{2} \ln \left| \frac{2 - \omega'}{2 + \omega'} \right|. \quad (7.58)$$

As for $\chi_{im}^{0,SB}$, by employing Eqs. (4.45), (4.46), and (4.46) we obtain

$$\chi_{im}^{0,SB}(q', \omega') = \frac{k_F}{2\pi \hbar v_F} C(\omega', \gamma') (1 - \delta_{\gamma',0}), \quad (7.59)$$

with

$$C(\omega', \gamma') = \frac{\omega' - i\gamma'}{\omega'^2 + \gamma'^2}, \quad \gamma' \equiv \hbar\gamma/E_F. \quad (7.60)$$

Although $\langle \Lambda \rangle_b$ is a function of momentum, for simplicity in the derivation of Eq. (7.59) it has been replaced by $\tau/2$ where τ is the relaxation time and $\gamma = 1/\tau$; this is valid only for elastic scattering. For TB transitions $\chi_{im}^{0,TB}$ is given by

$$\chi_{im}^{0,TB}(q', \omega') = \frac{k_F}{\pi \hbar v_F} C(\omega', \gamma') (1 - \delta_{\gamma',0}). \quad (7.61)$$

The DDRF in momentum and energy space, $\chi(q', \omega')$, characterizes the probability to find an electron which its final and initial states differing in momentum and energy by q' and ω' , respectively. In other words, it describes the probability of an electron excitation. In Fig. 7.1 we show the real and imaginary parts of the TB polarization function in the absence of impurities. The real part shows that its magnitude decreases, with increasing frequency, for all values of the momentum. The decrease is very fast for large frequencies. On the other hand, the imaginary part decreases dramatically, as the momentum decreases, for $\omega' > 2$ and vanishes for $\omega' \leq 2$.

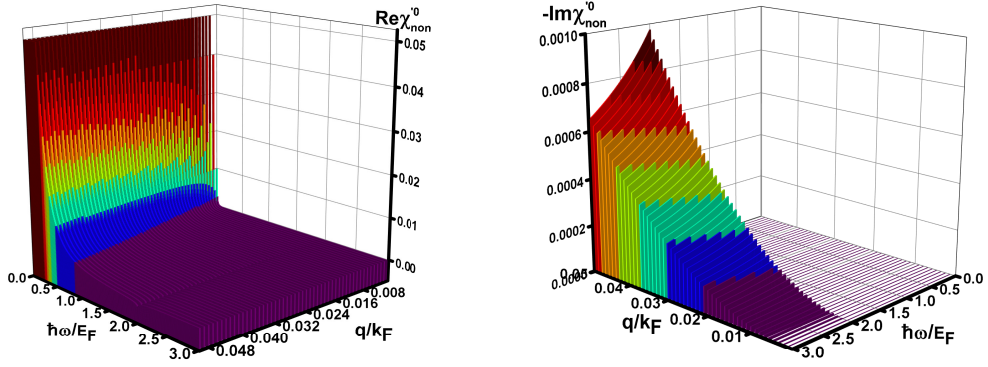


Figure 7.1: Real and imaginary parts of the polarization function $\chi_{non}^{0,TB}$ in the absence of impurities.

We show χ_{non} and χ_{im} as functions of ω' in Fig. 7.2. Actually, Fig. 7.2 shows that the magnitude of the real part of Eq. (7.61), $\Re\chi_{im}$ dominates for almost all ω' except for very small ω' for which the magnitude of $\Re\chi_{non}$ is larger than $\Re\chi_{im}$. Therefore, apart for very small ω' one can obtain all properties of graphene, related to χ , from χ_{im} that has not been considered so far. In addition, as seen in Fig. 7.2, for fixed ω' increasing γ' makes χ_{im} weaker since increasing γ' leads to shorter scattering time and length. Therefore, the probability for an electron to reach the final desired momentum is reduced by strengthening the interaction with impurity.

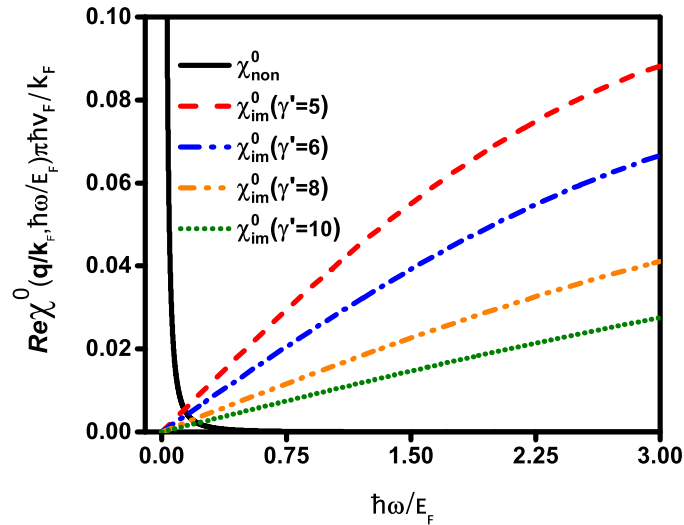


Figure 7.2: Real parts of χ_{non}^0 and χ_{im}^0 versus ω' where χ_{im}^0 is displayed for several γ' .

The real part of the total TB DDRF ($\Re\chi$), containing both χ_{non} and χ_{im} , is shown in Fig. 7.3 (a) versus ω' for a typical value of q' in the long wavelength limit. The solid black curve represents the TB DDRF without inclusion of scattering whereas the coloured curves are for several different γ' . To make clearer its dependence on ω' in Fig. 7.3 (b) we blow up the part of Fig. 7.3 (a) for $\omega' \leq 0.4$. As seen, the TB DDRF for small ω' decreases dramatically because in this energy range the principal contribution to it emanates from χ_{non} as we mentioned in the justification of Fig.7.2.

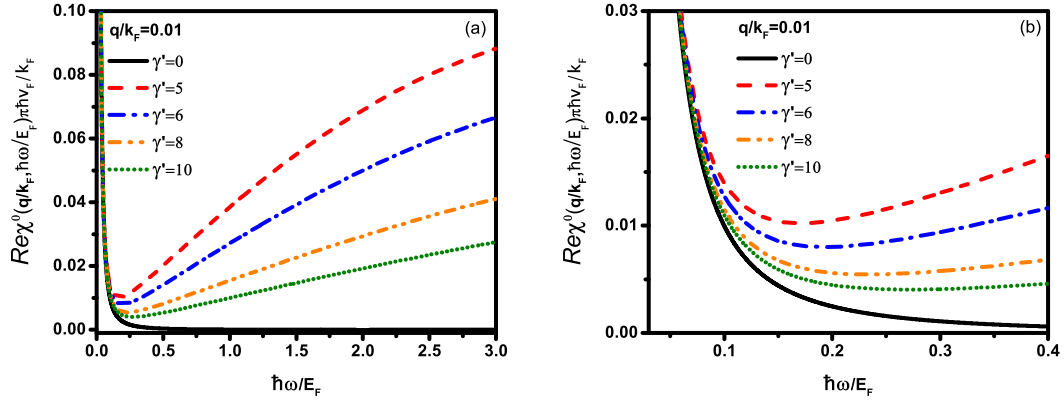


Figure 7.3: (a) Real part of the TB DDRF ($\Re\chi$) for several values of γ' . (b) A part of (a) for $\omega' \leq 0.4$.

The imaginary part of the TB DDRF ($\Im\chi$), versus ω' , is shown in Fig. 7.4 (a) for several γ' . To make more transparent its dependence on ω' , in Fig. 7.4 (b) we show it for three different γ' on an expanded scale. Notice though that this makes the cusps or maxima of Fig. 3(a) invisible.

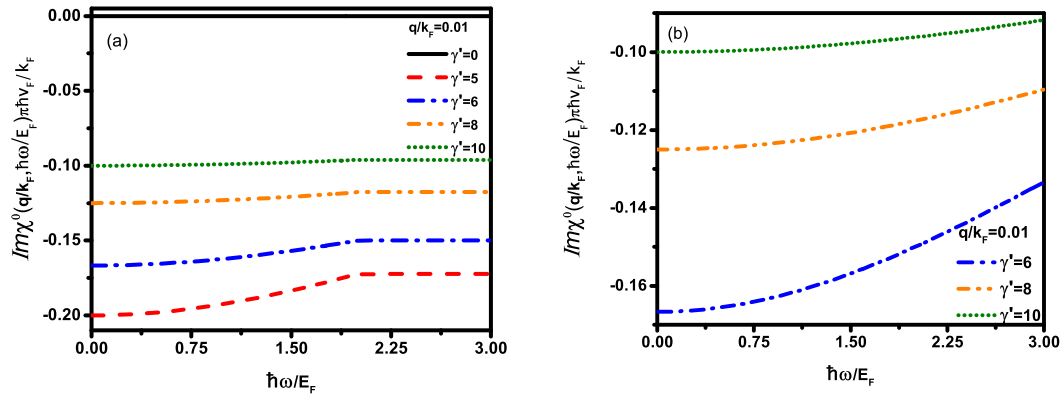


Figure 7.4: (a) Imaginary part of the TB DDRF, $\Im\chi$, for $q' = 0.01$ and several γ' . (b) A segment of $\Im\chi$ for three γ' .

Figures 7.5 (a) and (b) show the real and imaginary parts of the TB DDRF versus q' for several different values of γ' and a typical frequency $\omega' = 0.001$. As shown in 7.5 (a) the dependence of $\Re\chi$ is approximately parabolic because only χ_{non} has a term that contains q' and contributes to the TB DDRF. In addition, it is clear that for q' fixed $\Re\chi$ increases as γ' decreases.

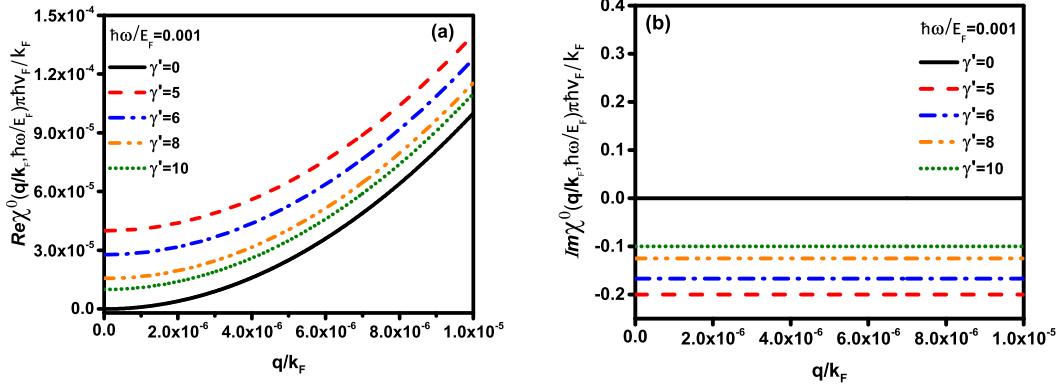


Figure 7.5: (a) Real and (b) imaginary parts of the TB DDRF versus q' at $\omega' = 0.001$ for several different values of γ'

The 3D bar of real and imaginary parts of TB DDRF in the presence of impurity, $\chi_{imp}^{\prime 0, TB}$, are shown in Fig. 7.6. In spite of $\chi_{non}^{\prime 0, TB}$, $\chi_{imp}^{\prime 0, TB}$ does not rely on momentum since γ' has been regarded to be independent that of. Therefore, it has been shown in term of impurity strength and frequency. It is worth to be pointed out that the order of magnitude of $\chi_{imp}^{\prime 0, TB}$ is much larger compared with $\chi_{non}^{\prime 0, TB}$. Consequently we expect that the contribution of $\chi_{imp}^{\prime 0, TB}$ in the total polarization function χ be more than $\chi_{non}^{\prime 0, TB}$. In the Fig. 7.7. for a typical value of impurity, $\gamma' = 5$, 3D bar of χ is depicted. We can see the real part of χ for a typical momentum in small frequency it dramatically decreases and then it increases. On the other hand, its imaginary part increases with frequency for a typical momentum reflecting this fact that for larger frequency the energy dissipation increases.

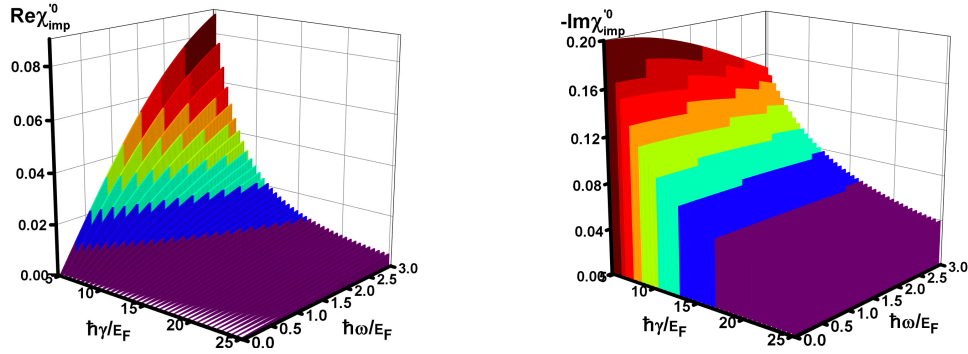
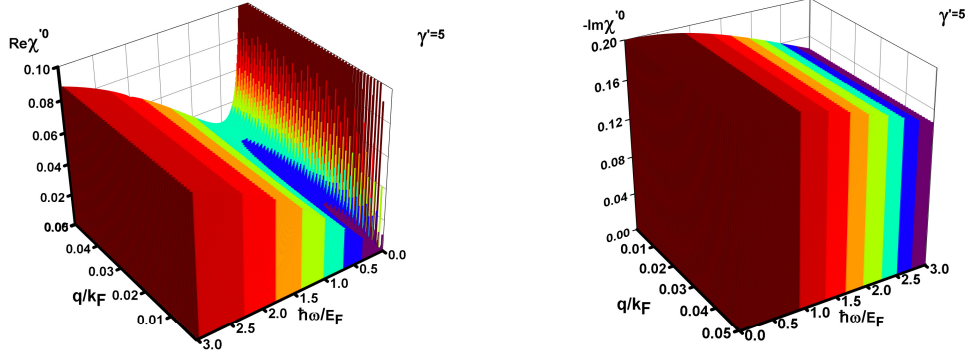
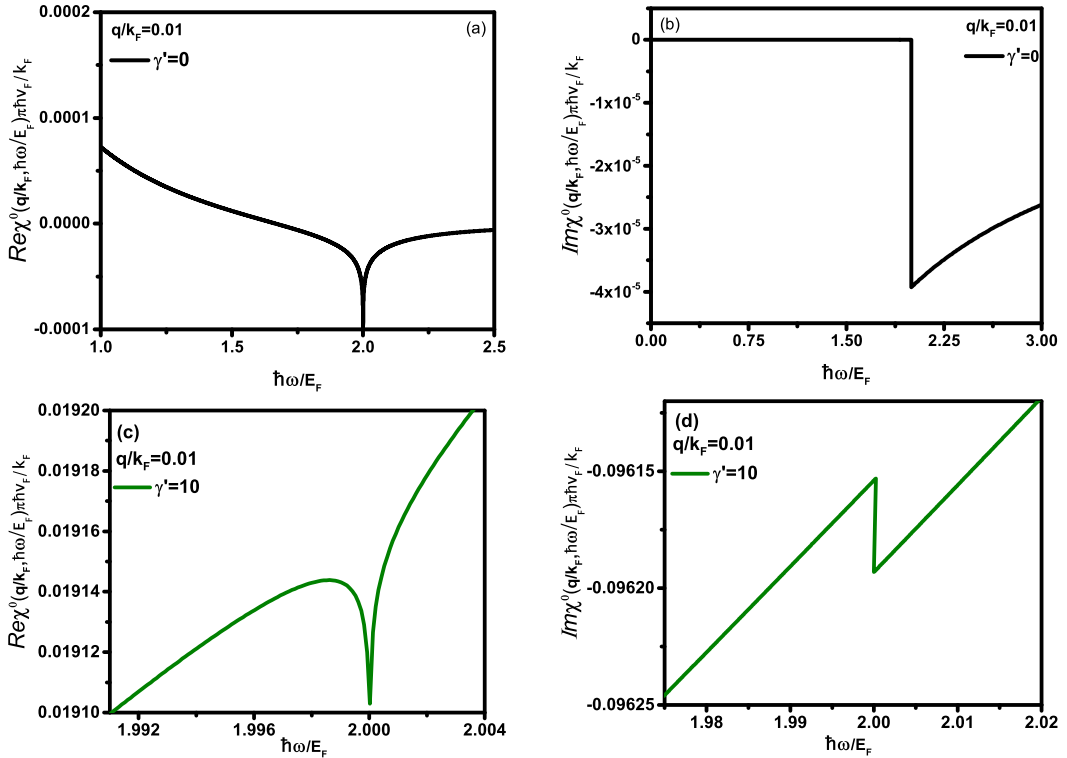


Figure 7.6: Real and imaginary parts of the polarization function $\chi_{imp}^{\prime 0, TB}$ in the presence of impurities.


 Figure 7.7: Real and imaginary parts of χ for $\gamma' = 5$.

Since the logarithmic and step function terms alter the behaviour of $\Re\chi$ and $\Im\chi$, respectively, in the vicinity of $\omega' = 2$, which is not clear in Figs. 7.3 (a) and 7.4 (a) due to the large difference between their values with and without scattering, in Fig. 7.8 we display them separately. The upper panels are for $\gamma' = 0$ and the lower ones for $\gamma' = 10$. Notice i) how including scattering, $\gamma' \neq 0$, strengthens the behaviour of the results without it near $\omega' = 2$ and ii) without scattering ($\gamma' = 0$) $\Im\chi$, shown in Fig. 7.8(b), vanishes for $\omega' \leq 2$ and that there is no dissipation in the system. In contrast, when scattering is included $\Im\chi$ has approximately a constant slope.


 Figure 7.8: (a) Real and (b) imaginary parts of the TB DDRF for $\gamma' = 0$ versus ω' . (c)-(d): as in (a) and (b) for $\gamma' = 10$.

As we mentioned in section 2.3 to find plasmons of a system it suffices to set its permittivity equal to zero. For the RPA we need to employ Eq. (3.56)

$$\epsilon^{RPA}(q, \omega) = 1 - V(q)\chi^0(q, \omega),$$

where $V(q)$ is the 2D Fourier transform of the Coulomb potential. In terms of q' we rewrite $V(q)$ as

$$V(q') = \eta/q', \quad (7.62)$$

with $\eta \equiv 8\alpha\pi^2\hbar c/\epsilon_b k_F$ and ϵ_b the background permittivity. For SB transitions the plasmons can be derived by combining Eqs.(7.56),(7.59), and (3.56). The result is

$$1 - \frac{\beta}{q'} \left[\frac{q'^2}{\omega'^2} + \frac{\omega' (1 - \delta_{\gamma',0})}{2(\omega'^2 + \gamma'^2)} \right] = 0. \quad (7.63)$$

One solution of this quadratic equation is

$$q' = \frac{\omega'^2}{2\beta} \left(1 + \left[1 - \frac{2\beta^2 (1 - \delta_{\gamma',0})}{\omega' (\omega'^2 + \gamma'^2)} \right]^{1/2} \right), \quad (7.64)$$

with $\beta \equiv \eta k_F/\pi\hbar v_F$, gives the dispersion relation. Notice that Eq. (7.63) gives the well-known dispersion $\omega \propto q^{1/2}$ for $\gamma = 0$. The other solution, with $1+$ in Eq. (7.63) replaced by $1-$, is unphysical and therefore rejected.

For TB transitions combining Eqs. (7.57),(7.61), and (3.56) gives the plasmon spectrum as

$$q' = \frac{\omega'}{\beta A(\omega')} \left[1 + \left\{ 1 - \frac{2\beta^2 A(\omega') (1 - \delta_{\gamma',0})}{(\omega'^2 + \gamma'^2)} \right\}^{1/2} \right]. \quad (7.65)$$

Again the second solution for q' , with $1+$ in Eq. (27) replaced by $1-$, is unphysical and rejected. In Figs. 7.9 (a) and 7.10 (a) we show the dispersion relations, resulting from Eqs. (7.64) and (7.65), for several values of γ' . To make these graphs more clear in Figs. 7.9 (b) and 7.10 (b) we show their windows for $0.03 \leq q' \leq 0.05$ and different values of γ' , respectively. In both cases the frequency increases with q' while the momentum plasmon range, i.e., the lower acceptable value of q' , decreases with increasing γ' . Judging from the results as γ increases in Figs. 7.9 and 7.10, we see that the SB plasmon frequency is larger than that the TB one, whereas the SB plasmon momentum range is a bit shorter than the TB one. Note that the plasmon group velocity $\partial\omega/\partial q$ is approximately constant and independent of the scattering strength γ' .

A plasmon is a coherent collective excitation of the charge density with all charges oscillating about their equilibrium positions. Scattering effects, such as electron-impurity or electron-phonon interaction, result in dissipation by single-particle excitations. In other words, a single-particle excitation competes with the collective one: if the mean-free path related to the single-particle excitation is of the order of the wavelength of the collective one, there would be no plasmon. In Figs. 7.9 (b) and 7.10 (b) we can see that there is a critical plasmon momentum below which there is no plasmon spectrum for a typical γ' . This can be explained as follows. The mean-free path decreases with increasing γ' . By the uncertainty principle then its momentum increases with γ' and so does the critical plasmon momentum. Physically, if the wavelength of the collective oscillation, the displacement from equilibrium, is smaller than the mean-free path, the system supports plasmons.

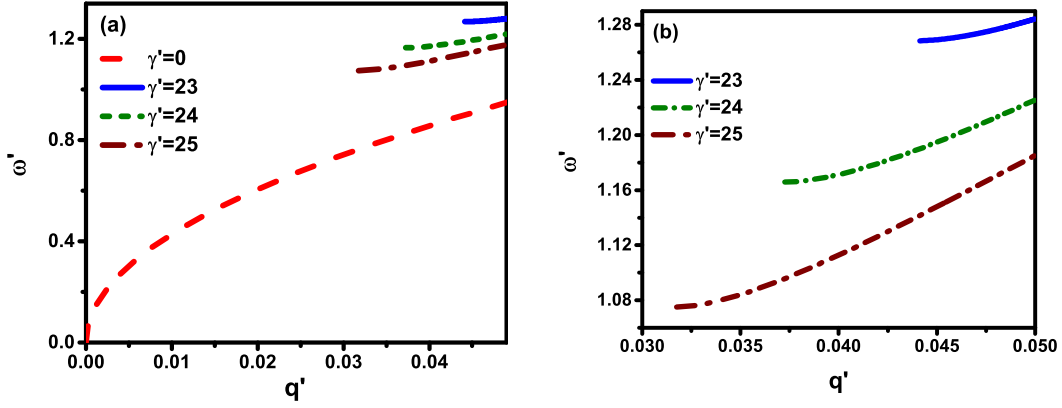


Figure 7.9: (a) SB dispersion relation for several values of γ' . (b) The portion of (a) for $0.03 \leq q' \leq 0.05$.

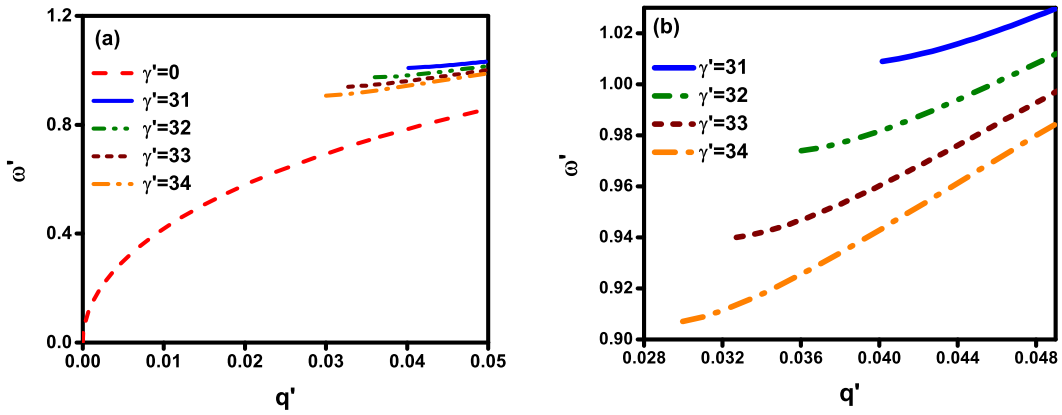


Figure 7.10: (a) TB dispersion relation for several values of γ' . (b) The portion of (a) for $0.028 \leq q' \leq 0.05$.

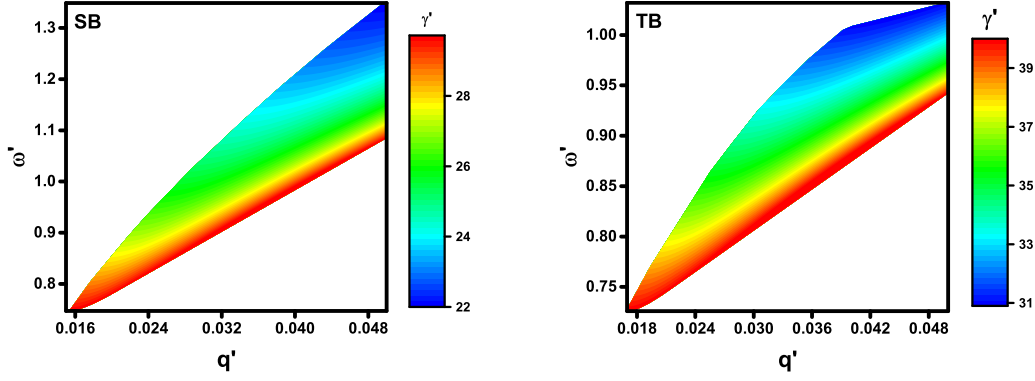
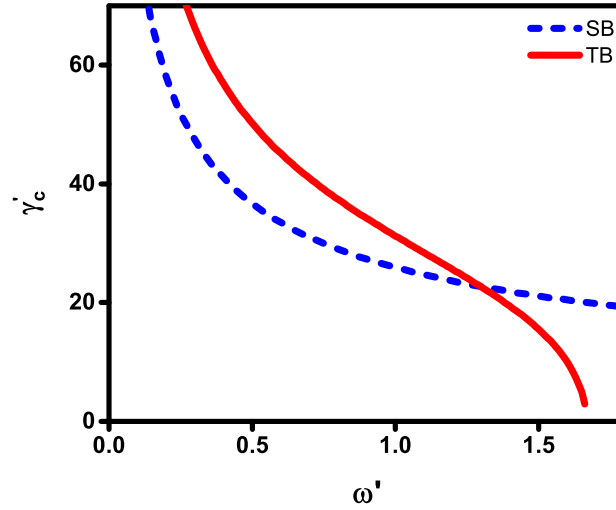
We also see, in both figures, that for fixed plasmon momentum the plasmon frequency increases with decreasing γ' . This can be justified as follows. At fixed plasmon momentum the coherent collective dipole momenta generate the plasmon electromagnetic field (PEM) whose energy is determined by the displacement from the equilibrium positions and the number of available coherent dipole momenta. Higher impurity density, that is larger γ' , increases the elastic scattering probability which reduces the number of coherent dipole momenta. Therefore, the PEM field resulting from them will have lower energy as γ' increases.

As emphasized above, there are critical values γ'_c below which there are no SB or TB plasmons. To find them we set the factors $[\dots]^{1/2}$ and $\{\dots\}^{1/2}$ in Eqs. (7.64) and (7.65), respectively, equal to zero. This gives

$$\gamma'_c{}^{SB} = [2\beta^2/\omega' - \omega'^2]^{1/2}, \quad (7.66)$$

$$\gamma'_c{}^{TB} = [2\beta^2 A(\omega') - \omega'^2]^{1/2}. \quad (7.67)$$

Figure 7.11 shows γ'_c versus the plasmon frequency ω' for SB and TB plasmons. In the former case the high value for low frequencies decreases fast for ω' small but much more slowly for $\omega' > 0.5$, while in the latter its value falls down very fast.


 Figure 7.12: SB and TB plasmon spectra for γ' continuous.

 Figure 7.11: SB and TB critical values γ'_c versus ω' .

It is worth observing that setting $[\dots]^{1/2} = 0$ in Eq. (7.64) leads, for $\gamma \neq 0$ fixed, to a simple cubic equation for ω' , $\omega'^3 + \gamma'^2 \omega' - 2\beta^2 = 0$. Its acceptable solution ω_c is given below in Eq. (7.68). This then can be used to find analytically the lowest limit for $q_c = \omega_c^2/2\beta$, shown in Figs. 7.9 and 7.10, from Eq. (7.64). The explicit results for $\gamma' \geq \gamma'_c$ are

$$\omega_c = [\beta^2 + \sqrt{Z}]^{1/3} + [\beta^2 - \sqrt{Z}]^{1/3}, \quad Z = \beta^4 + \gamma'^6/27. \quad (7.68)$$

Unfortunately, for TB transitions this is not possible due to the factor $A(\omega')$ in Eq. (27).

The plasmon spectrum in Figs. 7.9 and 7.10 involves only a few discrete values of γ' . For a continuous γ' we show it in Fig. 7.12 as a contour plot. Plasmons are not allowed outside the coloured regions. For the same plasmon frequency and momentum, we easily see that the corresponding γ' differ drastically.

7.6 Plasmons in a two-dimensional electron gas

For a two-dimensional electron gas (2DEG) in the long wavelength limit χ_{non}^0 is given by

$$\chi_{non}^0(q', \omega') = \frac{n\hbar^2 k_F^2 q'^2}{mE_F^2 \omega'^2}, \quad (7.69)$$

where n and m are the charge density and electron mass, respectively [41]. As for χ_{im}^0 , with Eqs (3.70) and (7.47) and the assumption that the scattering is elastic and τ independent of the wave vector, we obtain

$$\chi_{im}^0(q', \omega') = \frac{k_F^2}{2\pi E_F} C(\omega', \gamma'). \quad (7.70)$$

In the long wavelength limit the plasmon spectrum can be evaluated by utilizing Eqs. (3.56), (7.69), and (7.70) [91]. The result is similar to graphene's plasmon spectrum, namely,

$$q' = \frac{\omega'^2}{2\beta'} \left(1 + \left[1 - \frac{2\beta'^2 (1 - \delta_{\gamma',0})}{\omega' (\omega'^2 + \gamma'^2)} \right]^{1/2} \right), \quad (7.71)$$

with $\beta' = 4/k_F a_B$ and a_B the Bohr radius. In Fig. 7.13 we show this 2DEG plasmon spectrum in the absence and presence of impurities for various values of β' . To contrast it with that of graphene we give β' in “units” of β . In Fig. 7.13 (a) we can see that for a fixed q' the plasmon energy increases; this can be explained as follows. If the number of plasmon dipole-momenta increases we expect the energy of PEM field to increase as well. Note that in Eq. (7.71) the plasmon momentum is inversely proportional to β' . In addition, k_F in a 2DEG is proportional to the square root of the electron density, $k_F = \sqrt{2\pi n}$. Then one finds that the plasmon momentum q' is likewise proportional to \sqrt{n} . In contrast, in graphene the dimensionless plasmon momentum is independent of the electron density n . In Fig. 7.13 we show the plasmon dispersion in a 2DEG in (a) the absence and (b) the presence of impurity scattering; in (b) we took $\gamma' = 25$. It can be seen that for fixed plasmon momentum and decreasing β' the plasmon energy decreases due to the reduction of the plasmon dipole momenta. Furthermore, compared to the graphene case $\beta' = \beta$, we can see that for the lower value of β' the critical plasmon momentum becomes smaller due to the fact that scattering by impurities weakens with decreasing electron density.

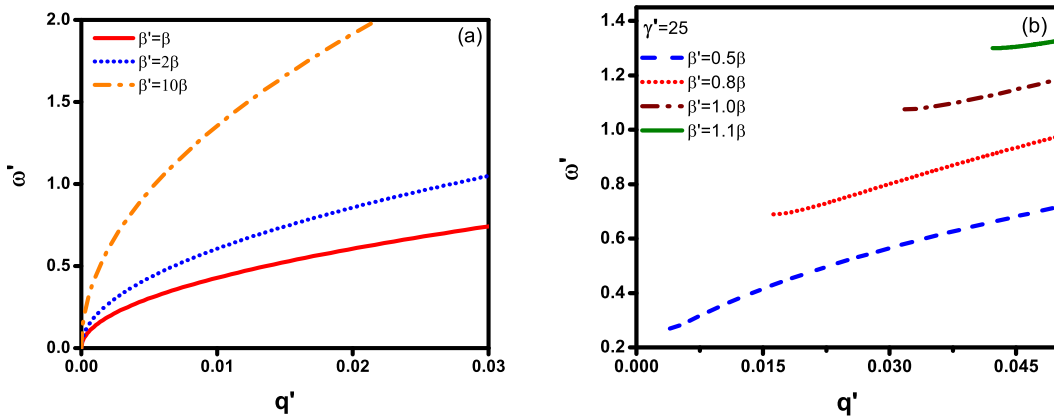


Figure 7.13: 2DEG plasmon dispersion (a) in the absence and (b) presence of impurity scattering. In (b) $\gamma' = 25$ is used.

Further, as in the case of graphene, in a 2DEG the critical γ' , below which no plasmons are allowed, is obtained in the same way. It is given by

$$\gamma_c'^{2DEG} = [2\beta'^2/\omega' - \omega'^2]^{1/2}. \quad (7.72)$$

We show it in Fig. 7.14 $\gamma_c'^{2DEG}$ for several values of β' . It can be seen that for fixed ω' and increasing β' the value of γ_c' increases as well. We further remark that, similar to graphene for SB transitions, with $\gamma_c' \neq 0$ fixed Eq. (33) allows an analytic evaluation of the allowed ω' which in turn determines the lower value of q' below which no plasmons are allowed. One simply has to replace β with β' in Eq. (7.68) to obtain the corresponding ω_c and q_c .

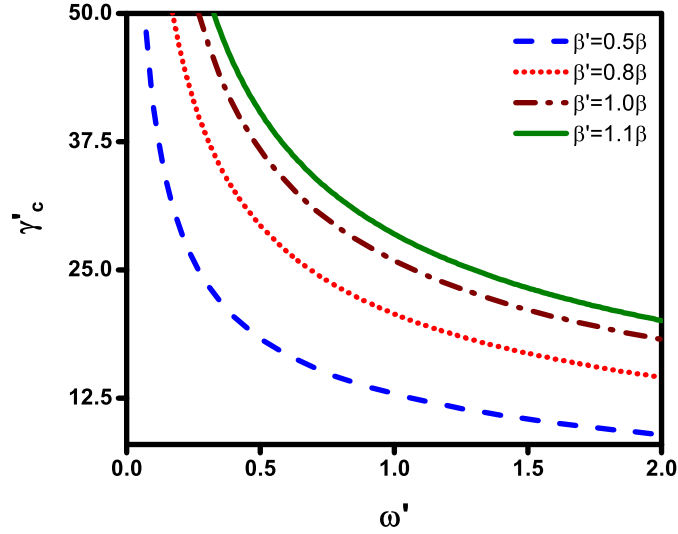


Figure 7.14: $\gamma_c'^{2DEG}$ versus ω' for several values of β' .

7.7 Single- and two-band TM SP

The poles of the transmission or reflection coefficients of graphene give the SPs which for TM modes is given by

$$q = \frac{i\omega\epsilon_0(n_1^2 + n_2^2)}{\sigma(q, \omega)}. \quad (7.73)$$

It should be pointed out that similar to section 6.4 Eq. (7.73) is valid only for SP momenta much larger than that of light, $q \gg \omega/c$. The simplest approximation on which we focus here is the Lindhard one that neglects the effects of Coulomb interaction and local field factor. Because the polarization function has different values for SB and TB transitions, the SPs would be different in each of them. Note that real part of the transmission pole yields an SP mode [45, 90] and its imaginary part is responsible for dissipation. For SB transitions Eqs. (7.56), (7.59), (3.59), and (7.73) give

$$q'^2 - q'\beta''\omega'^2 + \frac{\omega'^3(1 - \delta_{\gamma',0})}{2(\omega'^2 + \gamma'^2)} = 0 \quad (7.74)$$

with $\beta'' = v_F(n_1^2 + n_2^2)/4\alpha c$. The physical solution is given by

$$q' = \frac{1}{2} \left[\beta''\omega'^2 + \left[(\beta''\omega'^2)^2 - \frac{2\omega'^3(1 - \delta_{\gamma',0})}{\omega'^2 + \gamma'^2} \right]^{1/2} \right]. \quad (7.75)$$

For TB using Eqs. (7.57), (7.61), (3.59), and (7.73) we obtain the physical solution as

$$q' = \frac{\omega' \beta''}{A(\omega')} \left(1 + \left[1 - \frac{2A(\omega')}{\beta''^2} \left(\frac{1 - \delta_{\gamma',0}}{\omega'^2 + \gamma'^2} \right) \right]^{1/2} \right). \quad (7.76)$$

Notice that there are other solutions for Eqs. (7.75) and (7.76) with the plus sign in front of the square root $+[\dots]^{1/2}$ replaced by a negative sing. However, these solutions are unphysical therefore they have been rejected. Here in our calculation n_1 and n_2 have been considered to be 1 and 2 respectively. In Figs. 7.15 (a) and 7.16 (a) the TM SP spectrum of SB and TB for several values of γ' are shown. To make the behavior of graphs more clear in Figs. 7.15 (b) and 7.16 (b) we show them in a smaller windows of q' . To show how the domain of SPs alter by the value of impurity. As seen with decreasing γ' the acceptable value of q' increases where that of SB is smaller than TB. Furthermore, the SP frequency in TB is larger than SB for a typical allowed value of q' . In both cases the group velocity $\partial\omega/\partial q$ is approximately constant and independent of the impurity strength. As seen, the SP dispersion changes when the strength γ' is varied. This can be explained as follows. A coherent ensemble of dipole moments oscillating about their equilibrium configuration, under a phase matching condition, starts to generate evanescent electromagnetic field that propagates at the interface of metallic-dielectric media. Damping effects due to defects, impurities, or electron-phonon interaction are expected to reduce the effective number of these coherent dipole moments. In other words, a higher value of γ' increases the probability of scattering and reduces the number of coherent dipole moments. Therefore, the energy of an electromagnetic field originated from an ensemble of dipole moments for lower γ' , with the same momentum, is larger than that for higher γ' .

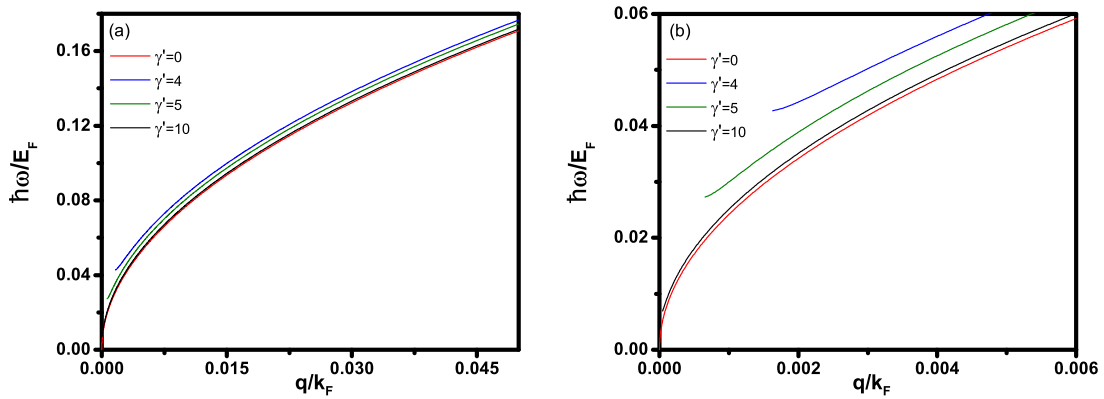


Figure 7.15: (a) SB TM SP for different values of γ' . (b) The segment of (a) for $q' \leq 0.006$.

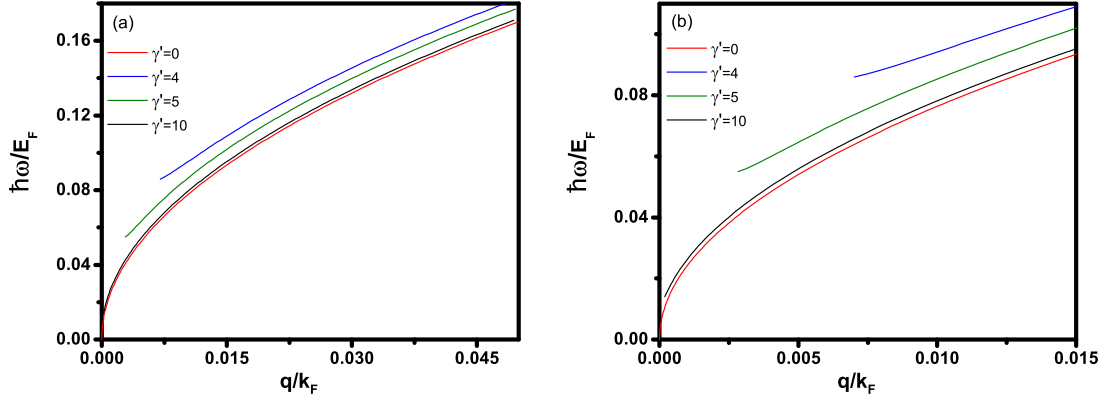


Figure 7.16: (a) TB TM SP for different values of γ' . (b) The segment of (a) for $q' \leq 0.015$.

In Figs. 7.17 and 7.18 we show the 3D TM SP spectrum and (ω', γ') contour plot of SB and TB respectively. As seen, for a fixed γ' by increasing SP frequency its momentum increases as well. The bars in these figures indicate the allowed values in a region where SPs exist. It can be seen, in particular in Figs. 7.15 and 7.16, that below a critical value of γ' , called γ'_c , no SPs exist. This critical strength γ'_c can be determined by setting to zero the quantities $[..]^{1/2}$ in Eqs. (7.75) and (7.76). The results are

$$\gamma_c'^{SB} = [2/\beta'^2 \omega' - \omega'^2]^{1/2}, \quad (7.77)$$

$$\gamma_c'^{TB} = [2A(\omega')/\beta'^2 - \omega'^2]^{1/2}. \quad (7.78)$$

The strength γ'_c , versus the SP frequency ω' is shown in Fig. 7.19 for the SB and TB cases. In both γ'_c decreases very fast with increasing SP frequency. In addition, for fixed frequency γ'_c is smaller in the SB case.

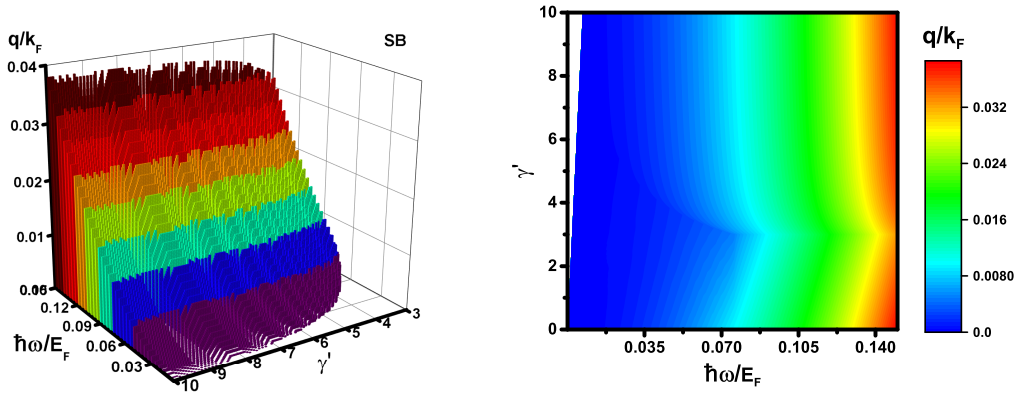


Figure 7.17: 3D bar and (γ', ω') contour plot of TM SB SPs.

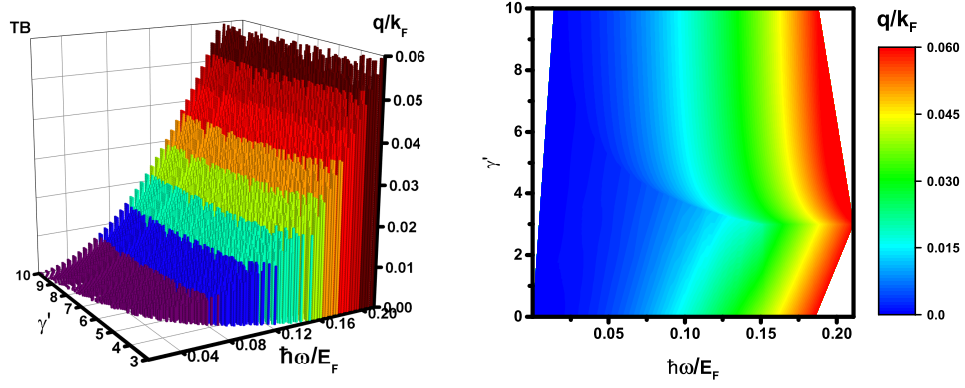
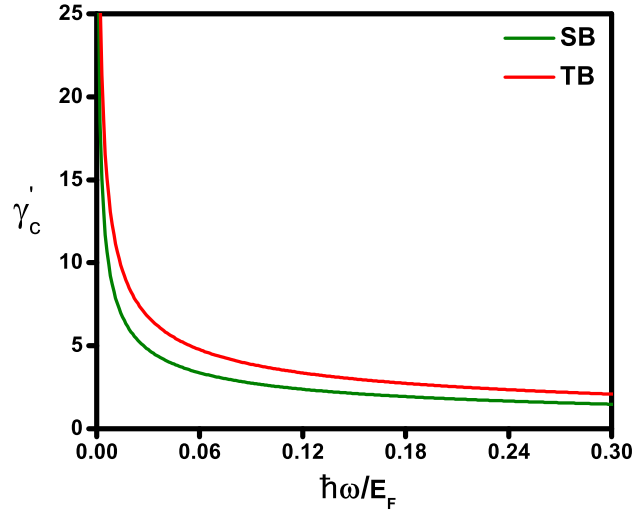

 Figure 7.18: 3D bar and (γ', ω') contour plot of TM TB SPs.


Figure 7.19: Critical impurity strength versus SP frequency.

7.8 Quality factor

To efficiently transport high-speed information and energy, devices must have the least possible number of obstacles or defects, e.g. impurities, so that the energy dissipation is the lowest. Devices with the best functionality are usually distinguished by the quality factor (QF) defined as the ratio of the stored to the dissipated energy. The devices with higher the QF higher have higher functionality and performance [92]. The QF is given by

$$Q = \frac{U_{stor}}{U_{dis}} = \frac{U_0 - U_{dis}}{U_{dis}} = \frac{U_0}{U_{dis}} - 1, \quad (7.79)$$

where U_{stor} , U_{dis} and U_0 refer to the stored, dissipated, and total energy densities, respectively. Here U_0 is the energy density of the incoming field, $U_0 = \epsilon_0 |E_I|^2 / 2$. The dissipated energy of the SP, U_{dis} , is

$$U_{dis} = \frac{1}{2} \epsilon_0 |E_{dis}|^2 = \frac{1}{2} \epsilon_0 |E_I|^2 |\Im t(q'_{sp}, \omega'_{sp})|^2, \quad (7.80)$$

where $\Im t(q'_{sp}, \omega'_{sp})$ is the imaginary part of the transmission coefficient at the surface plasmon momentum and frequency. For SB and TB transitions we obtain

$$Q_{SB} = [\eta \Im C(\omega', \gamma') / 2k'_{sp}]^2 - 1, \quad (7.81)$$

$$Q_{TB} = [\eta D(\omega'_{sp}, \gamma') / 2k'_{sp}]^2 - 1, \quad (7.82)$$

with

$$D(\omega', \gamma') = \Im C(\omega', \gamma') + (\pi q'^2_{sp} / 4\omega') \Theta(\omega' - 2), \quad (7.83)$$

and $\eta = 4\alpha c / (v_F n_1 n_2)$. For low SP frequency by combining Eqs. (7.75) and (7.81) for SB and Eqs. (7.76) and (7.82) for TB, respectively, it can be shown that QF is

$$Q \propto \alpha^2 \lambda_{sp}^2 / \gamma'^2, \quad (7.84)$$

which depends only on fine-structure, SP wavelength, and impurity strength. In Figs.7.20 (a) and (b) QF of SB and TB TM SPs versus SP frequency for several values of γ' are shown. As seen, by increasing SP frequency QF decreases dramatically. In addition, for a fixed SP frequency in both cases by increasing the impurity strength QF decreases which is expected since impurity with higher value implying more loss and dissipation. In low frequency according to Eqs. (7.75) and (7.76) SP wavelength is proportional to ω^{-2} , as seen in Figs.7.20 in both cases, SB and TB, QF decreases with the power of ω^{-4} in this regime. Due to the fact that, dissipation in TB is more than SB regarding to (7.59) and (7.61) we expect that QF in SB be more than SB as it is conspicuous here.

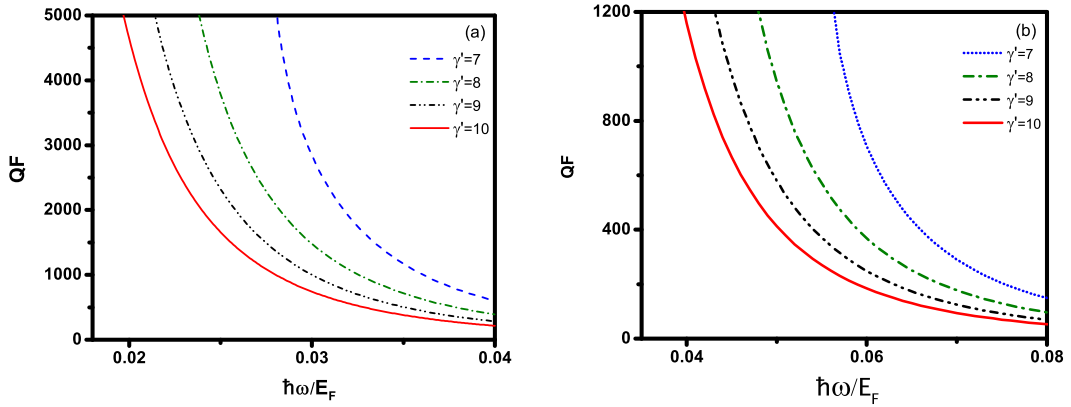


Figure 7.20: (a) SB and (b) TB TM SPs QF versus SP frequency for several values of γ' .

7.9 Single- and two-band TE SP

Similar to the case of TM SPs, the transmission amplitude for TE SPs, see Eq. (6.30), is given by

$$t(k, \omega) = 2 \left[1 + \frac{n_2 \sin \theta_T}{n_1 \sin \theta_I} + \frac{\sigma(k, \omega)}{n_1 \epsilon_0 c \sin \theta_I} \right]^{-1}. \quad (7.85)$$

Corresponding to Eq.(7.73) for TE SPs we find

$$k = \frac{i\sigma(k, \omega)\omega}{2\epsilon_0 c^2}. \quad (7.86)$$

In the SB case there are no TE SPs as in the absence of scattering [93]. In the TB one corresponding to Eq.(7.74) we obtain

$$q'^3 + aq'^2 + b = 0, \quad (7.87)$$

with $a = 2\alpha c\omega' A(\omega')/v_F$, $b = 4\alpha c\omega'^2 \Re C(\omega', \gamma')/v_F$. Eq. (7.87) has a real solution with negative value for q' which is not physical. Accordingly, we infer that impurity scattering suppresses TE SPs in graphene.

8 Quantum Boltzmann equation

8.1 Introduction

In the previous chapters, we dealt with QLRT to investigate dynamical transport and optical properties of inhomogeneous systems. For instance, we treated plasmonics properties of AGNRs and graphene by regarding many-body effects such as exchange-hole effect, electron-phonon, and the Coulomb potential to name a few. Here we employ quantum Boltzmann equation (QBE) in the Van Hove limit with the same Hamiltonian of Eq. (7.24) to study transport properties of a homogeneous system via considering many-body effects such as electron-electron interaction [94]

$$\begin{aligned} & \frac{\partial \langle c_{\zeta'}^\dagger c_{\zeta''} \rangle_t}{\partial t} - F(t) \frac{1 - e^{-\beta(E_{\zeta'} - E_{\zeta''})}}{E_{\zeta'} - E_{\zeta''}} \langle n_{\zeta''} \rangle_{eq} (1 - \langle n_{\zeta'} \rangle_{eq}) \langle \zeta'' | \dot{a} | \zeta' \rangle + \frac{i}{\hbar} (E_{\zeta''} - E_{\zeta'}) \langle c_{\zeta'}^\dagger c_{\zeta''} \rangle_t \\ & + \beta F(t) \sum_{\zeta_1 \zeta_2 \zeta_3} Q(\zeta_3 \zeta; \zeta_2 \zeta_1) \langle n_{\zeta_3} n_{\zeta} (1 - n_{\zeta_2}) (1 - n_{\zeta_1}) \rangle_{eq} (a_{\zeta_3} + a_{\zeta} - a_{\zeta_2} - a_{\zeta_1}) \delta_{\zeta' \zeta''} \\ & = - \sum_{\zeta_1 \zeta_2 \zeta_3} Q(\zeta_3 \zeta; \zeta_2 \zeta_1) \langle n_{\zeta_3} n_{\zeta} (1 - n_{\zeta_2}) (1 - n_{\zeta_1}) - (1 - n_{\zeta_3}) (1 - n_{\zeta}) n_{\zeta_2} n_{\zeta_1} \rangle_t \delta_{\zeta' \zeta''}, \quad (8.1) \end{aligned}$$

with $\langle \zeta | a | \zeta \rangle$ being the expectation value of the position operator and $\beta = 1/k_B T$. Here a and A in Eq. (7.24) are related by $A = \sum_i a_i$. The Q in Eq. (8.1) is the transition probability per unit time given by

$$Q(\zeta_3 \zeta; \zeta_2 \zeta_1) = \lambda^2 \frac{2\pi}{\hbar} |\langle \zeta_3 \zeta | v | \zeta_2 \zeta_1 \rangle|^2 \delta(E_{\zeta_3} + E_{\zeta} - E_{\zeta_2} - E_{\zeta_1}), \quad (8.2)$$

where v is the interaction. The Delta function in Eq. (8.2) is added manually to satisfy energy conservation. The conductivity of system can be evaluated by current operator which, for $\omega = 0$, direct current (DC), results in

$$\begin{aligned} \sigma_{\mu\nu}^d &= \frac{\beta e^2}{V} \sum_{klmi} Q(m, i; l, k) \langle n_m n_i (1 - n_l) (1 - n_k) \rangle_{eq} \\ & \quad \times (a_{\nu m} + a_{\nu i} - a_{\nu l} - a_{\nu k}) a_{\mu i}, \quad (8.3) \end{aligned}$$

$$\sigma_{\mu\nu}^{nd} = \frac{ie^2 \hbar}{V} \sum_{i \neq i'} \langle n_i \rangle_{eq} (1 - \langle n_{i'} \rangle_{eq}) \langle i | v_\nu | i' \rangle \langle i' | v_\mu | i \rangle \frac{1 - e^{-\beta(E_{i'} - E_i)}}{(E_{i'} - E_i)^2}, \quad (8.4)$$

where e and V stand for the electron charge and system volume. The superscripts “ d ” and “ nd ” in Eqs. (8.3) and (8.4) refer to diagonal and non-diagonal parts respectively. This stems from the approach used in representation of an operator like A

$$\begin{aligned}
 A &= \sum_{ij} |i\rangle \langle i| A |j\rangle \langle j| \\
 &= \sum_i |i\rangle \langle i| A |i\rangle \langle i| + \sum_{i \neq j} |i\rangle \langle i| A |j\rangle \langle j| \\
 &= \mathbb{P}A + (1 - \mathbb{P})A \equiv A^d + A^{nd},
 \end{aligned} \tag{8.5}$$

where \mathbb{P} is the projection operator. For more details see Ref. [51]. Therefore, the general expression for dc conductivity by considering electron-electron interaction is given by $\sigma_{\mu\nu} = \sigma_{\mu\nu}^d + \sigma_{\mu\nu}^{nd}$ with $\mu, \nu = x, y, z$.

8.2 dc conductivity of graphene in presence of electron-electron interaction

In this section, as an example of the application of QBE, we evaluate the dc conductivity of graphene via considering the electron-electron interaction. For the sake of the simplicity, we assume that the external applied electric field is in the x direction, $\vec{E} = E_x \hat{e}_x$. For the diagonal part Eq. (8.3) becomes [94]

$$\sigma_{xx}^d = \frac{\beta e^2}{4V} \sum_{klmi} Q(m, i; l, k) f_m f_i (1 - f_l)(1 - f_k) (a_{xk} + a_{xl} - a_{xm} - a_{xi})^2, \tag{8.6}$$

where f is the Fermi-Dirac distribution. In the derivation of Eq. (8.6), we have exploited

$$\begin{aligned}
 \langle n_m n_i (1 - n_l)(1 - n_k) \rangle_{eq} &= \langle n_m \rangle_{eq} \langle n_i \rangle_{eq} (1 - \langle n_l \rangle_{eq})(1 - \langle n_k \rangle_{eq}) \\
 &= f_m f_i (1 - f_l)(1 - f_k).
 \end{aligned}$$

Graphene eigenvalues and eigenfunctions are given by

$$\langle \vec{r} | \vec{k} \zeta s \rangle = \frac{e^{i\vec{k}\vec{r}}}{\sqrt{4A}} \begin{pmatrix} e^{-i\theta(\vec{k})} \\ \zeta \\ e^{i\theta(\vec{k})} \\ \zeta \end{pmatrix} X_s, \quad E_{\zeta s}(\vec{k}) = \zeta \hbar v_F |\vec{k}|, \quad \zeta = \pm 1, \tag{8.7}$$

with $\theta(\vec{k}) = \tan^{-1}(k_y/k_x)$. Here X and $\zeta = \pm 1$ refer to spin part of the eigenfunction, valence, and conduction bands respectively. Therefore, Eq. (8.6) leads to

$$\begin{aligned}
 \sigma_{xx}^d &= \frac{\beta e^2}{4A} \sum_{\vec{k}_1 \zeta_1 s_1} \sum_{\vec{k}_2 \zeta_2 s_2} \sum_{\vec{k}_3 \zeta_3 s_3} \sum_{\vec{k}_4 \zeta_4 s_4} Q(\vec{k}_1 \zeta_1 s_1, \vec{k}_2 \zeta_2 s_2; \vec{k}_3 \zeta_3 s_3, \vec{k}_4 \zeta_4 s_4) \\
 &\quad \times f_{\vec{k}_1 \zeta_1 s_1} f_{\vec{k}_2 \zeta_2 s_2} (1 - f_{\vec{k}_3 \zeta_3 s_3})(1 - f_{\vec{k}_4 \zeta_4 s_4}) (a_{x\vec{k}_4 \zeta_4 s_4} + a_{x\vec{k}_3 \zeta_3 s_3} - a_{x\vec{k}_1 \zeta_1 s_1} - a_{x\vec{k}_2 \zeta_2 s_2})^2,
 \end{aligned} \tag{8.8}$$

with

$$Q(\vec{k}_1 \zeta_1 s_1, \vec{k}_2 \zeta_2 s_2; \vec{k}_3 \zeta_3 s_3, \vec{k}_4 \zeta_4 s_4) = \frac{2\pi}{\hbar} I_{comb}^2 \delta(E_{\vec{k}_1 \zeta_1 s_1} + E_{\vec{k}_2 \zeta_2 s_2} - E_{\vec{k}_3 \zeta_3 s_3} - E_{\vec{k}_4 \zeta_4 s_4}),$$

where I_{comb} is

$$I_{comb} \equiv \langle \vec{k}_1 \zeta_1 s_1, \vec{k}_2 \zeta_2 s_2 | v | \vec{k}_3 \zeta_3 s_3, \vec{k}_4 \zeta_4 s_4 \rangle. \quad (8.9)$$

For the sake of simplicity, we first deal with I_{comb} . The Coulomb potential is written in terms of its Fourier transform

$$v(\vec{r} - \vec{r}') = \sum_{\vec{q}} \frac{e^{i\vec{q} \cdot (\vec{r} - \vec{r}')}}{\sqrt{q^2 + k_s^2}}, \quad (8.10)$$

where k_s is the screening strength. Eq. (8.9) becomes

$$I_{comb} = \frac{1}{(4A)^2} \int \int d\vec{r} d\vec{r}' \begin{pmatrix} e^{-i\theta(\vec{k}_1)} \\ \zeta_1 \\ e^{i\theta(\vec{k}_1)} \\ \zeta_1 \end{pmatrix}^\dagger \begin{pmatrix} e^{-i\theta(\vec{k}_3)} \\ \zeta_3 \\ e^{i\theta(\vec{k}_3)} \\ \zeta_3 \end{pmatrix} e^{i\vec{r} \cdot (\vec{k}_3 - \vec{k}_1)} \\ \begin{pmatrix} e^{-i\theta(\vec{k}_2)} \\ \zeta_2 \\ e^{i\theta(\vec{k}_2)} \\ \zeta_2 \end{pmatrix}^\dagger \begin{pmatrix} e^{-i\theta(\vec{k}_4)} \\ \zeta_4 \\ e^{i\theta(\vec{k}_4)} \\ \zeta_4 \end{pmatrix} e^{i\vec{r}' \cdot (\vec{k}_4 - \vec{k}_2)} \underbrace{X_{s_1}^\dagger X_{s_3}}_{\delta_{s_1 s_3}} \underbrace{X_{s_2}^\dagger X_{s_4}}_{\delta_{s_2 s_4}} \sum_{\vec{q}} \frac{e^{i\vec{q} \cdot (\vec{r} - \vec{r}')}}{\sqrt{q^2 + k_s^2}} \quad (8.11)$$

which, by some simplifications, leads to

$$I_{comb} = \frac{1}{4} \sum_{\vec{q}} \frac{\delta_{s_1 s_3} \delta_{s_2 s_4}}{\sqrt{q^2 + k_s^2}} \left[\cos[\theta(\vec{k}_1) - \theta(\vec{k}_3)] + \zeta_1 \zeta_3 \right] \left[\cos[\theta(\vec{k}_2) - \theta(\vec{k}_4)] + \zeta_2 \zeta_4 \right] \\ \underbrace{\frac{1}{A} \int d\vec{r} e^{i\vec{r} \cdot (\vec{k}_3 - \vec{k}_1 + \vec{q})}}_{\delta_{\vec{k}_1 - \vec{k}_3, \vec{q}}} \underbrace{\frac{1}{A} \int d\vec{r}' e^{i\vec{r}' \cdot (\vec{k}_4 - \vec{k}_2 - \vec{q})}}_{\delta_{\vec{k}_4 - \vec{k}_2, \vec{q}}}, \quad (8.12)$$

resulting in

$$I_{comb} \equiv \frac{1}{4} \frac{\delta_{s_1 s_3} \delta_{s_2 s_4} \delta_{\vec{k}_1 - \vec{k}_3, \vec{k}_4 - \vec{k}_2}}{\sqrt{g(\vec{k}_1, \vec{k}_3)^2 + k_s^2}} O(\vec{k}_1 \zeta_1, \vec{k}_2 \zeta_2; \vec{k}_3 \zeta_3, \vec{k}_4 \zeta_4), \quad (8.13)$$

with

$$g(\vec{k}_1, \vec{k}_3) \equiv |\vec{k}_1 - \vec{k}_3|,$$

and

$$O(\vec{k}_1 \zeta_1, \vec{k}_2 \zeta_2; \vec{k}_3 \zeta_3, \vec{k}_4 \zeta_4) \equiv \left[\cos[\theta(\vec{k}_1) - \theta(\vec{k}_3)] + \zeta_2 \zeta_4 \right] \left[\cos[\theta(\vec{k}_2) - \theta(\vec{k}_4)] + \zeta_2 \zeta_4 \right].$$

For the sake of the simplicity, we only consider the conduction band, $\zeta_1 = \zeta_2 = \zeta_3 = \zeta_4 = +1$. Finally, Eq. (8.8) becomes

$$\sigma_{xx}^d = \frac{\beta e^2}{4A} \sum_{\vec{k}_1 \vec{k}_2} \sum_{\vec{k}_3 \vec{k}_4} \sum_{s_1 s_2 s_3 s_4} \frac{2\pi}{\hbar} \frac{\delta_{s_1 s_3} \delta_{s_2 s_4}}{|g(\vec{k}_1, \vec{k}_3)|^2 + k_s^2} \frac{1}{4^2} O^2(\vec{k}_1 \zeta_1, \vec{k}_2 \zeta_2; \vec{k}_3 \zeta_3, \vec{k}_4 \zeta_4)$$

$$\begin{aligned} & \times f_{\vec{k}_1 s_1} f_{\vec{k}_2 s_2} (1 - f_{\vec{k}_3 s_3}) (1 - f_{\vec{k}_4 s_4}) (a_{x\vec{k}_4 s_4} + a_{x\vec{k}_3 s_3} - a_{x\vec{k}_1 s_1} - a_{x\vec{k}_2 s_2})^2 \\ & \times \delta(E_{\vec{k}_1 \zeta_1 s_1} + E_{\vec{k}_2 \zeta_2 s_2} - E_{\vec{k}_3 \zeta_3 s_3} - E_{\vec{k}_4 \zeta_4 s_4}) \delta_{\vec{k}_1 - \vec{k}_3, \vec{k}_4 - \vec{k}_2}. \end{aligned} \quad (8.14)$$

The production of the delta function and Kronecker delta in the above equation states the conservation of energy and momentum. In general, $g(\vec{k}_1, \vec{k}_3)$ is a constant. In the case that $g(\vec{k}_1, \vec{k}_3) \rightarrow 0$, for the sake of simplicity, we assume $g(\vec{k}_1, \vec{k}_3) = 0$. This implies that the conductivity is non-vanishing if and only if $\vec{k}_1 = \vec{k}_3$, $\vec{k}_4 = \vec{k}_2$ or $\vec{k}_1 = -\vec{k}_2$, $\vec{k}_4 = -\vec{k}_3$. After some algebra and using the following identity

$$\beta f_i (1 - f_i) = \delta(E_i - E_F), \quad (8.15)$$

we arrive at

$$\sigma_{xx}^d = \frac{2\pi e^2}{A^3 \hbar} \frac{4\Delta x^2}{k_s^2} \sum_{\vec{k}_1 \vec{k}_2} \delta(E(\vec{k}_1) - E_F) f_{\vec{k}_2} (1 - f_{\vec{k}_2}), \quad (8.16)$$

with $\Delta x = (a_{x\vec{k}_1} - a_{x\vec{k}_2})$. Since $a_{x, \vec{k} \zeta s}$ vanishes, we use the following approximation $\Delta x = l_\tau$ where l_τ is the mean-free distance. From the physical point of view, the average distance between electron scatterings which result in changing the momentum of electrons is the mean-free distance. Converting the sum into an integral gives rise to

$$\begin{aligned} \sigma_{xx}^d &= \frac{2\pi e^2}{A^3 \hbar} \frac{4l_\tau^2}{k_s^2} \frac{A^2}{(2\pi)^4} \int_0^{2\pi} d\theta_2 \int_0^{2\pi} d\theta_1 \int_0^{k_F} k_1 dk_1 \delta(k_1 - k_F) \\ & \times \int_0^{k_F} \frac{k_2 e^{\beta \hbar (k_2 - k_F)}}{[1 + e^{\beta \hbar (k_2 - k_F)}]^2} dk_2. \end{aligned} \quad (8.17)$$

After some algebra, we obtain

$$\sigma_{xx}^d = \frac{e^2}{A \hbar} \frac{4l_\tau^2}{k_s^2} \frac{k_F}{2\pi} \int_0^{k_F} \frac{k e^{\beta \hbar (k - k_F)}}{[1 + e^{\beta \hbar (k - k_F)}]^2} dk. \quad (8.18)$$

The integral in the above equation can be evaluated in the following way:

$$\begin{aligned} II &= \int_0^{k_F} \frac{(k - k_F + k_F) e^{\beta \hbar (k - k_F)}}{[1 + e^{\beta \hbar (k - k_F)}]^2} dk = k_F \int_0^{k_F} \frac{e^{\beta \hbar (k - k_F)}}{[1 + e^{\beta \hbar (k - k_F)}]^2} dk + \\ & \int_0^{k_F} \frac{(k - k_F) e^{\beta \hbar (k - k_F)}}{[1 + e^{\beta \hbar (k - k_F)}]^2} dk, \end{aligned} \quad (8.19)$$

where the first term results in

$$k_F \int_0^{k_F} \frac{e^{\beta \hbar (k - k_F)}}{[1 + e^{\beta \hbar (k - k_F)}]^2} dk = \frac{k_F}{\beta \hbar} \left[\frac{1}{1 + e^{-\beta \hbar k_F}} - \frac{1}{2} \right],$$

and the second term

$$\int_0^{k_F} \frac{(k - k_F) e^{\beta \hbar (k - k_F)}}{[1 + e^{\beta \hbar (k - k_F)}]^2} dk = \frac{1}{(\beta \hbar)^2} \int_{-\beta \hbar k_F}^0 \frac{x e^x dx}{(1 + e^x)^2} = \frac{1}{(\beta \hbar)^2} \left[\frac{x e^x}{1 + e^x} - \ln(1 + e^x) \right] \Big|_{-\beta \hbar k_F}^0$$

$$= \frac{1}{(\beta\hbar)^2} \left[\frac{\beta\hbar k_F e^{-\beta\hbar k_F}}{1 + e^{-\beta\hbar k_F}} + \ln\left(\frac{1 + e^{-\beta\hbar k_F}}{2}\right) \right].$$

Therefore, the value of the integral is

$$II = \frac{k_F^2}{\beta E_F} \left[\frac{1}{1 + e^{-\beta E_F}} - \frac{1}{2} \right] + \frac{k_F^2}{(\beta E_F)^2} \left[\frac{\beta E_F e^{-\beta E_F}}{1 + e^{-\beta E_F}} + \ln\left(\frac{1 + e^{-\beta E_F}}{2}\right) \right].$$

By introducing $\sigma_0 \equiv e^2/h$, we arrive at

$$\begin{aligned} \sigma'_{xx} \equiv \frac{\sigma_{xx}^d}{\sigma_0} &= \frac{4}{A k_F} \frac{(l_\tau k_F)^2}{(k_s/k_F)^2} \left(\frac{1}{(\beta E_F)^2} \left[\frac{\beta E_F e^{-\beta E_F}}{1 + e^{-\beta E_F}} + \ln\left(\frac{1 + e^{-\beta E_F}}{2}\right) \right] \right. \\ &\quad \left. + \frac{1}{\beta E_F} \left[\frac{1}{1 + e^{-\beta E_F}} - \frac{1}{2} \right] \right). \end{aligned} \quad (8.20)$$

Because of the relation between the Fermi wave-vector and charge density in low energy limit for graphene, $k_F = \sqrt{2\pi n}$, we can rewrite the above equation as

$$\begin{aligned} \sigma'_{xx} &= \frac{1}{A} \frac{1}{\sqrt{\pi n}} \frac{(l_\tau k_F)^2}{(k_s/k_F)^2} \left(\frac{1}{(\beta E_F)^2} \left[\frac{\beta E_F e^{-\beta E_F}}{1 + e^{-\beta E_F}} + \ln\left(\frac{1 + e^{-\beta E_F}}{2}\right) \right] \right. \\ &\quad \left. + \frac{1}{\beta E_F} \left[\frac{1}{1 + e^{-\beta E_F}} - \frac{1}{2} \right] \right). \end{aligned} \quad (8.21)$$

In Fig. 8.1 (a) σ'_{xx} as a function of temperature for several values of $l_\tau k_F$ at a fixed value of Fermi energy and screening strength is shown. We see for a typical value of $l_\tau k_F$ the diagonal part of conductivity in the x direction, σ'_{xx} , increases by increasing the temperature. As seen with increasing $l_\tau k_F$ for a fixed temperature, the value of σ'_{xx} increases due to the lower probability of collisions. In Fig. 8.1 (b) we show σ'_{xx} versus temperature for a fixed value of Fermi energy and mean-free path for several screening strength. We see the same behavior such as Fig. 8.1 (a). However, the value of σ'_{xx} decrease by increasing k_s for a fixed temperature due to the change in strength of the Coulomb interaction which governs the interaction between the electrons.

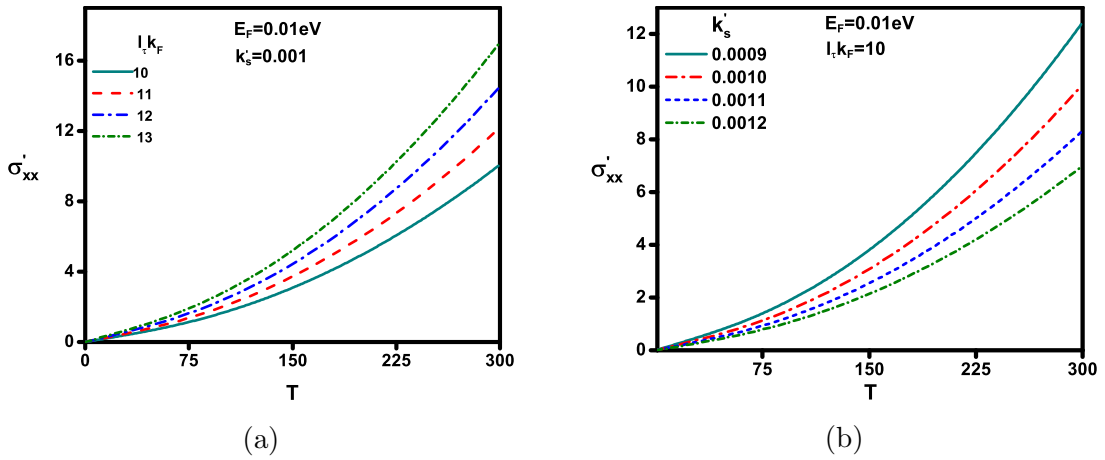


Figure 8.1: (a) σ'_{xx} versus temperature for several values of $l_\tau k_F$ for $k_s/k_F = 0.001$ and $E_F = 0.01$ eV. (b) σ'_{xx} versus temperature for several values of k_s/k_F for $l_\tau k_F = 10$ and $E_F = 0.01$ eV

For a fixed temperature and mean free distance value, for several values of screening strength, we show σ'_{xx} versus Fermi energy in Fig. 8.2 (a). As seen, by increasing the Fermi energy the value of conductivity decrease which can be understood as follows. The Fermi energy is proportional to the square root of electron density, $E_F \propto n^{1/2}$. This implies the probability of electron-electron interaction increase by increasing the electron density. Therefore, for lower value of Fermi energy, σ'_{xx} has higher value. To make the behavior of σ'_{xx} more clear for $E_F \geq 0$, in Fig. 8.2 (b) we show a portion of Fig. 8.2 (a).

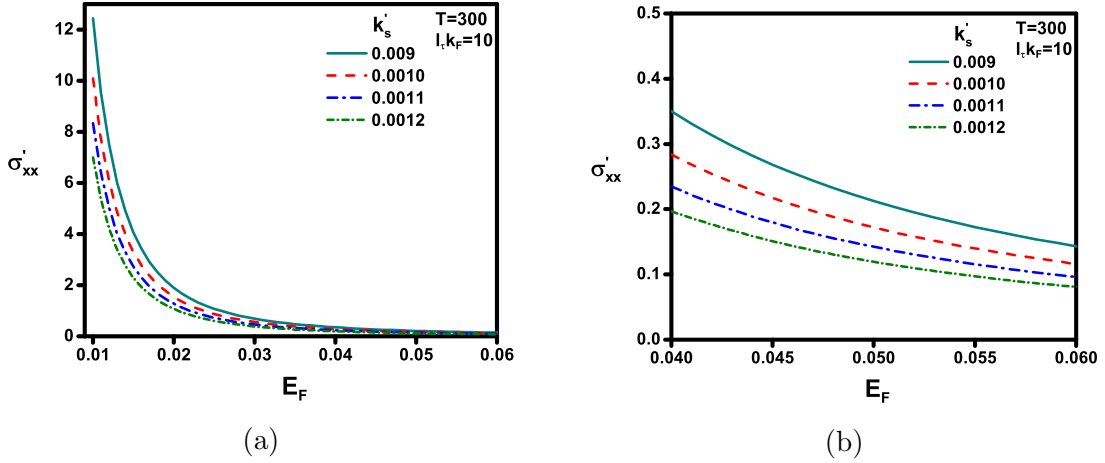


Figure 8.2: (a) σ'_{xx} versus Fermi energy for several values of $l_\tau k_F$ for $k_s/k_F = 0.001$ and $T = 300$. (b) a segment of (a) in the range of $0.04 \leq E_F \leq 0.06$ eV.

In Fig. 8.3 (a) for a typical value of screening and mean-free path, we show the 3D bar plot of σ'_{xx} as a function of Fermi energy and temperature. In the same way, for a typical value of screening and temperature, in Fig. 8.3 (b) the 3D bar plot of σ'_{xx} as a function of Fermi energy and mean free-path is shown.

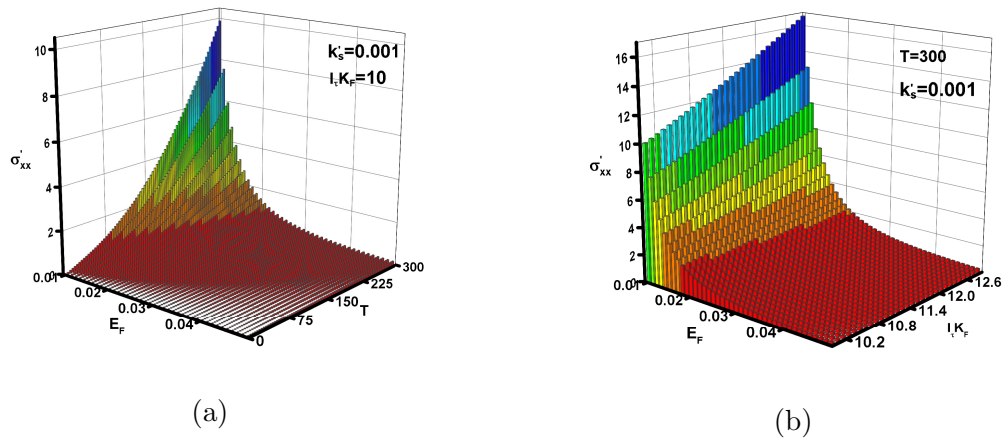


Figure 8.3: 3D bar of σ'_{xx} (a) versus Fermi energy and temperature for $k_s/k_F = 0.001$ and $l_\tau k_F = 10$. (b) versus Fermi energy and $l_\tau k_F$ for $T = 300$ and $k_s/k_F = 0.001$.

Using Eq. (8.4) the non-diagonal part of conductivity takes the form

$$\sigma_{\mu\nu}^{nd} = \frac{ie^2\hbar}{A} \sum_{i \neq i'} \langle i | v_\nu | i' \rangle \langle i' | v_\mu | i \rangle \frac{(f_i - f_{i'})}{(E_{i'} - E_i)^2}, \quad (8.22)$$

where we used the identity

$$f_i(1 - f_{i'}) [1 - e^{-\beta(E_{i'} - E_i)}] = (f_i - f_{i'}). \quad (8.23)$$

For $\mu = \nu = x = y$, Eq. (8.22) vanishes as can be seen by exchanging the indexes i by i' . This results in two terms with opposite signs. For $\mu = x, \nu = y$, in the case when an electric field such as $\vec{E} = E_x \hat{e}_x + E_y \hat{e}_y$ is applied, Eq. (8.22) leads to

$$\begin{aligned} \sigma_{xy}^{nd} &= \frac{ie^2 \hbar}{A} \sum_{\zeta s} \sum_{\vec{k} \neq \vec{k}'} \langle \vec{k} \zeta s | v_x | \vec{k}' \zeta s \rangle \langle \vec{k}' \zeta s | v_y | \vec{k} \zeta s \rangle \frac{(f_{\vec{k} \zeta s} - f_{\vec{k}' \zeta s})}{(E_{\vec{k}' \zeta s} - E_{\vec{k} \zeta s})^2} \\ &+ \frac{ie^2 \hbar}{A} \sum_{\vec{k} s} \sum_{\zeta \neq \zeta'} \langle \vec{k} \zeta s | v_x | \vec{k} \zeta' s \rangle \langle \vec{k} \zeta' s | v_y | \vec{k} \zeta s \rangle \frac{(f_{\vec{k} \zeta s} - f_{\vec{k} \zeta' s})}{(E_{\vec{k} \zeta' s} - E_{\vec{k} \zeta s})^2}, \end{aligned} \quad (8.24)$$

with

$$v_x = v_F \begin{pmatrix} 0 & 1 & 0 & 0 \\ 1 & 0 & 0 & 0 \\ 0 & 0 & 0 & -1 \\ 0 & 0 & -1 & 0 \end{pmatrix}, \quad v_y = v_F \begin{pmatrix} 0 & -i & 0 & 0 \\ i & 0 & 0 & 0 \\ 0 & 0 & 0 & -i \\ 0 & 0 & i & 0 \end{pmatrix}.$$

Let's first evaluate $\langle \vec{k} \zeta s | v_x | \vec{k}' \zeta s \rangle$ of the first term on the right hand side (RHS) of Eq. (8.24)

$$\langle \vec{k} \zeta s | v_x | \vec{k}' \zeta s \rangle = \frac{v_F}{4A} \begin{pmatrix} e^{-i\theta(\vec{k})} \\ \zeta \\ e^{i\theta(\vec{k})} \\ \zeta \end{pmatrix}^\dagger \begin{pmatrix} 0 & 1 & 0 & 0 \\ 1 & 0 & 0 & 0 \\ 0 & 0 & 0 & -1 \\ 0 & 0 & -1 & 0 \end{pmatrix} \begin{pmatrix} e^{-i\theta(\vec{k}')} \\ \zeta \\ e^{i\theta(\vec{k}')} \\ \zeta \end{pmatrix} \underbrace{\int e^{i\vec{r} \cdot (\vec{k}' - \vec{k})} d\vec{r}}_{\delta_{\vec{k}, \vec{k}'}}. \quad (8.25)$$

The sum over \vec{k} and \vec{k}' indicates they should be different. However, we have $\delta_{\vec{k}, \vec{k}'}$ which implies the first term of RHS of Eq. (8.24) vanishes. For the second term of Eq. (8.24), we evaluate $\langle \vec{k} \zeta s | v_x | \vec{k} \zeta' s \rangle$ which is

$$\langle \vec{k} \zeta s | v_x | \vec{k} \zeta' s \rangle \propto -\frac{v_F^2}{A} (\zeta - \zeta') \underbrace{\frac{A}{4\pi^2} \int_0^{2\pi} \sin(\theta) \cos(\theta) d\theta}_{=0} = 0. \quad (8.26)$$

Since both terms on RHS of Eq. (8.24) vanish we can conclude that σ_{xy}^{nd} vanishes.

9 Conclusions and outlook

This thesis presents a theoretical approach for many-body effects on transport and optical properties of novel nanostructures. Within the Drude model, we treated those properties in the classical regime for metallic systems. Then, we introduced the definition and concept of nanostructures and the importance of many-body effects in these systems such as quantum wires and wells. To study properties of these systems, we employed quantum linear response theory to evaluate the polarization function which enables one to obtain system's conductivity and permittivity. As an example of these novel systems, we studied TM and TE surface plasmons, reflection and transmission coefficients, and conductivity of armchair graphene nanoribbons in the Lindhard, random-phase, and Hubbard approximations where we used the tight binding as a reliable method to evaluate eigenvalues and eigenfunctions analytically. We showed that metallic ribbons do not support Brewster angles and TE surface plasmons. We demonstrated that in the long wave length limit, the linear response theory cannot retrieve the classical results of the Drude model. We discussed the adiabatic switching-on parameter which is designated to satisfy causality and avoid divergence in integration over time; and we showed that dissipations in a system originating from randomness need to be addressed in the system's Hamiltonian.

We evaluated the linear-response function to an external stimulus, obtained an expression that is valid for elastic scattering. This was achieved by applying the van Hove limit to all operators and by utilizing appropriate super-operators of the literature. The resulting polarization function has two terms, χ_{non} which is independent of the scattering, and χ_{im} who does depend on it and produces results that are qualitatively and quantitatively different from those of χ_{non} . In graphene the term χ_{non} dominates the response in the long wavelength limit, i.e., for very low frequencies, while the term χ_{im} dominates for all other frequencies.

As an application of this development, we evaluated plasmons in graphene and the 2DEG in the random-phase approximation. The main result of the term χ_{im} is that introduces scattering-dependent wave-vector limits below which no plasmons are allowed. It is also valid for all values of the wave vector, that is, it is not limited to the long wavelength limit as χ_{non} is. Another nice feature is that it simply explains and retrieves the Drude model results in the long wavelength limit. We showed new plasmon results for i) graphene and ii) the 2DEG. In i) we distinguished between intra-band (SB) and inter-band (TB) transitions. In both i) and ii) we obtained the scattering-induced limits referred to above, analytical dispersion relations, and their well-known long wavelength limit in the absence of scattering. An important difference between i) and ii) is that in the dimensionless units used the plasmon wave vector for graphene is independent of the electron density whereas in a 2DEG it is proportional to its square root, $q' \propto \sqrt{n}$. As discussed, depending on the scattering

strength γ' the single-particle excitations due to scattering drastically modify the frequency and wave vector domains (ω, q) of the collective excitations. The latter are suppressed below a critical γ' .

Next we evaluated TM SPs in graphene for SB and TB transitions in the absence of Coulomb interaction and local field factors, i.e., in the Lindhard approximation for the polarization function, but took into account scattering by impurities. We showed that the scattering strength γ restricts the SP domains for SB and TB transitions. Importantly, for each frequency there is a critical scattering strength γ_c below which SPs do not exist. The strength γ_c decreases with frequency, very fast for very low frequencies and much less for higher frequencies. Further, we explicitly evaluated the quality factor and found it is approximately equal to the square of $\alpha\lambda_{SP}/\gamma$, where α is the fine-structure constant and λ_{SP} the wavelength. For fixed frequency the quality factor decreases with γ for SB and TB transitions and is higher for the SB ones. In addition, we investigated TE SPs in the presence of impurity scattering and showed that the scattering suppresses them in both cases.

Finally, we investigated the electron-electron interaction on DC conductivity of graphene by considering the screening effect in the homogeneous quantum Boltzmann equation. We showed how electron density and temperature modify graphene conductivity.

Graphene, as the first member of 2D materials, was created by mechanical exfoliation in lab at room temperature. However, graphene has a high electron mobility, but it is gapless. There are some methods to open a band gap in graphene such as quantum confinement, defects, hybrid structures, and substrate to name a few. Advances in exfoliation techniques have enabled us to manufacture a single layer sheet from any 3D material. Silicene and germanene are silicon and germanium counterparts of graphene with buckled lattices in group IV. Due to the spin-orbit coupling (SOC), they have a band gap in the order of a few meV at the Dirac points. Another class of 2D materials that has band gap on the desired order is transition metal chalcogenides (TMCs) which makes them promising candidates for the new generation of electronic devices. A single layer TMC is comprised of a hexagonally ordered plane of metal atoms sandwiched between two hexagonally ordered planes of chalcogen atoms.

There are several areas of research regarding the transport and optical properties of novel structure graphene-like materials that require further study and investigations, including:

1. Studying the effect of normal and tangential magnetic fields on dynamical transport of transition metal chalcogenides such as WSe_2 and investigating many-body effects such as electron-electron interaction, screening, and exchange-hole.
2. Studying the impurity effects on transport and optical properties of WSe_2 in the presence and absence of magnetic and electric fields.
3. Investigating the phonon-phonon response function to determine thermal conductivity of novel structures in quantum regime.
4. Extending the above-mentioned studies on double-layer systems.
5. Studying transport and optical properties of single and multi-layer novel structures by considering many-body effects.

6. Extending response function to higher orders to evaluate second and third nonlinear response terms.
7. Simulating transport and optical properties by finite-difference time domain (FDTD) and finite-element method (FEM) using parallel computing such as OpenMp and OpenAcc.

Bibliography

- [1] Michael Riordan and Lillian Hoddeson, “*Crystal fire : the birth of the information age*”, (Norton, 1997).
- [2] Raul Rojas, “*Encyclopedia of computers and computer history*”, (Fitzroy Dearborn, 2001).
- [3] Gerard O’Regan, “*Introduction to the history of computing : a computing history primer*”, (Springer, 2016).
- [4] Chris Oxlade, “*The History of Computers*”, (Heinemann-Raintree, 2018).
- [5] M. I. Stockman, “The spacer as a nanoscale quantum generator and ultrafast amplifier,” *J. Opt.* **12**, 024004 (2010).
- [6] E. Ozbay, ”Plasmonics: Merging Photonics and Electronics at Nanoscale Dimensions,” *Science*. **13**, 189-193 (2006).
- [7] M. L. Brongersma, V. M. Shalaev, ”The Case for Plasmonics,” *Science*. **328**, 440-441 (2010).
- [8] D. K. Gramotnev and S. I. Bozhevolnyi, ”Plasmonics beyond the diffraction limit,” *Nat. Photon.* **4**, 83-91 (2010).
- [9] M. S. Kushwaha, “Plasmons and magnetoplasmons in semiconductor heterostructures,” *Surf. Sci. Reports.* **41**, 1-416 (2001).
- [10] G. V. Naik, V. M. Shalaev, A. Boltasseva, “Alternative Plasmonic Materials: Beyond Gold and Silver,” *Advanced Materials* **25**, 3264-3294 (2013).
- [11] A. Boltasseva, H. A. Atwater, ”Low-Loss Plasmonic Metamaterials,” *Science*. **33**, 290-291 (2011).
- [12] L. Tang, S. E. Kocabas, S. Latif, A. K. Okyay, D. Ly-Gagnon, K. C. Saraswat, D. A. B. Miller, ”Nanometre-scale germanium photodetector enhanced by a near-infrared dipole antenna,” *Nat. Photon.* **2**, 226-229 (2008).
- [13] S. A. Maier, M. L. Brongersma, P. G. Kik, S. Meltzer, A. A. G. Requicha, H. A. Atwater, ”Plasmonics- a route to nanoscale optical devices,” *Adv. Mater.* **13**, 1501 (2001).
- [14] T. Low and P. Avouris, “Graphene Plasmonics for Terahertz to Mid-Infrared Applications,” *ACS Nano.* **8**, 1086-1101 (2014).

- [15] Z. Sun, A. Martinez and F. Wang, "Optical modulators with 2D layered materials," *Nature Photonics* **10**, 227-238 (2016).
- [16] S. Jang, E. Hwang, Y. Lee, S. Lee, and J. H. Cho, "Multifunctional Graphene Optoelectronic Devices Capable of Detecting and Storing Photonic Signals," *Nano Lett.* **15**, 2542-2547 (2015).
- [17] Y. Zhao and Y. Zhu, "Graphene-based hybrid films for plasmonic sensing," *Nanoscale.*, **7**, 14561-14576 (2015).
- [18] M. Kauranen and A. V. Zayats, "Nonlinear plasmonics," *Nature Photonics* **6**, 737-748 (2012).
- [19] S. I. Bozhevolnyi, J. B. Khurgin, "The case for quantum plasmonics," *Nat. Photon.* **11**, commentary (2017).
- [20] J. Chen, M. Badioli, P. Alonso-Gonzalez, S. Thongrattanasiri, F. Huth, J. Osmond, M. Spasenovic, A. Centeno, A. Pesquera, P. Godignon, A. Z. Elorza, N. Camara, F. J. G. de Abajo, R. Hillenbrand, F. H. L. Koppens, "Optical nano-imaging of gate-tunable graphene plasmons," *Nature.* **487**, 77-81 (2012).
- [21] Z. Fei, A. S. Rodin, G. O. Andreev, W. Bao, A. S. McLeod, M. Wagner, L. M. Zhang, Z. Zhao, M. Thiemens, G. Dominguez, M. M. Fogler, A. H. Castro Neto, C. N. Lau, F. Keilmann, D. N. Basov, "Gate-tuning of graphene plasmons revealed by infrared nano-imaging," *Nature.* **487**, 82-85 (2012).
- [22] Q. Bao and K. P. Loh, "Graphene Photonics, Plasmonics, and Broadband Optoelectronic Devices," *ACS Nano.* **2**, 3677-3694 (2012).
- [23] L. Ju, B. Geng, J. Horng, C. Girit, M. Martin, Z. Hao, H. A. Bechtel, X. Liang, A. Zettl, Y. R. Shen and F. Wang, "Graphene plasmonics for tunable terahertz metamaterials," *Nature Nanotechnology* **6**, 630-634 (2011).
- [24] A. A. Shylau, S. M. Badalyan, F. M. Peeters, A. P. Jauho, "Electron polarization function and plasmons in metallic armchair graphene nanoribbons," *Phys. Rev. B* **91**, 205444 (2015).
- [25] D. R. Andersen and H. Raza, "Collective modes of massive Dirac fermions in armchair graphene nanoribbons," *J. Phys. Condens. Matter* **25**, 045303 (2013).
- [26] L. Brey and H. A. Fertig, "Elementary electronic excitations in graphene nanoribbons," *Phys. Rev. B* **75**, 125434 (2007).
- [27] C. E. P. Villegas, M. R. S. Tavares, G. Q. Hai, and P. Vasilopoulos, "Plasmon modes and screening in double metallic armchair graphene nanoribbons," *Phys. Rev. B* **88**, 165426 (2013).
- [28] M. Bagheri and M. Bahrami, "Plasmons in spatially separated double-layer graphene nanoribbons," *J. Appl. Phys.* **115**, 174301 (2014).
- [29] Y. Wang and D. R. Andersen, "First-principles study of the terahertz third-order nonlinear response of metallic armchair graphene nanoribbons," *Phys. Rev. B* **93**, 235430 (2016).

- [30] Y-W Son, M. L. Cohen, and S. G. Louie, “Energy Gaps in Graphene Nanoribbons,” *Phys. Rev. Lett.* **97**, 216803 (2006); D. Gunlycke and C. T. White, “Tight-binding energy dispersions of armchair-edge graphene nanostrips,” *Phys. Rev. B* **77**, 115116 (2008).
- [31] G. Seol, and J. Guo, “Bandgap opening in boron nitride confined armchair graphene nanoribbon,” *Appl. Phys. Lett.*, **98**, 143107 (2011).
- [32] G. Z. Magda, X. Jin, I. Hagymasi, P. Vancso, Z. Osvath,, P. Nemes-Incze, C. Hwang, L. P. Biro, and L. Tapaszto, “Room-temperature magnetic order on zigzag edges of narrow graphene nanoribbons,” *Nature* , **514**, 608-611 (2014).
- [33] M. Jablan, H. Buljan, M Soljagic, ”New Electromagnetic Mode in Graphene,” *PRB.* **80**, 245435 (2009).
- [34] Luca Salasnich, “*Quantum Physics of Light and Matter*”, (Springer, 2014).
- [35] Mark Fox, “*Quantum Optics: An Introduction*”, (Oxford University, 2006).
- [36] Martin Dressel and George Gruner, “*Electrodynamics of Solids: Optical Properties of Electrons in Matter*”, (Cambridge University, 2010).
- [37] John David Jackson, “*Classical Electrodynamics*”, (John Wiley & Sons, 1999).
- [38] Nasser Peyghambarian , Stephan W. Koch, and Andre Mysyrowicz, “*Introduction to Semiconductor Optics*”, (Prentice Hall, 1993).
- [39] Govind P. Agrawal and Malin Premaratne, “*light propagation in gain media optical amplifiers*”, (Cambridge University, 2011).
- [40] Alexander L. Fetter and John Dirk Walecka, “*Quantum Theory of Many-Particle Systems*”, (McGraw-Hill, 1971).
- [41] Gabriele Giuliani and Giovanni Vignale, “*Quantum Theory of the Electron Liquid*”, (Cambridge University, 2005).
- [42] Neil W. Ashcroft and N. David Mermin, “*Solid State Physics*”, (Harcourt College, 1976).
- [43] Piers Coleman, “*Introduction to Many-Body Physics*”, (Cambridge University, 2015).
- [44] Giuseppe Grosso and Giuseppe Pastori Parravicini, “*Solid State Physics*”, (Academic, 2014).
- [45] Hartmut Haug and Stephan W Koch, “*Quantum Theory of the Optical and Electronic Properties of Semiconductors*”, (World Scientific, 2009).
- [46] Stefan Alexander Maier, “*Plasmonics: Fundamentals and Applications*”, (Springer, 2007).
- [47] Lukas Novotny and Bert Hecht, “*Principles of Nano-Optics*”, (Cambridge University, 2006).

- [48] Robert Zwanzig, “*Nonequilibrium Statistical Mechanics*”, (Oxford University, 2001).
- [49] Gerd Röpke, “*Nonequilibrium Statistical Physics*”, (Wiley-VCH, 2013).
- [50] Michael Plischke and Birger Bergersen, “*Equilibrium Statistical Physics*”, (World Scientific, 2006).
- [51] Carolyne M Van Vliet, “*Equilibrium and Non-Equilibrium Statistical Mechanics*”, (World Scientific, 2008).
- [52] Henrik Bruus and Karsten Flensberg, “*Many-Body Quantum Theory in Condensed Matter Physics: An Introduction*”, (Oxford University, 2004).
- [53] Nouredine Zettili, “*Quantum Mechanics Concepts and Applications*”, (John Wiley & Sons, 2009).
- [54] Paul Harrison and Alex Valavanis, “*Quantum Wells, Wires and Dots: Theoretical and Computational Physics of Semiconductor Nanostructures*”, (Wiley, 2005).
- [55] David Pines and David Bohm, ”A Collective Description of Electron Interactions: II. Collective vs Individual Particle Aspects of the Interactions”, *Phys. Rev.* **85**, 338 (1952).
- [56] David Pines and David Bohm, ”A Collective Description of Electron Interactions: III. Coulomb Interactions in a Degenerate Electron Gas”, *Phys. Rev.* **92**, 609 (1953).
- [57] Murat Tas, ”Dielectric Formulation of One-dimensional Electron Gas”, (2004).
- [58] Bogdan Mihaila, ”Lindhard function of a d-dimensional Fermi gas”, arxiv: 1111.5337v1 (2011).
- [59] Zhifeng Ren, Yucheng Lan and Yang Wang, “*Introduction to Carbon*”, Aligned Carbon Nanotubes, (Springer, 2012).
- [60] Nada F. Atta, Ahmed Galal and Ekram H. El-Ads, ”Graphene –A Platform for Sensor and Biosensor Applications”. In: Toonika R (ed) Biosensors-micro and nanoscale applications, InTech, pp 37-84, (2015)
- [61] Sumio Iijima, ”Helical microtubules of graphitic carbon”, *Nature.* **354**, 56-58 (1991).
- [62] A. K. Geim and K. S. Novoselov, ”The rise of graphene”, *Nature Materials.* **6**, 183-191 (2007).
- [63] Jenő Solyom, “*Fundamentals of the Physics of Solids*”, (Springer, 2007).
- [64] Gholam Reza Yazdi, Tihomir Iakimov and Rositsa Yakimova, ”Epitaxial Graphene on SiC: A Review of Growth and Characterization”, *Crystals.* **6(5)**, 53 (2016).

- [65] GJae-Ung Lee, Duhee Yoon, and Hyeonsik Cheong, "Estimation of Young's Modulus of Graphene by Raman Spectroscopy", *Nano Lett.* **12**(9), 4444-4448 (2012).
- [66] Khan M.F. Shahil and Alexander A. Balandin, "Thermal properties of graphene and multilayer graphene: Applications in thermal interface materials", *Solid State Communications.* **152** 1331-1340, (2012).
- [67] Michael P. Marder, "*Condensed Matter Physics*", (Wiley, 2010).
- [68] A. H. Castro Neto, F. Guinea, N. M. R. Peres, K. S. Novoselov, and A. K. Geim, "The electronic properties of graphene", *Rev. Mod. Phys.* **81**, 109 (2009).
- [69] George B. Arfken and Hans J. Weber, "*Essential Mathematical Methods for Physicists*", (Academic, 2003).
- [70] E. N. Economou, "*Green's Functions in Quantum Physics*", (Springer, 2006).
- [71] B. Wunsch, T. Stauber, F. Sols, and F. Guinea, *New Journal of Physics.* **8**, 318 (2006).
- [72] E. H. Hwang and S. Das Sarma, "Dielectric function, screening, and plasmons in two-dimensional graphene", *Phys. Rev. B.* **75**, 205418 (2007).
- [73] V. N. Kotov, B. Uchoa, V. M. Pereira, F. Guinea, and A. H. Castro Neto, "Electron-Electron Interactions in Graphene: Current Status and Perspectives," *Rev. Mod. Phys.* **84**, 1067 (2011).
- [74] David Griffiths, "*Introduction to Electrodynamics*", (Prentice Hall, 1999).
- [75] Q. Bao and K. P. Loh, "Graphene Photonics, Plasmonics, and Broadband Optoelectronic Devices," *ACS Nano.* **2**, 3677-3694 (2012).
- [76] S. Xiao, X. Zhu, B.H. Li, N. A. Mortensen, "Graphene-plasmon polaritons: From fundamental properties to potential applications," *Front. Phys.* **11**, 117801 (2016).
- [77] Y. Zhong, S. D. Malagari, T. Hamilton, and D. Wasserman, "Review of mid-infrared plasmonic materials," *Journal of Nanophotonics.* **9**, 093791 (2015).
- [78] T. Stauber, "Plasmonics in Dirac systems: from graphene to topological insulators," *Journal of Physics: Cond. Matter.* **26**, 123201 (2014).
- [79] A. N. Grigorenko, M. Polini and K. S. Novoselov, "Graphene plasmonics," *Nature Photonics* **6**, 749-758 (2012).
- [80] A. Politano and G. Chiarello, "Plasmon modes in graphene: status and prospect," *Nanoscale* **6**, 10927-10940 (2014).
- [81] S. A. Mikhailov and D. Beba, "Nonlinear broadening of the plasmon linewidth in a graphene stripe," *New Journal of Physics.* **14**, 115024 (2012).
- [82] W. Wang and J. M. Kinaret, "Plasmons in graphene nanoribbons: Interband transitions and nonlocal effects," *Phys. Rev. B* **87**, 195424 (2013).

- [83] L. Ju, B. Geng, J. Horng, C. Girit, M. Martin, Z. Hao, H. A. Bechtel, X. Liang, A. Zettl, Y. R. Shen and F. Wang, "Graphene plasmonics for tunable terahertz metamaterials," *Nature Nanotechnology* **6**, 630-634 (2011).
- [84] J. H. Strait, P. Nene, W. M. Chan, C. Manolatou, S. Tiwari, and F. Rana, "Confined plasmons in graphene microstructures: Experiments and theory," *Phys. Rev. B* **87**, 241410 (2013).
- [85] A. A. Shylau, S. M. Badalyan, F. M. Peeters, A. P. Jauho, "Electron polarization function and plasmons in metallic armchair graphene nanoribbons," *Phys. Rev. B* **91**, 205444 (2015).
- [86] D. R. Andersen and H. Raza, "Collective modes of massive Dirac fermions in armchair graphene nanoribbons," *J. Phys. Condens. Matter* **25**, 045303 (2013).
- [87] L. Brey and H. A. Fertig, "Elementary electronic excitations in graphene nanoribbons," *Phys. Rev. B* **75**, 125434 (2007).
- [88] C. E. P. Villegas, M. R. S. Tavares, G. Q. Hai, and P. Vasilopoulos, "Plasmon modes and screening in double metallic armchair graphene nanoribbons," *Phys. Rev. B* **88**, 165426 (2013).
- [89] M. Bahrami and P. Vasilopoulos, "Exchange, correlation, and scattering effects on surface plasmons in arm-chair graphene nanoribbons," *Opt. Express*. **25**(14), 16840-16853 (2017).
- [90] F. J. G. Abajo, "Graphene Plasmonics: Challenges and Opportunities," *ACS Photonics*. **1**, 135-152 (2014).
- [91] Xue-Feng Wang, "Plasmon spectrum of two-dimensional electron systems with Rashba spin-orbit interaction," *Phys. Rev. B* **72**, 085317 (2005).
- [92] M. Bosman, E. Ye, S. F. Tan, C. A. Nijhuis, J. K. W. Yang, R. Marty, A. Mlayah, A. Arbouet, C. Girard, and M. Han, "Surface Plasmon Damping Quantified with an Electron Nanoprobe," *Scientific Reports* **3**, 1312 (2013).
- [93] S.A. Mikhailov, K. Ziegler, "New Electromagnetic Mode in Graphene," *PRL*. **99**, 016803 (2007).
- [94] P. Vasilopoulos and C. M. Van Vliet, "Influence of the electron-electron interaction on the Aharonov-Bohm effect," *Phys. Rev. B* **34**, 4375(R) (1987).
- [95] M. Charbonneau, K. M. van Vliet, and P. Vasilopoulos, "Linear response theory revisited III: One-body response formulas and generalized Boltzmann equations," *J. Math. Phys* **23**, 318 (1982).

A Time ordering operator

The time-evaluation of wave functions and operators in the interaction picture are

$$\begin{aligned} |\hat{\psi}(t)\rangle &\equiv e^{iH_0t} |\psi\rangle, & \text{State,} \\ \hat{A}(t) &= e^{iH_0t} \hat{A} e^{-iH_0t}, & \text{Operator,} \\ &H_0, & \text{Time independent,} \end{aligned} \quad (\text{A.1})$$

where we let $\hbar = 1$. The system's Hamiltonian is given by

$$H = H_0 + V(t). \quad (\text{A.2})$$

By evaluating the time derivative of the wave function, $|\hat{\psi}(t)\rangle$, we obtain the following useful relation

$$i\partial_t |\hat{\psi}(t)\rangle = \hat{V}(t) |\hat{\psi}(t)\rangle, \quad (\text{A.3})$$

where ∂_t indicates the partial time derivative. Since the time evolution of $|\hat{\psi}(t)\rangle$ is given only by (A.3) the Schroedinger equation reduces to this equation. This indicates that $|\hat{\psi}(t)\rangle$ and $|\hat{\psi}(0)\rangle$ are related through an unitary transformation like $\hat{U}(t, t_0)$ that only depends on $V(t)$

$$|\hat{\psi}(t)\rangle = \hat{U}(t, t_0) |\hat{\psi}(t_0)\rangle. \quad (\text{A.4})$$

From Eqs. (A.3) and (A.4) we obtain

$$i\partial_t \hat{U}(t, t_0) = \hat{V}(t) \hat{U}(t, t_0). \quad (\text{A.5})$$

In addition, from Eq.(A.3) we have the boundary condition $\hat{U}(t_0, t_0) = 1$. To solve Eq. (A.5) we integrate which leads to

$$\hat{U}(t, t_0) = 1 + \frac{1}{i} \int_{t_0}^t dt' \hat{V}(t') \hat{U}(t', t_0). \quad (\text{A.6})$$

This indicates the solution can be obtained by iteration and the solution has the following form

$$\hat{U}(t, t_0) = 1 + \frac{1}{i} \int_{t_0}^t dt' \hat{V}(t') + \frac{1}{i^2} \int_{t_0}^t dt' \hat{V}(t') \int_{t_0}^{t'} dt'' \hat{V}(t'') + \dots \quad (\text{A.7})$$

To express results in a more compact form we use the following relation. The second term in the (A.7) can be rewritten

$$\int_{t_0}^t dt' \hat{V}(t') \int_{t_0}^{t'} dt'' \hat{V}(t'')$$

$$\begin{aligned}
 &= \frac{1}{2} \int_{t_0}^t dt' \hat{V}(t') \int_{t_0}^t dt'' \hat{V}(t'') + \frac{1}{2} \int_{t_0}^t dt'' \hat{V}(t'') \int_{t_0}^t dt' \hat{V}(t') \\
 &= \frac{1}{2} \int_{t_0}^t dt' \int_{t_0}^t dt'' \hat{V}(t') \hat{V}(t'') \theta(t' - t'') + \frac{1}{2} \int_{t_0}^t dt'' \int_{t_0}^t dt' \hat{V}(t'') \hat{V}(t') \theta(t'' - t') \\
 &\equiv \frac{1}{2} \int_{t_0}^t dt' \int_{t_0}^t dt'' T_t [\hat{V}(t') \hat{V}(t'')].
 \end{aligned} \tag{A.8}$$

By some algebra we can extend this to higher order. To finally obtain

$$\hat{U}(t, t_0) = \sum_{j=0}^{\infty} \frac{1}{j!} \left(\frac{1}{i}\right)^j \int_{t_0}^t dt_1 \dots \int_{t_0}^t dt_j T_t [\hat{V}(t_1) \dots \hat{V}(t_j)] = T_t \left[\exp\left(-i \int_{t_0}^t dt' \hat{V}(t')\right) \right]. \tag{A.9}$$

B Matrix elements of the Coulomb potential of AGNRs

The normalized wave function of an AGNR is given by

$$\mathcal{U}(\vec{r}) = \mathcal{U}_{k,k_y(n),\eta}(x, y) = \frac{1}{\sqrt{4LW}} \begin{pmatrix} \left(\begin{array}{c} \eta e^{-i\theta(k,k_y(n))} \\ 1 \end{array} \right) e^{ik_y(n)y} \\ \left(\begin{array}{c} -\eta e^{-i\theta(k,k_y(n))} \\ 1 \end{array} \right) e^{-ik_y(n)y} \end{pmatrix} e^{ikx} X_s, \quad (\text{B.1})$$

where X_s denotes the spin part of the wave function. In second quantization representation, the Coulomb potential operator is

$$\hat{V} = \frac{1}{2} \int \int d\vec{r} d\vec{r}' \hat{\mathcal{U}}^\dagger(\vec{r}) \hat{\mathcal{U}}(\vec{r}') V(\vec{r} - \vec{r}') \hat{\mathcal{U}}(\vec{r}) \hat{\mathcal{U}}^\dagger(\vec{r}'), \quad (\text{B.2})$$

where the field operator $\hat{\mathcal{U}}(\vec{r})$ is given by

$$\hat{\mathcal{U}}(\vec{r}) = \sum_{k,n,\eta,s} \hat{a}_{k,n,\eta,s} \mathcal{U}_{k,k_y(n),\eta}(x, y). \quad (\text{B.3})$$

By substituting Eq. (B.3) into Eq. (B.2) we have

$$\begin{aligned} \hat{V} &= \frac{1}{2} \left(\frac{1}{\sqrt{4LW}} \right)^4 \int \int d\vec{r} d\vec{r}' \left[\sum_{k,n,\eta,s} \hat{a}_{k,n,\eta,s} \begin{pmatrix} \left(\begin{array}{c} \eta e^{-i\theta(k,k_y(n))} \\ 1 \end{array} \right) e^{ik_y(n)y} \\ \left(\begin{array}{c} -\eta e^{-i\theta(k,k_y(n))} \\ 1 \end{array} \right) e^{-ik_y(n)y} \end{pmatrix} e^{ikx} X_s \right]^\dagger \\ &\times \left[\sum_{k',n',\eta',s'} \hat{a}_{k',n',\eta',s'} \begin{pmatrix} \left(\begin{array}{c} \eta e^{-i\theta(k',k_y(n'))} \\ 1 \end{array} \right) e^{ik_y(n')y'} \\ \left(\begin{array}{c} -\eta e^{-i\theta(k',k_y(n'))} \\ 1 \end{array} \right) e^{-ik_y(n')y'} \end{pmatrix} e^{ik'x'} X_{s'} \right]^\dagger V(\vec{r} - \vec{r}') \\ &\times \left[\sum_{\nu',m',\mu',\alpha'} \hat{a}_{\nu',m',\mu',\alpha'} \begin{pmatrix} \left(\begin{array}{c} \mu' e^{-i\theta(\nu',k_y(m'))} \\ 1 \end{array} \right) e^{ik_y(m)y'} \\ \left(\begin{array}{c} -\mu' e^{-i\theta(\nu',k_y(m'))} \\ 1 \end{array} \right) e^{-ik_y(m)y'} \end{pmatrix} e^{i\nu'x'} X_{\alpha'} \right] \\ &\times \left[\sum_{\nu,m,\mu,\alpha} \hat{a}_{\nu,m,\mu,\alpha} \begin{pmatrix} \left(\begin{array}{c} \mu e^{-i\theta(\nu,k_y(m))} \\ 1 \end{array} \right) e^{ik_y(m)y'} \\ \left(\begin{array}{c} -\mu e^{-i\theta(\nu,k_y(m))} \\ 1 \end{array} \right) e^{-ik_y(m)y'} \end{pmatrix} e^{i\nu x'} X_\alpha \right]. \quad (\text{B.4}) \end{aligned}$$

After some algebra we arrive at

$$\begin{aligned}
 \hat{V} &= 4 \frac{1}{2} \left(\frac{1}{4LW} \right)^2 \sum_{k,n,\eta,s} \sum_{k',n',\eta,s'} \sum_{\nu',m',\mu',\alpha'} \sum_{\nu,m,\mu,\alpha} \hat{a}_{k,n,\eta,s}^\dagger \hat{a}_{k',n',\eta',s'}^\dagger \hat{a}_{\nu',m',\mu',\alpha'} \hat{a}_{\nu,m,\mu,\alpha} \\
 &\times \underbrace{\{X_s^\dagger X_\alpha\}}_{\delta_{s\alpha}} \underbrace{\{X_{s'}^\dagger X_{\alpha'}\}}_{\delta_{s'\alpha'}} (1 + \eta\mu e^{i[\theta(k,k_y(n)) - \theta(\mu,k_y(m))]}) \left(1 + \eta'\mu' e^{i[\theta(k',k_y(n')) - \theta(\mu',k_y(m'))]} \right) \\
 &\times \int_0^W \int_0^W \frac{V(q, y-y')}{L} \cos([k_y(m) - k_y(n)] y) \cos([k_y(m') - k_y(n')] y') dy dy' \\
 &\times \underbrace{\int dx e^{i(\nu-k+q)x}}_{L\delta_{\nu,k-q}} \underbrace{\int dx' e^{i(k'-\nu'+q)x'}}_{L\delta_{\nu',k'+q}}. \tag{B.5}
 \end{aligned}$$

Applying Kronecker deltas and using $y = uW$ and $y' = u'W'$ we obtain

$$\begin{aligned}
 \hat{V} &= \frac{1}{8} \sum_{k,n,\eta,s} \sum_{k',n',\eta,s'} \sum_{m',\mu'} \sum_{m,\mu} \hat{a}_{k,n,\eta,s}^\dagger \hat{a}_{k',n',\eta',s'}^\dagger \hat{a}_{k'+q,m',\mu',s'} \hat{a}_{k-q,m,\mu,s} \int_0^1 \int_0^1 du du' \\
 &\times \frac{V(q, W(u-u'))}{L} \cos([k_y(m) - k_y(n)] \pi u) \cos([k_y(m') - k_y(n')] \pi u'), \tag{B.6}
 \end{aligned}$$

where $V(q, W(u-u'))$ is the Fourier component of the Coulomb potential, that is

$$\frac{e^2}{|\vec{r} - \vec{r}'|} = \frac{1}{L} \sum_q V(q, y, z) e^{iqx}. \tag{B.7}$$

We can find $V(q)$ by multiplying both sides of Eq. (B.7) by $e^{-iq'x}$ which leads to

$$\begin{aligned}
 V(q, y, z) &= e^2 \int_{-\infty}^{\infty} dx \frac{e^{-iqx}}{\sqrt{x^2 + y^2 + z^2}} \\
 &= e^2 \int_{-\infty}^{\infty} dx \frac{\cos(qx)}{\sqrt{x^2 + y^2 + z^2}} - \underbrace{ie^2 \int_{-\infty}^{\infty} dx \frac{\sin(qx)}{\sqrt{x^2 + y^2 + z^2}}}_{=0}. \tag{B.8}
 \end{aligned}$$

By introducing $a^2 = y^2 + z^2$ and some calculations we arrive at

$$V(q, y, z) = 2e^2 \int_0^{\infty} dx \frac{\cos\left(\frac{x}{a} qa\right)}{a \sqrt{1 + \left(\frac{x}{a}\right)^2}}, \tag{B.9}$$

where by introducing $x = ta$ Eq. (B.9) becomes

$$V(q, y, z) = 2e^2 \int_0^{\infty} dt \frac{\cos(qat)}{\sqrt{1 + (t)^2}} = 2e^2 K_0 \left(\left| q \sqrt{y^2 + z^2} \right| \right). \tag{B.10}$$

We can rewrite Eq. (B.6) as

$$\hat{V} = \frac{1}{8} \sum_{k,n,\eta,s} \sum_{k',n',\eta,s'} \sum_{m,\mu,m',\mu'} \sum_q \hat{a}_{k,n,\eta,s}^\dagger \hat{a}_{k',n',\eta',s'}^\dagger \hat{a}_{k'+q,m',\mu',s'} \hat{a}_{k-q,m,\mu,s} V_{n,n',m,m'}(q),$$

with

$$\begin{aligned}
 V_{n,n',m,m'}(q) \equiv V_{m-n,m'-n'}(q) &= \frac{2e^2}{\epsilon_b} \int_0^1 \int_0^1 K_0(|qW(u-u')|) \cos([k_y(m) - k_y(n)]\pi u) \\
 &\times \cos([k_y(m') - k_y(n')]\pi u') du du'. \quad (\text{B.11})
 \end{aligned}$$

In Fig. B.1 we plot $V_{m-n,m'-n'}(q)$ for several values of sub-band indices for $dm = 23$. As seen, the strength of the components with the same sub-band index, $V_{0,0}(q)$, is larger than others.

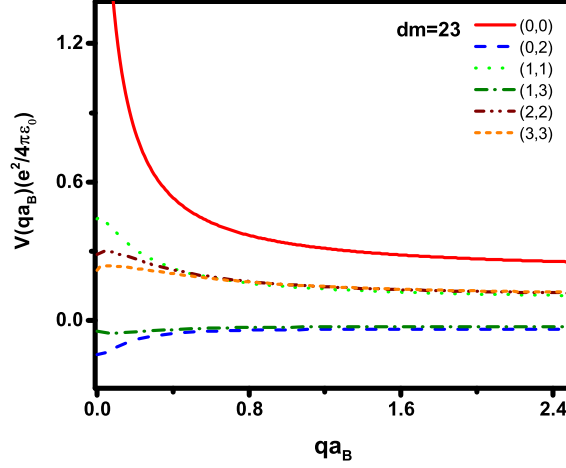


Figure B.1: Several values of the Fourier components of the Coulomb potential with $dm = 23$.

In Fig. B.2 we show $V_{0,0}(q)$ for several values of dm . As seen, $V_{0,0}(q)$ for an AGNR with smaller width has higher value.

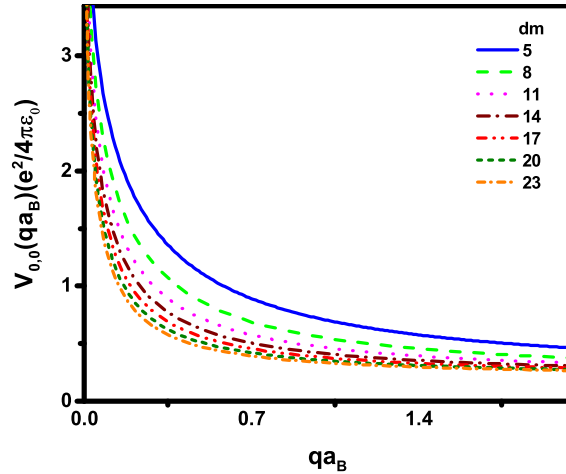


Figure B.2: Fourier components of the Coulomb potential, $V_{0,0}(q)$, for several values of dm .